# Cold atoms in two dimensional quasi crystals

Zhaoxuan Zhu

INSTITUT POLYTECHNIQUE DE PARIS

NNT : 2024IPPAX017

Thèse de doctorat

# Cold atoms in two dimensional quasicrystals

Thèse de doctorat de l'Institut Polytechnique de Paris
préparée à l'École polytechnique

École doctorale n°626 École doctorale de l'Institut Polytechnique de Paris (EDIPP)
Spécialité de doctorat : Physique

Thèse présentée et soutenue à Palaiseau, le 29/02/2024, par

**ZHAOXUAN ZHU**

Composition du Jury :

| | |
|---|---|
| Marcel Filoche<br>Research Director at CNRS, Ecole Supérieure de Physique et de Chimie Industrielles | Rapporteur |
| Patrik Öhberg<br>Professor at Heriot-Watt University | Rapporteur |
| Patrizia Vignolo<br>Professor at the University of Nice | Présidente |
| Nicolas Dupuis<br>Research Director at CNRS, Sorbonne Université | Examinateur |
| Anuradha Jagannathan<br>Professor at Université Paris-Saclay | Examinateur |
| Laurent Sanchez-Palencia<br>Research Director at CNRS, Ecole Polytechnique | Directeur de thèse |

# Contents

# Résumé

Les quasi-cristaux sont des solides ordonnés à longue distance sans symétrie de translation, présentant des symétries rotationnelles qui sont interdites pour les cristaux normaux, par exemple d'ordre 5, 7, 8, ... Leur découverte en laboratoire dans les années 1980 a entraîné un changement de paradigme en cristallographie, révolutionnant notre compréhension de la structure possible des solides [1–3]. Depuis lors, les quasi-cristaux ont attiré beaucoup d'attention en raison de leurs propriétés intrigantes, notamment les quasi-particules phasoniques [4–6], les propriétés de transport [7–10], le spectre d'énergie complexe [11–13], l'ordre topologique non trivial [14–18] et la localisation de type Anderson [19, 20]. Un outil puissant pour étudier les propriétés physiques des quasi-cristaux est la simulation quantique [21–23]. Avec la réalisation de systèmes atomiques ultrafroids dans les années 1990 [24, 25] et les développements rapides qui ont suivi, un nouveau terrain de jeu pour la physique quantique à plusieurs corps s'est ouvert. En particulier, le contrôle précis des paramètres physiques et les différents outils de mesure dans un système atomique froid en font une plateforme prometteuse pour la simulation quantique [26, 27]. Un potentiel quasipériodique unidimensionnel dans les expériences sur les atomes froids peut être créé en superposant plusieurs faisceaux laser avec des périodes incommensurables. Au cours des dernières années, les atomes froids dans des potentiels quasipériodiques unidimensionnels ont été largement étudiés[20, 28–45]. Un réseau optique bidimensionnel formant un potentiel quasi-cristallin peut également être créé par certaines configurations géométriques de faisceaux laser. Cela a été proposé pour la première fois théoriquement en 2005 [46] et réalisé dans des expériences sur les atomes froids en 2019 [47], suivant une configuration proposée en 2013 [48]. La localisation de bosons faiblement interactifs dans ce système a été rapportée [49]. Avec ces avancées dans les expériences, les études théoriques sur les atomes froids bidimensionnels dans des potentiels quasicristaux commencent également à gagner du terrain [50–52]. Dans les potentiels quasi-cristallins pour les bosons froids, les effets de localisation peuvent induire la phase de verre de Bose, qui est une phase isolante compressible. L'existence de la phase de verre de Bose a été proposée théoriquement à la fin des années 1980, d'abord en une dimension [53], puis également en dimensions supérieures [54]. Cependant, l'observation directe et non-ambigüe de la phase de verre de Bose dans les atomes ultrafroids reste un défi. Un obstacle majeur est la fluctuation thermique, car toutes les expériences sur les atomes froids sont

réalisées à une température finie. Les fluctuations thermiques peuvent entrer en compétition avec le (quasi)désordre et détruire la phase de verre de Bose. Il a été proposé que ce problème puisse être surmonté en utilisant un potentiel quasipériodique peu profond [38]. Pour un réseau profond, le modèle de liaisons fortes donne une bonne description et l'échelle d'énergie typique est l'énergie de couplage tunnel. Cette énergie est généralement assez faible et de même ordre de grandeur que la température dans les expériences typiques. Dans les potentiels quasi-cristallins peu profonds, l'échelle d'énergie pertinente est l'énergie de recul $E_r$. Il s'agit de la température limite du refroidissement laser et beaucoup plus élevée que la température typique des expériences d'atomes ultrafroids. De cette manière, l'effet de la température est relativement réduit et peut faciliter l'observation de la phase de verre de Bose. Dans cette thèse, nous présentons une étude théorique de la simulation quantique de quasicristaux bidimensionnels avec des atomes froids. Nous discuterons des propriétés des particules individuelles et des diagrammes de phase thermodynamiques pour des bosons bidimensionnels dans un potentiel quasi-cristallin peu profond. La structure de la thèse est la suivante.

Le chapitre 1 présente une revue du système à étudier, préparant ainsi le terrain pour les parties suivantes. Nous passons en revue la réalisation expérimentale et la configuration des atomes ultrafroids, ainsi que l'idée fondamentale de la simulation quantique, en soulignant comment les différentes méthodes de contrôle et de mesure dans les atomes ultrafroids en font une plateforme idéale pour la simulation quantique. Nous introduisons ensuite le phénomène de localisation dans les systèmes désordonnés. Nous passons ensuite en revue la découverte et les concepts des quasicristaux, montrant que la localisation peut également apparaître dans les quasicristaux, mais pas avec le même comportement que dans les systèmes désordonnés.

Le chapitre 2 se concentre sur les liquides quantiques de bosons, fournissant les bases théoriques pour les études ultérieures sur les bosons froids bidimensionnels, et introduit également l'algorithme de Monte Carlo par intégrale de chemin que nous avons largement utilisé pour les calculs numériques. Nous passons d'abord en revue les concepts de la condensation de Bose-Einstein (CBE) pour les bosons non interactifs. Ensuite, nous discutons le critère de Penrose-Onsager sur la façon d'étendre la définition de la CBE aux bosons en interactions. Nous donnons une brève présentation des approches théoriques largement utilisées pour les bosons condensés : l'équation de Gross-Pitaevskii et le spectre de Bogoliubov. Nous discutons le phénomène étroitement lié de la superfluidité et du modèle des deux fluides. Pour les bosons bidimensionnels, la transition superfluide a un caractère particulier. Elle appartient à la classe d'universalité de la transition BKT. Nous passons en revue ses propriétés de base et certains résultats théoriques, en particulier ceux qui seront utilisés dans les chapitres suivants. Ensuite, nous discutons des bosons dans des réseaux, avec ou sans désordre. Ainsi, nous voyons comment la phase d'isolant de Mott et la phase de verre de Bose peuvent apparaître pour les bosons interactifs. Les différentes phases introduites dans ce chapitre, y compris la superfluidité, le fluide normal, l'isolant de Mott et le verre de Bose, seront le sujet d'étude des chapitres suiv-

ants sur les bosons dans des potentiels quasicristaux. Enfin, nous donnons un bref aperçu de la méthode numérique de Monte Carlo par intégrale de chemin pour les bosons, y compris son optimisation appelée algorithme du ver.

Dans le chapitre 3, nous étudions les propriétés des particules individuelles dans le potentiel quasicristal bidimensionnel créé par plusieurs faisceaux laser disposés géométriquement de manière à ce que le potentiel total présente une symétrie de rotation interdite pour les cristaux normaux. Nous discutons d'abord les propriétés de localisation. Nous soulignons qu'une étude minutieuse de la localisation nécessite de voir comment le rapport de participation inverse évolue avec la taille du système. Grâce à cela, nous identifions des états localisés, étendus et également critiques. Nous étudions ensuite les structures de bande interdite. Pour la plus grande bande interdite, nous utilisons une approche de perturbation pour expliquer pourquoi cette bande interdite existe. Enfin, nous présentons également une image générale du spectre pour différents types de potentiels avec différentes symétries de rotation.

Le chapitre 4 présente notre étude sur les diagrammes de phase thermodynamique de bosons bidimensionnels dans un potentiel quasicristal, en utilisant la méthode de Monte Carlo par intégrale de chemin pour les calculs numériques. Nous identifions les différentes phases à l'aide de quelques paramètres d'ordre. Pour les isolants compressibles, le verre de Bose et le fluide normal, nous introduisons une stratégie pour les différencier. Nous discutons de l'importance des effets de taille finie pour obtenir un diagramme de phase thermodynamique correct. Par cette approche, nous utilisons les données de Monte Carlo pour localiser les frontières entre les différentes phases et ainsi obtenir les diagrammes de phase.

Dans le chapitre 5, nous résumons nos travaux de cette thèse et discutons plusieurs perspectives de recherches futures.

# Abstract

Quasicrystals are long-range-ordered solids without translational symmetry, showing rotational symmetries that are forbidden for normal crystals, for example 5 fold, 7 fold, 8 fold etc. Their discovery in the laboratory during the 1980s lead to a paradigm shift in crystallography, revolutionizing the basic idea on possible structure of solids [1–3]. Since then on, quasicrystals have attracted much attentions, owing to their intriguing properties, including for examples phasonic quasiparticles [4–6], transport properties [7–10], intricate energy spectrum [11–13], nontrivial topological order [14–18] and Anderson-like localization [19, 20]. A powerful tool to study the physical properties of quasicrystals is quantum simulation [21–23]. With the realization of ultracold atomic systems in the 1990s [24, 25] and the rapid developments thereon, a new playground of quantum many body physics has opened. In particular, the strong control over the physical parameters and the various measurement tools in a cold atomic system make it a promising platform for quantum simulation [26, 27]. A one-dimensional quasiperiodic potential in cold atoms experiments can be created by superimposing several laser beams with incommensurable periods. In the past years, cold atoms in one-dimensional quasiperiodic potentials have been studied extensively [20, 28–45]. A two-dimensional optical lattice giving a quasicrystal potential can also be created by certain geometrical arrangements of laser beams. This was first proposed theoretically in 2005 [46], and realized in cold atoms experiments in 2019 [47] following a configuration proposed in 2013 [48]. Localization of weakly interacting bosons in that system has been reported [49]. With these advancements in experiments, the theoretical studies of two dimensional cold atoms in quasicrystal potentials also start to gain momentum [50–52]. For cold bosons in quasicrystal potentials, localization effects may induce the Bose glass phase, which is a compressible insulating phase. The existence of Bose glass phase was proposed theoretically in the late 1980s first in one dimension [53] and then also in higher dimensions [54]. However, a direct undisputed observation of the Bose glass phase in ultracold atoms is still challenging. One big hindrance is the thermal fluctuation, as all cold atoms experiments are performed under a finite temperature. The thermal fluctuations may compete with the (quasi)disorder and destroy the Bose glass phase. It has been proposed that this issue may be overcome by using a shallow quasiperiodic potential [38]. For a deep lattice, the tight binding model gives a good description and the typical energy scale is the tunnelling energy. This energy

is usually quite small and of the same order of magnitude of the temperature in typical experiments. In shallow quasicrystal potentials, the relavant energy scale is the recoil energy $E_r$. This is the limiting temperature of laser cooling and much higher than the typical temperature of ultracold atoms experiments. In this way, the temperature effect is relatively decreased and may help the observation of Bose glass phase. In this thesis, we give a theoretical study of quantum simulation of two-dimensional quasicrystals with cold atoms. We will discuss the single particle properties and the thermodynamic phase diagrams for two dimensional bosons in a shallow quasicrystal potential. The structure of the thesis is as follows.

Chapter 1 gives a review of the system to be studied, setting up the stage for the following parts. We review the experimental realization and setup of ultracold atoms and the basic idea of quantum simulation, stressing how the various control and measurement methods in ultracold atoms allows it to be a good platform of quantum simulation. We give a introduction to the localization phenomenon in disordered system. We then review the discovery and concepts of quasicrystals, and showing that localization can also appear in quasicrystals, but not with the same behaviour as in disordered systems.

Chapter 2 focuses on the quantum liquids of bosons, giving the theoretical backgrounds for the following studies of two dimensional cold bosons, and also introduces the path integral Monte Carlo algorithm that we have heavily used for numerical calculations. We first review the concepts on Bose-Einstein condensation (BEC) for non-interacting bosons. Then we discuss the Penrose-Onsager proposal on how to extend the definition of BEC to interacting bosons. We give a brief explanation of the widely used theoretical approaches for condensed bosons: Gross-Pitaevskii equation and Bogoliubov spectrum. We discuss the closely related phenomemon superfluid and the two fluids model. For 2D bosons, the superfluid transition is of special character. It is in the universality class of the BKT transition. We review its basic properties and some theoretical results, in particular those that will be used in the following chapters. Then we discuss the bosons in lattices, with or without disorder. With this we see how the Mott insulator phase and Bose glass phase may appear for interacting bosons. The various phases introduced in this chapter, including superfluid, normal fluid, Mott insulator and Bose glass, will be the study subject of the following chapters for bosons in quasicrystal potentials. In the end we give a brief review of the path integral Monto Carlo numerical method for bosons, including its optimization called worm algorithm.

In chapter 3 we study the single particle properties of the two dimensional quasicrystal potential created by several laser beams, geometrically arrange in such a way that the total potential has a rotational symmetry that is forbidden for normal crystals. We first discuss the localization properties. We stress that a careful study of localization requires to see how the inverse participation ratio scales with system sizes. With that we identify localized, extended and also critical states. We then study the gap structures. For the largest gap, we use a perturbation picture to give a explanation on why that gap exists. In the end we also show the general picture of the spectrum for different kinds of potentials

with different rotational symmetries.

Chapter 4 shows our study on the thermodynamic phase diagrams of two dimensional bosons in a quasicrystal potential, using the path integral Monte Carlo method for numerical calculations. We identify different phases with a few order paramters. For compressible insulators Bose glass and normal fluid, we introduce a strategy to differentiate one from the other. We discuss why a careful finite size effect is indispensable to obtain a faithful thermodynamic phase diagram. With this preparation, we use the Monte Carlo data to locate the boundaries between various phases, and thus get the phase diagrams.

In chapter 5, we give a summary of our works in this thesis, and discuss several perspectives of future researches.

# Chapter 1

# Introduction

Macroscopic systems are made of atoms, neutral particles that are in perpetual motion. Atoms are in turn composed of electrons with negative charges and nucleus with positive charges. Although atoms are electrically neutral as a whole, there are electromagnetic interactions between the atoms due to dipole-dipole interaction, called Van der Waals interaction. The electrons moving around the nucleus can lead to an instantaneous electric dipole moment of an atom. The electric field created by this dipole then polarizes another atom far away. The polarized atom will then interact back with the original polarized atom. This dipole-dipole interaction gives an attractive force for atoms far apart. When atoms are near to each other with distance about the atomic radius, they are like hard spheres and have a repulsive interaction.

Macroscopic systems consists of a large number of atoms. This large number permits a statistical description of macroscopic systems. One can define a temperature describing how the entropy of a system changes with respect to its energy, as $1/T \equiv dS/dE$. Clearly, this physical quantity, temperature, is of pure statistical nature. A macroscopic system shows different properties at different temperature, in particular, the large total number $N$ of atoms in a macroscopic system permits us to define its thermodynamic phases. Let us consider a gas of neutral atoms with short range binary interactions. Of course, if the temperature is very high then the electrons can escape from the Coulomb attraction of the nucleus and the macroscopic system becomes a plasma of electrons and nuclei. In this case the atomic picture breaks down. Suppose we have a relatively high temperature where the atomic picture still holds, then the atoms are in a gas phase. A dilute gas is well described by the elementary kinetic theory of gases. The thermodynamics of the atoms are the usual ones of a classical gas. Its specific heat is independent of temperature $T$, and for fermions with spin, the thermodynamic average of spins has a susceptibility that scales as the inverse of temperature $T$, which is the Curie's law. As temperature decreases, the system can undergo a first order phase transition into a liquid state, where the atoms have stronger correlations. As the temperature further decreases, the system may undergo another first order phase transition into a solid phase. This is

what happens for almost all cases, with the only exceptions being the isotopes of helium, $^3$He and $^4$He, which remain in a liquid phase down to the lowest temperatures. The small mass of helium leads to a large quantum zero-point fluctuation, which prevents the helium from solidifying. Thus helium remains in a liquid phase at low temperature where quantum effects must be considered [55]. The statistics of the atoms are no longer given by the Boltzmann statistics. The fermions like $^3$He which obey Fermi-Dirac statistics, and the bosons like $^4$He which obey Bose-Einstein statistics, have very different physical properties. From a broader perspective, the electrons in metals can also be viewed as a quantum liquid. Due to the small mass of electrons compared to atoms, the quantum degeneracy temperature of electron is much higher and is typically about $\sim 10^4$K. So the conduction electrons are in the quantum regime at room temperature. The study of the physics of quantum liquids gave rise to the far reaching concepts of elementary excitations [56–58], with the crucial observation that each of the low lying many body eigenstates of quantum liquids can be considered as a combination of elementary excitations, which makes low temperature quantum liquids in some aspects better understood than classical liquids [55]. An elementary excitation could be of boson type or fermion type, and has a dispersion relation $\epsilon(p)$ between its energy $\epsilon$ and momentum $p$. Quantum liquids at low temperatures show novel macroscopic quantum phases like superfluidity [59] for bosons and superconductivity [60] for fermions.

The above mentioned systems like electrons and liquid helium are strongly interacting and there physical parameters like the interaction strengths are not well controlled. This situation was changed in the 1990s, when the ultracold atomic systems are realized in experiments [24, 25], thanks to the developments of cooling techniques. With them one can get dilute systems that are well controlled. The dilute atomic gases are cooled down to a temperature where quantum effects must be taken into account. After the first achievement of Bose-Einstein condensation (BEC) with bosonic gas, the quantum degenerate fermionic gas was also realized a few years later [61–64]. With these achievements, ultracold atoms have become a new type of quantum many body systems. It allows for various controlling and probing methods. The interaction between the atoms and laser can be used to create external potentials for the atoms, which may confine the atomic movements to one or two dimensions and can be used to design a certain periodic [65, 66] or quasi-periodic [46, 67, 68] potential for the atoms. The interaction between the atoms can be tuned via the Feshbach resonance [69, 70]. The momentum distribution of the atomic gas can be directly measured in a time-of-flight experiment [71]. The new systems of ultracold atoms also give rise to new physics. A quantum phase transition between superfluid and Mott insulator was observed by tuning the depth of optical lattice [71]. By tuning the Feshbach resonance to the unitary point where the interaction strength is infinitely large, one length scale related to the interaction strength disappears and one observes the atomic gases display universal thermodynamics [72–75]. If one tunes the Feshbach resonance across the unitary point, a BEC-BCS crossover can be observed for fermionic atoms [76–79].

The macroscopic quantum phases like superfluid and superconductivity only

exist at low temperatures, while the critical temperatures depend on the density. Above a certain critical temperature, theses phases are destroyed by the thermal fluctuation. The basic idea of thermal fluctuation can be well explained in a classical system of atoms. Temperature is bounded below by 0K. At non-zero temperature, atoms are all in thermal motions. Thermal motions are random, and the motions are stronger at higher temperatures. These thermal motions of small atoms can be visibly observed in the Brownian motion experiment, where one put a pollen into water and then observe the pollen which is a much larger object than the atoms. The pollen does not stay at rest in the water, but undergoes a random movement called Brownian movement. This originates from the collisions between the pollen and the many moving molecules of water surrounding it. The net effect of the collisions is a random force experienced by the pollen. If we neglect the short correlation time scale of the collisions, different collisions are independent events and the random force is a white noise. The random walk of the pollen has a mean squared distance proportional to the time $t$, as $< x^2 >= 2Dt$, where $x$ is the displacement of pollen in $x$ direction and $D$ is the diffusion coefficient. On the other hand, if one drags a pollen with constant velocity $v$ in water, the pollen experiences a friction force, in the opposite direction of the velocity and proportional to the velocity value as $f = -v/\mu$, where $f$ represents the friction force and $\mu$ is called the mobility. This friction force also originates from the collisions between the moving pollen and the atoms in the water. It is thus not surprising that the diffusion coefficient $D$ and mobility $\mu$ can be related by the Einstein relation [80] $D = k_B \mu T$, where $k_B$ is the Boltzmann constant and $T$ is the temperature. This relation is an example of the fluctuation-dissipation theorem. The presence of temperature $T$ in this relation clearly shows the thermal nature of Brownian motion. The random movements of the pollen is a typical example of thermal fluctuation, where randomness is introduced by the finite temperature. In the following chapters, we will see how thermal fluctuations could destroy long range phase coherence of matter waves, as what happens when a superfluid becomes normal fluid when the temperature is increased above the critical temperature.

Another possibility of destroying the long-range coherence besides thermal fluctuation is the randomness of the media through which the wave propagates. This is what happens in the physics of Anderson localization [81]. Originally Anderson localization was discussed in the context of the movements of electrons in a crystal. It is well known that in a perfect periodic crystal, the single particle eigenstates of the electron's wavefunction are the Bloch waves, which are just plane waves modulated by a periodic function. Anderson conjectured out that in the presence of strong enough disorder in the crystal, a conductor can become an insulator. This is actually a general phenomenon of waves propagating in a disordered media. The destructive interference of waves scattered by the disorders prevents the wave from propagating far away and we then have a localized wave.

Quasicrystals play an intermediate role between periodic systems and disordered systems. Solid state alloys with quasicrystal structure were discovered by chance in 1984 [1]. They are long-range-ordered, while have no translational

symmetry. On the one hand, unlike periodic crystals, quasicrystal potentials can lead to localization effects [19]. On the other hand, the localization physics of quasicrystals are quite different from the Anderson localization of disordered systems. We can study the physical properties of quasicrystals by quantum simulation, thanks to the strong control over the physical parameters in a cold atomic system. In cold atoms experiments, a quasicrystal optical lattice potential can be realized with relatively easy arrangements of laser beams. In one-dimension, a quasiperiodic potential can be created by superimposing several laser beams with incommensurable periods. In the past years, these one-dimensional quasiperiodic systems of cold atoms have been extensively studied [20, 28–45]. Studying quantum fluids in a 2D quasicrystal optical lattice was first theoretically proposed in 2005 [46]. In 2019, this was realized in cold atoms experiments [47] following a configuration proposed in 2013 [48]. In particular, observation of a localization phase of weakly interacting bosons in that system has been reported [49]. With these advancements in experiments, the theoretical study of two dimensional cold atoms in quasicrystal systems is just starting [50–52] and many questions remain open. For example, we want to know how robust the localization phase is against thermal fluctuations. The physics in 2D quasicrystals have fundamental differences compared to the 1D cases, as we know the effects of thermal and quantum fluctuations in 1D systems are generally more significant. For instance, in a homogeneous system, there is no superfluidity at any finite temperatures for bosons in 1D, while in 2D there is a finite temperature superfluid-to-normal fluid transition which is a topological BKT transition. Better theoretical understandings of the physics of cold atoms in 2D quasicrystals are required, which may be useful guides for further experimental works.

The main subject of this thesis is the cold atoms in a two dimensional quasicrystal potential. In this chapter, we first review the basic ideas and experimental setups of ultracold atomic systems, and then give a review of the localization physics and quasicrystal systems, thus set up the stage for the study of the combination of the two in the following chapters.

## 1.1 Cold atoms and quantum simulation

Cold atoms are experimental systems where one can control various kinds of physical parameters. These controls of parameters make cold atoms one of the best platforms of quantum simulation, where one directly design an experimental setup corresponding to a certain theoretical model and then measure the physical observables. These rich methods of controls in cold atomic systems are thanks to the internal degrees of freedoms of the atoms.

### 1.1.1 External and internal variables

Atoms are composite objects containing the nucleus and electrons surrounding the nucleus. For a dynamical description of atoms, it is helpful to make a

separation between the external variables and internal variables [82]. While the relative motions between the electrons and nucleus are subject to the Coulomb interaction, the motion of the atoms as a whole are subject to the Van der Waals interaction, thus a separation between these two kinds of dynamical variables are intuitively quite acceptable.

We illustrate this idea by taking the example of an atom composed of the nucleus and one electron. We denote the position variables of the electron and nucleus as $\mathbf{r}_e$ and $\mathbf{r}_N$, their masses as $m_e$ and $m_N$, and their momenta as $\mathbf{p_e}$ and $\mathbf{p_N}$. In quantum mechanics, they have the standard canonical commutation relations as

$$[r_{e,i}, p_{e,j}] = i\hbar\delta_{ij}, \quad [r_{N,i}, p_{N,j}] = i\hbar\delta_{ij}, \quad i,j = x,y,z \tag{1.1}$$

and all the other commutators are zero. The Hamiltonian is the summation of the kinetic terms and the interaction between the electron and the nucleus,

$$H = \frac{\mathbf{p_e}^2}{2m_e} + \frac{\mathbf{p_N}^2}{2m_N} + V(\mathbf{r}_e - \mathbf{r}_N). \tag{1.2}$$

We introduce the new variables

$$\mathbf{R} = \frac{m_e\mathbf{r}_e + m_N\mathbf{r}_N}{M}, \ \mathbf{P} = \mathbf{P_e} + \mathbf{P_N}, \tag{1.3}$$

$$\mathbf{r} = \mathbf{r}_e - \mathbf{r}_N, \quad \frac{\mathbf{p}}{m} = \frac{\mathbf{p_e}}{m_e} - \frac{\mathbf{p_N}}{m_N}, \tag{1.4}$$

where $M = m_e + m_N$ is the total mass of the atom and $m = \frac{m_e m_N}{M}$ is the reduced mass. The variables $\mathbf{R}$ and $\mathbf{P}$ are the position and momentum of the center of mass, and they are called external variables. The variables $\mathbf{r}$ and $\mathbf{p}$ describe the relative motion between the electron and the nucleus, and they are called internal variables. It can be easily checked that these new variables obey the commutation relations

$$[r_i, p_j] = i\hbar\delta_{ij}, \quad [R_i, P_j] = i\hbar\delta_{ij}, \quad i,j = x,y,z, \tag{1.5}$$

while all other commutators are zero. So this transformation is a canonical transformation which conserves the canonical commutation relations.

The Hamiltonian can be rewritten with the new variables as

$$H = \frac{\mathbf{P}^2}{2M} + \frac{\mathbf{p}^2}{2m} + V(\mathbf{r}). \tag{1.6}$$

We can see from this Hamiltonian that the dynamics of external and internal variables are separated.

As we will see in the following parts, the separation of internal and external degress of freedoms of atoms goes through the whole discussion of cold atomic physics. If the atoms were elementary particles with no internal structure, there would be much less ways to play with the systems. It is the internal degree of freedom that allows people to have so many ways to control and probe the atoms.

### 1.1.2 Ultracold atoms

The internal variables are governed by quantum mechanics, which lead to the discrete atomic spectra. For the interaction between atoms and monochromatic lasers, the internal degrees of freedom are usually well described by a two level system, with a ground state conventionally denoted as $|g\rangle$ and an excited state conventionally denoted as $|e\rangle$ [82]. For example, for interaction processes between an atom and a laser with frequency $\omega$, due to the conservation laws, only few states can be reached from the ground state with nonzero matrix elements. Due to the fact that the electromagnetic field is a vector field, according to Wigner-Eckart theorem, a state with angular momentum $l$ can only transit to another state with angular momentum $l$, $l-1$ or $l+1$. In addition, photons are spin-1 particles, but with only transverse polarizations, so 2 states out of them are involved in the reachable final states. Further selection rules can be obtained by picking a certain polarization of the laser and taking into account the parity symmetry. In the end, the excited states with excitation energy too far from the energy of a single photon $\hbar\omega$ have little effects and we can only consider the states that are almost in resonance with the laser, i.e. an excitation energy $\hbar\omega_0$ close to $\hbar\omega$. If $\omega$ is smaller than $\omega_0$, the laser is called red detuned; if $\omega$ is larger than $\omega_0$, the laser is called blue detuned.

At room temperature, the external variables of atoms are well described by classical physics, which gives the equipartition rule and leads to a constant specific heat. As the temperature gives the scale of the kinetic energy of the atom, the atomic velocity scales as square root of temperature, and with low enough temperature, it is possible to have the atomic momentum small enough that the de Broglie wavelength $\lambda = h/p$ is comparable or larger than the typical inter-atomic distance. Then the atoms' external variables should be described by quantum mechanics. Ultracold atoms fall into this category. They have a temperature of the order to tens to hundreds of nK, corresponding to a thermal de Broglie wavelength of the order $\lambda_T \sim 10^2 - 10^3 nm$ . This is the same order of magnitude as optical wavelengths, which is also the typical inter-particle distance in these systems.

#### 1.1.2.1 Laser cooling

The quantum degenerate ultracold atomic systems are realized in experiments thanks to the developments of cooling techniques for atomic systems. A first stage of cooling is usually achieved by the laser cooling technique. An atom placed in counter-propagating lasers can be cooled down due to the Doppler effect [83], see Fig. 1.1. If we choose the laser frequency $\omega$ to be red detuned, i.e. $\hbar\omega$ is a bit smaller than the transition energy between the electron ground and excited states, then due to the Doppler effect, the atom will be more likely to absorb a photon when it moves towards the laser source, and gain the momentum of the photon which is in opposite direction to the atomic momentum. This makes the atom experience a friction -like force, which decreases the atomic velocity. When the excited electron decays back into the ground state through

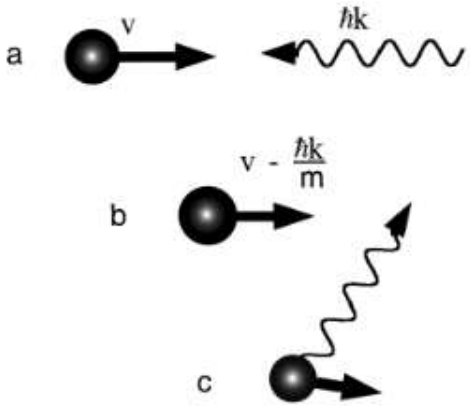


Figure 1.1: (a) An atom with velocity $v$ encounters a photon with momentum $\hbar k$; (b) after absorbing the photon, the atom is slowed by $\hbar k/m$; (c) after re-radiation in a random direction, on average the atom is slower than in (a). This figure is from Ref. [84]

spontaneous emission, the atom gains the opposite momentum of the emitted photon. The spontaneous emission is however isotropic and thus the net effect of average momentum change is zero. On the other hand, the spontaneous emissions in random directions give a non-zero average of the square of velocity. In the end, the atoms reach an equilibrium state where cooling due to photon absorbing and heating up due to photon emission fluctuations balance each other. The atoms are just like Brownian particles. The colliding and absorbing of photons give an effective friction force and the spontaneous emissions give the random kicks. For a well-chosen detuning, the lowest equilibrium temperature that can be reached is given by the natural linewidth $\Gamma$ of the excited state as $T = \hbar\Gamma/2k_B$. In experiments, this could be of the order of hundreds of $\mu K$.

Further cooling below this Doppler limit can be achieved using sub-Doppler cooling techniques, for example the Sisyphus mechanism [85, 86]. The later uses the energy shifts and cycles of pumping and transitions betweeen Zeeman sublevels. This can in the end reach a natural temperature limit of laser cooling techniques, given by the recoil energy of the photon emission as

$$E_r = \frac{\hbar^2 k^2}{2m} \tag{1.7}$$

where $k$ represents the wavenumber of the laser and $m$ is the atomic mass. If an atom at rest emits a photon with momentum $\hbar k$, the atom gains a recoil momentum $\hbar k$ in the opposite direction. The corresponding kinetic energy is this recoil energy $E_r$. This gives a temperature of the order of $\mu K$ in experiments.

#### 1.1.2.2 Trapping

The idea of slowing down the atoms by absorbing photons can also be used for trapping of atoms. A widely used trapping method for neutral atoms is the magneto-optical trap (MOT) [87–89], utilising both the optical and magnetic fields. The idea is illustrated in Fig. 1.2 for a 1D trapping in the $z$ direction. Assume the atom internal state has a transition from ground state with angular momentum $J_g = 0$ to excited states with angular momentum $J_e = 1$. The magnetic field leads to the Zeeman splitting between the excited states with different angular momentum $M_e$ in the $z$ direction. The magnetic field is chosen to be spatially inhomogeneous, and as a result, the relative energies between the Zeeman sub-levels depend on the positions as well. The lasers propagating in the two directions are circularly polarized in opposite directions. As shown in Fig. 1.2, the laser propagating from right to left has $\sigma^-$ polarization, and the laser propagating from left to right has $\sigma^-$ polarization. Due to the conservation of angular momentum in light matter interaction processes, the $\sigma^-$ polarized light can only excite the atom from the ground state to the $M_e = -1$ state, and the $\sigma^+$ polarized light can only excite the atom from the ground state to the $M_e = +1$ state. If we take the laser to be red-detuned from the $M_e = 0$ state with detuning $\delta$, then at the trap center all three Zeeman sub-levels are detuned from the laser. For atoms to the right of the trap center, say at point $z'$ in Fig. 1.2, the state $M_e = -1$ is close to resonance and the state $M_e = +1$ is further from resonance, and the atom absorbs more photons with $\sigma^-$ polarisation. Since the $\sigma^-$ polarised light propagates from right to left, the atom is pushed towards the trap center. On the other hand, if an atom is at a position $z'' < 0$ to the left of the trap center, it absorbs more photons with $\sigma^+$ polarization as the state $M_e = +1$ is closer to resonance, so the atom is pushed to the right towards the trap center. In this way, the cooling and trapping of the atomic cloud is achieved simultaneously in the MOT.

#### 1.1.2.3 Evaporative cooling

Yet the temperature reached by laser cooling methods is not low enough to reach the quantum degeneracy with phase space density $D \equiv n\lambda_T^3 \gtrsim 1$. Lower temperatures of the atomic gases are realized in experiments by evaporative cooling, see Fig. 1.3. By gradually decreasing the depth of the trap, the atoms with large velocities will escape the trap. Then the remaining atoms can reach a new thermal equilibrium through atom-atom interactions, and this new equilibrium has a lower temperature than before. Although a number of the atoms is lost during the evaporation process, the decrease of particle number density $n$ is compensated by a faster increase of thermal de Broglie wavelength $\lambda_T$ and the phase space density $D \equiv n\lambda_T^3$ is increased. Thus the cooling is efficient enough to reach the quantum degeneracy threshold. In the end, it gives the temperature of tens to hundreds of nK where lies the ultracold atoms regime.

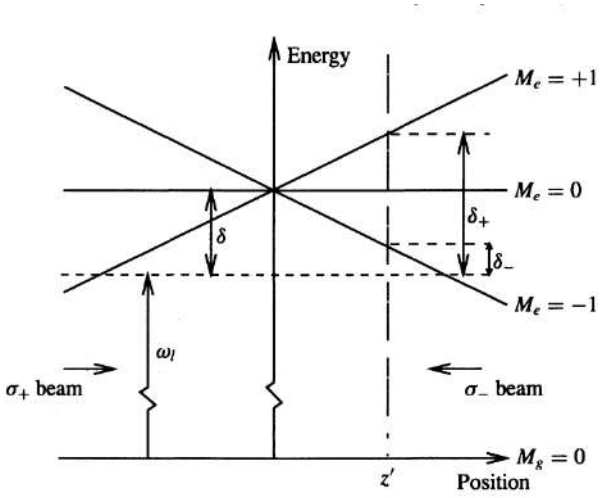


Figure 1.2: Arrangement for a MOT in 1D. The horizontal dashed line represents the laser frequency seen by an atom at rest in the center of the trap. Because of the Zeeman shifts of the atomic transition frequencies in the inhomogeneous magnetic field, atoms at $z = z'$ are closer to resonance with the $\sigma^-$ laser beam than with the $\sigma^+$ beam, and are therefore driven toward the center of the trap. This figure is from Ref. [90]

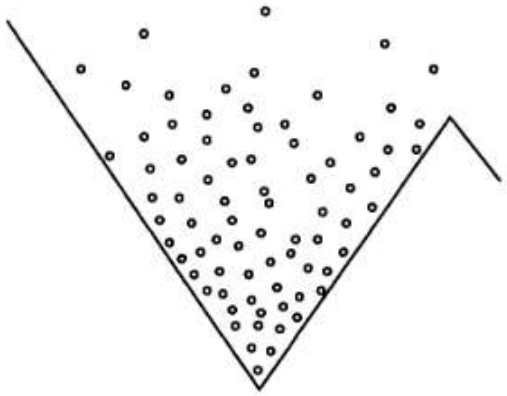

Figure 1.3: Principle of the evaporation technique. Once the trap depth is lowered, atoms with energy above the trap depth can escape and the remaining atoms reach a lower temperature. This figure is from Ref. [90]

#### 1.1.2.4 Hamiltonian of atomic gases

The achievements of methods to cool and trap atoms with laser light was recognized by the award of the Nobel prize in 1997 [84, 91, 92]. Thanks to the developments of these cooling and trapping techniques, the ultracold atomic systems have been realized in experiments during the 1990s. A landmark is the observation of Bose-Einstein condensation using dilute ultracold gases in 1995 [24, 25], characterizing the quantum degeneracy of the bosons. This opened a new field of experimental study over quantum systems, and was recognized by the award of the Nobel prize in 2001 [93, 94]. An experimental setup for the atoms confined by lasers and magnetic fields are sketched in Fig. 1.4. The confined atoms can be sustained a sufficiently long time, such that the system can be considered in an equilibrium state with a certain temperature $T$. Since the interaction and statistics of the atoms are quantum, the physics is characterised by the Hamiltonian,

$$\hat{H} = \sum_i \frac{\hat{\mathbf{p}}_\mathbf{i}^{\,2}}{2m} + \sum_i V(\hat{\mathbf{r}}_i) + \sum_{i<j} U(\hat{\mathbf{r}}_i - \hat{\mathbf{r}}_j), \tag{1.8}$$

with $m$ the atom mass, $i$ and $j$ go over the number of atoms. The momentum operator $\hat{\mathbf{p}}_\mathbf{i}$ and position operator $\hat{\mathbf{r}}_i$ refer to the external variables of the atoms, i.e. dynamic variables of their centers of mass. The Hamiltonian contains the kinetic term $\sum_i \frac{\hat{\mathbf{p}}_\mathbf{i}^{\,2}}{2m}$, the external potential $\sum_i V(\hat{\mathbf{r}}_i)$ and the interaction between the atoms $\sum_{i<j} U(\hat{\mathbf{r}}_i - \hat{\mathbf{r}}_j)$. Here we only consider two-body interactions as the ultracold atomic gases are dilute. These terms in the Hamiltonian are all operators of the external variables of the atoms. As we will show, the internal states of the atoms allow strong control over the Hamiltonian of the external variables.

#### 1.1.2.5 Atom-atom interactions

The interaction term $U$ describes 2-body scattering processes for dilute atomic gases, coming from the Van de Waals interactions between the atoms, as discussed above. Just like what we have done for separation of internal and external variables for electron and nucleus, a 2-body scattering process can be treated by separating the center of mass motion and the relative motion of the two scattering objects. The center of mass motion is just as trivial as a free particle and is thus eliminated from the problem by taking the center of mass reference frame. The scattering properties are then characterized by the relative motion of the two scattering objects. For isotropic interaction $U$, the angular momentum $l$ of the relative motion is a good quantum number during the scattering. The scattering amplitude can be decomposed into a summation of partial waves amplitudes for different angular momentum. Scattering in isotropic potential can be thus reduced to solving a one-dimensional Schrödinger equation in semi-infinite space. The angular momentum $l$ amounts to a centrifugal potential term in addition to the bare interaction potential. This centrifugal potential is proportional to $\hbar^2 l(l+1)$, i.e. the eigenvalue of the square of the

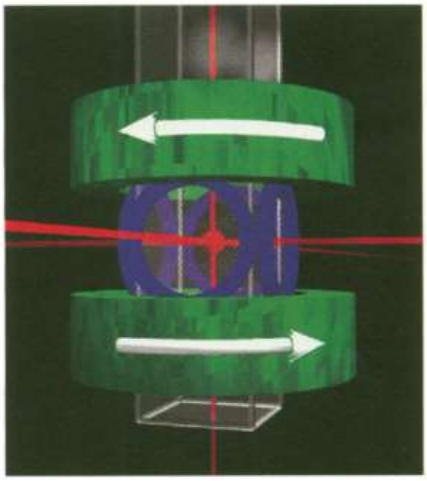

Figure 1.4: Experimental setup for a cold atom system. Six laser beams intersect in a glass cell, creating a magneto-optical trap. The coils generating the fixed quadrupole and rotating transverse components of the time orbiting potential trap magnetic fields are shown in green and blue, respectively. This figure is from Ref. [24]

angular momentum operator. It is zero for s-wave scattering with angular momentum $l = 0$. At low temperature, only the s-wave scattering needs to be considered because partial waves with higher angular momentum are strongly suppressed due to the centrifugal energy. A typical centrifugal energy barrier for $l = 1$ corresponds to a temperature $\sim 1mK$, much higher than the temperature regime of ultracold atomic systems. The s-wave scattering can be characterised by a quantity $a_{sc}$ with the dimension of length, called scattering length. It is related to the scattering amplitude $f$ in the low energy limit as

$$f(k \to 0) = -a_{sc} \tag{1.9}$$

where $k$ is related to the energy $E$ as $E = \frac{\hbar^2 k^2}{2\mu}$, while $\mu$ is the reduced mass. The sign of scattering length $a_{sc}$ characterizes the sign of interaction: the interaction is repulsive for positive scattering length, and attractive for negative scattering length.

#### 1.1.2.6 Feshbach resonance

This scattering length for atomic collisions can actually be tuned in experiments, thanks to the internal states of the atoms, using so-called Feshbach resonances [95]. The colliding atoms can have different kinds of initial internal states. Under the spirit of Born Oppenheimer approximation, different kinds of initial states give different effective interaction potentials between the two

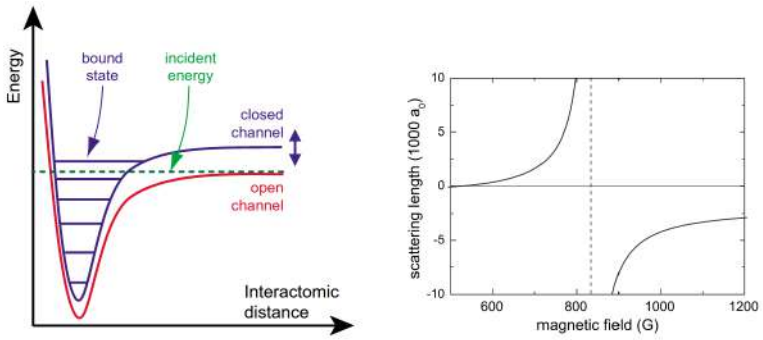


Figure 1.5: Left: The two-channel model for a Feshbach resonance. Atoms prepared in the open channel, corresponding to the interaction potential, undergo a collision at low incident energy. In the course of the collision, the open channel is coupled to the closed channel. When a bound state of the closed channel has an energy close to zero, a scattering resonance occurs. The position of the closed channel can be tuned with respect to the open one, e.g., by varying the magnetic field $B$. Right: Magnetic field dependence of the scattering length between the two lowest magnetic substates of $^6$Li with a Feshbach resonance at $B_0 = 834G$ and a zero crossing at $B_0 + \Delta B = 534G$. The background scattering length $a_{bg} = -1405a_B$ is exceptionally large in this case ($a_B$ the Bohr radius). This figure is from Ref. [26]

atoms, which are referred to as different collision channels. Figure 1.5(left) gives a sketch of a two-channel collision. There is an open channel, where the colliding atoms are initially prepared. The other channel, called the closed channel, has an energy at infinitely large distance larger than the initial energy of the two colliding atoms in the open channel. It has discrete bound states with energies lower than the energy limit at infinite large distance. One of the bound states may have an energy close to the initial energy of the open channel, and the two atoms in the open channel will undergo a scattering resonance with this bound state. The scattering amplitude of the resonant scattering is controlled by the energy difference between the colliding atoms in the open channel and the resonant bound state in the closed channel. If the two channels have different magnetic moments, the relative position of the closed channel bound state can be tuned by varying an external, uniform magnetic field. As a consequence, the scattering length $a_{sc}$ can be tuned with this method called Feshbach resonance. In particular, it is possible to reach the unitary point where the scattering length $a_{sc}$ is infinite and go over this point to change the sign of interaction from attractive to repulsive or vice-versa, see Fig. 1.5(right).

#### 1.1.2.7 Optical lattices

In addition to the interaction term $U$ in the Hamiltonian (1.8), the external potential term $V(\mathbf{r})$ can also be well controlled in the experiments. Although an atom is neutral as a whole, it can still interact with electro-magnetic fields, i.e. lasers, via its internal variables, which creates an effective external potential experienced by its external variables. This can be understood in a semi-classical picture. The laser shining on an atom polarizes the atom, and induces a dipole moment $\mathbf{d}$ proportional to the electromagnetic field $\mathbf{E}(\mathbf{r})$. The dipole then interact with the laser field and gives a dipole force $\mathbf{F} = \mathbf{d}\cdot\nabla\mathbf{E}(\mathbf{r}) \propto \nabla|\mathbf{E}(\mathbf{r})|^2$, i.e. the force is proportional to the gradiant of the laser field intensity. Consequently, the effective external potential due to the dipole force is just proportional to the intensity as $V(\mathbf{r}) \propto I(\mathbf{r})$. In addition, the sign of potential $V(\mathbf{r})$ is controlled by the detuning $\delta$ of the laser: if the laser is red detuned with $\delta < 0$, the potential is attractive where the laser intensity $I(\mathbf{r})$ is large; if the laser is blue detuned with $\delta > 0$, the potential is repulsive where the laser intensity $I(\mathbf{r})$ is large.

This allows to optically design potentials on purpose. For instance, overlapping two counterpropagating coherent lasers will give a standing wave with spatial period as half of the laser wavelength $\lambda$. Taking the propagation direction of the lasers as the $z$ direction, the intensity of the standing wave along $z$ direction is proportional to $sin^2(kz)$. The optical potential can be written as $V(z) = V_0 sin^2(kz)$, where $k = 2\pi/\lambda$ is the wave number of the lasers and $V_0$ represents the laser intensity. This is a periodic potential along $z$ direction, with spatial period $a = \lambda/2$. This gives a one-dimensional optical lattice. Two-dimensional or three-dimensional optical lattices can be created using multiple pairs of laser beams, see Fig 1.6. They are usually in orthogonal directions, and have no interference between different directions, due to a slight frequency shift. Then the total potential in three dimensions is just a summation of three one-dimensional potentials

$$V(x, y, z) = V_0[sin^2(kx) + sin^2(ky) + sin^2(kz)] \tag{1.10}$$

Atoms in this periodic potential of optical lattice can mimic the electrons in the periodic potential created by solid crystals, see Fig. 1.7. The absolute values of the physical parameters in the two systems are different by several orders of magnitude: the typical lattice constant in solid crystal is of order Å while the optical lattice constant is half of the laser wavelength and of the order $\mu$m; the typical temperature of electrons in solid is $\sim 10^2$K while the temperature for ultracold atoms is about $10^{-8}$-$10^{-7}$K; the mass of an atom is thousands of times heavier than the mass of an electron. However, what matters are the ratios of the various physical parameters, which can be of the same order for the two system, and then the quantum degenerate cold atomic gases in optical lattices are governed by the same physics as the electrons in crystals. For example, the atomic wavefunctions can be described by the Bloch waves, and Bloch oscillations in optical lattices have been observed [96, 97]. With deep optical lattices, one can reach a strongly-correlated lattice system [98]. Using the Wannier functions as the basis, one can develop the tight binding lattice model.

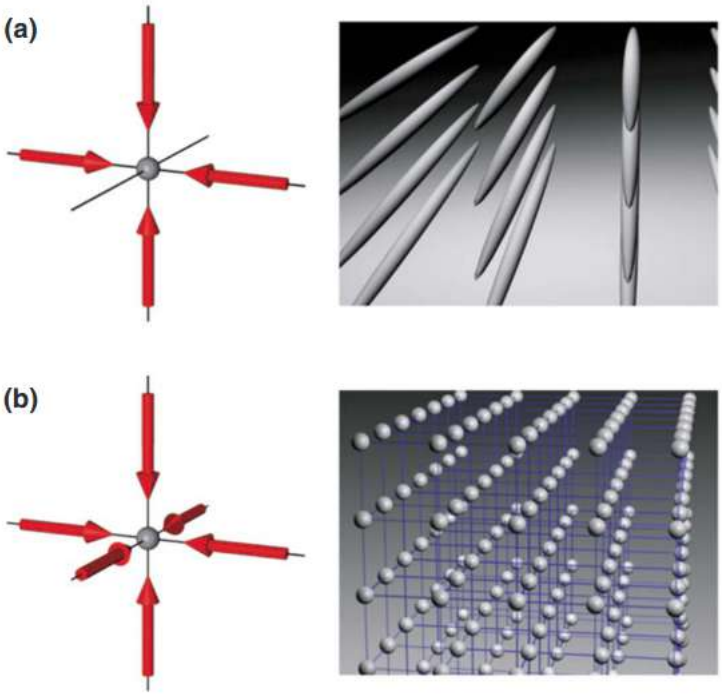


Figure 1.6: Optical lattices.(a)Two- and (b) three-dimensional optical lattice potentials formed by superimposing two or three orthogonal standing waves. For a two-dimensional optical lattice, the atoms are confined to an array of tightly confining one-dimensional potential tubes, whereas in the three-dimensional case the optical lattice can be approximated by a three-dimensional simple cubic array of tightly confining harmonic-oscillator potentials at each lattice site. This figure is from Ref. [26]

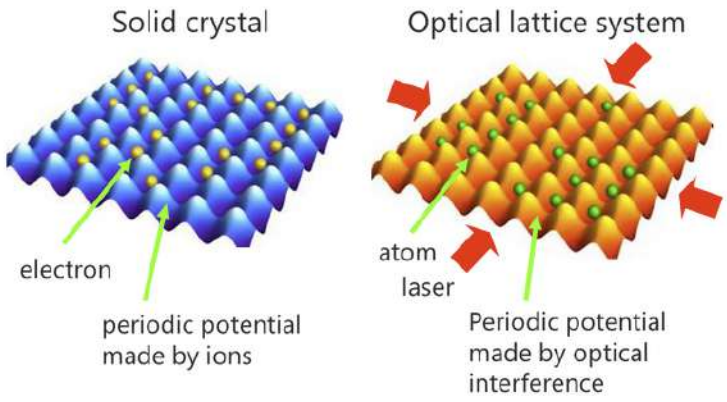


Figure 1.7: Left: periodic potential experienced by electrons in a crystal. Right: periodic potential experienced by atoms in a optical lattice. This figure is from Ref. [100]

The main physics is given by the hopping between nearest neighbours and on-site interactions. This leads to the Hubbard model, widely used in condensed matter physics, for example in the study of Mott insulator transitions and high temperature superconductors [99].

The optical lattice potential can also be used to confine the atoms to lower dimensions. For deep optical lattice potentials, the confinement on a single site can be approximated by a harmonic trap. The trapping frequency $\omega$ is related to the potential amplitude $V_0$ as $\hbar\omega = 2E_r(V_0/E_r)^{1/2}$, where $E_r$ is the recoil energy Eq. 1.7. If all the other energy scales of the atomic gas are much smaller than $\hbar\omega$, then the atoms are effectively confined in a two-dimensional system. Likewise, effective one-dimensional systems can be created by two strong confining optical potentials.

In an optical lattice, the dimension, the potential amplitude and spatial period are all controllable. The good control over the external potential term and interaction term in the Hamiltonian (1.8) makes the ultracold atomic systems a good platform for quantum simulation.

### 1.1.3 Quantum simulation

Generally speaking, solving a quantum mechanical problem could be challenging both analytically and numerically, in particular in the presence of strong correlations. From the analytical perspective, only few models are exactly solvable. Most of the theoretical problems can only be dealt with by certain approximation methods. However, there are many problems that cannot be correctly analysed by any known approximations. For example, some strongly correlated materials could be beyond the scope of mean field theory. Another approach to target a quantum mechanical problem is by numerical calculation. Nevertheless,

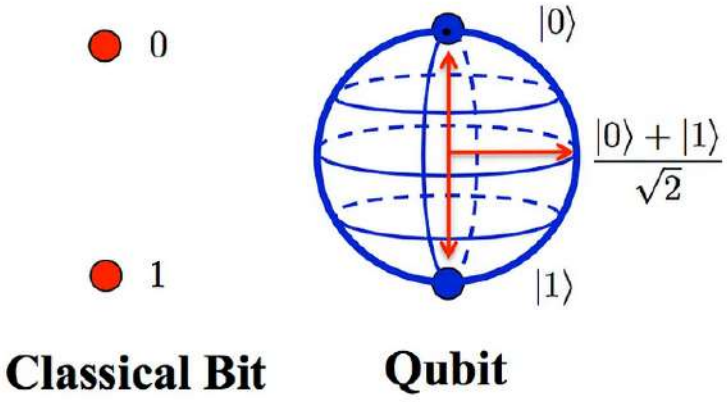


Figure 1.8: Left: a classical bit, which has two states 0 and 1. Right: a qubit which lives on a Bloch sphere. This figure is from Ref. [101]

there is a fundamental difficulty here, which comes from the fact that people calculate a quantum mechanical problem using classical computers. A classical computer is based on the information unit classical bit, which is just a two state object. The two states of a classical bit are usually called as 0 and 1. However, a quantum state lives in the Hilbert space. For instance, a quantum spin $\frac{1}{2}$, also referred to as a qubit, lives on a Bloch sphere, which is a two dimensional complex vector space spanned by states $|0\rangle$ and $|1\rangle$, see Fig. 1.8. As a consequence, a quantum spin system with $N$ spin $\frac{1}{2}$ will give a Hilbert space with dimension $2^N$. A general quantum state is described by a $2^N \times 2^N$ density matrix. If we store the quantum states by classical bits, the number of bits required hence grows exponentially with the size of the spin system. One way of solving this problem is to make the computer itself quantum [21], where one uses the quantum bit, or qubit, for calculations of quantum mechanical problems. This is the idea of quantum computation.

#### 1.1.3.1 Digital quantum simulator

A quantum simulator is a quantum system onto which one can map the theoretical model one wants to study. Of course this simulator should not be as complicated as the original real system from where the theoretical model was extracted in the first place, otherwise we gain nothing by this loop. The logic is that we first get the theoretical model which is a great simplification of the real-life objects but is expected to capture its core physics we are interested in. Then this theoretical model could be mapped to by a quantum simulator and the physics of this model can be directly measured. Suppose we want to study the time evolution of a quantum state $|\phi(0)\rangle$. We can map this state into state $|\psi(0)\rangle$ of the quantum simulator and map the Hamiltonian of the

system $H_{sys}$ into the Hamiltonian of the simulator $H_{sim}$, then in the end map the final state of the simulator $|\psi(t)\rangle$ back to $|\phi(t)\rangle$, see Fig. 1.9. The quantum simulator should be a controllable system: the initial state can be prepared, the Hamiltonian of the simulator can be engineered and the final state can be measured [23].

A digital quantum simulator is a universal machine. The quantum states are encoded using the qubits. The unitary transformation $U$ is implemented by the application of a sequence of qubit gates. One just needs to re-register and re-program the qubits and gates to simulate different systems. In this sense it is a quantum computer. The digital simulator would be optimised in a general way, not specific to any particular system.

#### 1.1.3.2 Analog quantum simulator

Another approach to simulate quantum systems is analog quantum simulation, where the simulator directly mimics the model to be simulated. It can be viewed as a quantum computer for a single Hamiltonian. An experimental system is designed such as the Hamiltonian is the same as the quantum problem to solve, then the calculations over this Hamiltonian will be done by nature. Of course, in practice it is impossible to reproduce in the experiments exactly the same model Hamiltonian, so the task of building an analog quantum simulator is to make the Hamiltonian of the simulator as close as possible to the Hamiltonian to be simulated, such that we can believe we can get the physics of the simulated Hamiltonian from measurements performed on the analog quantum simulator.

Compared to a true quantum computer, an analog quantum simulator is usually easier to build. On the one hand, one needs to build a new analog simulator for each model; on the other hand, an analog simulator can be optimized specifically for the simulated model, without taking any compromises for the sake of being applied to other general models as for a quantum computer.

#### 1.1.3.3 Cold atoms for quantum simulations

In order to give the desired Hamiltonian, we need to have good control over the experimental system of the simulator. As we explained above, the Hamiltonian Eq. (1.8) of the ultracold atomic gas is remarkably controllable and the physical information of the atomic gas can be probed in various ways, thus ultracold atomic gases are a good candidates for quantum simulation[27, 102].

There are many achievements in this field, including for examples simulating the quantum phase transition between a Mott insulator and a superfluid by tuning the optical lattice depth [71], simulating the BEC-BCS crossover by the Feshbach resonance [103], simulating artificial gauge field by rotating the trapping potential or by utilizing the Berry phase in atom-laser interactions which leads to the quantum Hall effects in cold atoms [104], simulating one dimensional spin chains [105] and simulating localization effects in disordered or quasiperiodic systems [106–110].

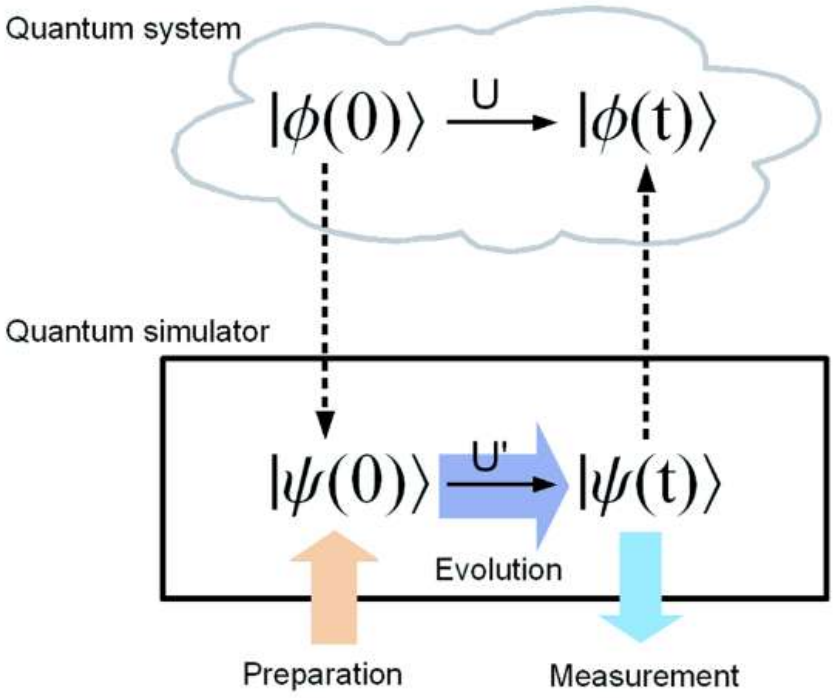


Figure 1.9: Schematic representation of a quantum system and a corresponding quantum simulator. The quantum state $|\phi(0)\rangle$ evolves to $|\phi(t)\rangle$ via the unitary transformation $U = exp(-i\hbar H_{sys}t)$. The quantum simulator evolves from the state $|\psi(0)\rangle$ to $|\psi(t)\rangle$ via $U' = exp(-i\hbar H_{sim}t)$. The simulator is designed such that there is a mapping between the simulator and the simulated system, in particular, the mappings $|\phi(t)\rangle \leftrightarrow |\psi(t)\rangle$,$|\phi(0)\rangle \leftrightarrow |\psi(0)\rangle$, and $U \leftrightarrow U'$. While the simulated system may not be controllable (or not experimentally accessible in some cases),the quantum simulator is. Namely, the initial state $|\psi(0)\rangle$ can be prepared, the unitary evolution $U'$ can be engineered, and the final state $|\psi(t)\rangle$ can be measured. The result of this measurement provides information about the simulated system. The colored arrows denote the controllable operations. The solid black arrows describe the time evolution of the system and the simulator. The dashed arrows indicate the correspondence between the quantum states of the simulator and the simulated system. This figure is from Ref. [23]

## 1.2 Localization

In this thesis we will study the quantum simulation of 2D quasicrystals by cold atoms, including the localization properties. In this section, we give a brief review of the basic idea of localization, disorder and quasicrystals.

### 1.2.1 Bloch waves in periodic potentials

For comparison to a disordered case, we first review the Bloch theorem for single particle eigenstates in a periodic potential. For simplicity, we take a one dimensional system. The Hamiltonian is

$$H = \frac{p^2}{2m} + V(x) \tag{1.11}$$

where the potential is a periodic function,

$$V(x) = V(x + a), \tag{1.12}$$

where $a$ is the lattice constant.

The system has discrete translational symmetry for all translations of an integer times $a$. According to the Wigner's theorem, this translation symmetry should be mathematically represented as a linear, unitary operator $T$. The operator of translation of distance $a$ is

$$T_a\psi(x) = \psi(x - a). \tag{1.13}$$

The momentum operator $\hat{p}$ is by definition the generator of spatial translation (multiplied by $\hbar$), so we can also write the operator $T_a$ in terms of $\hat{p}$ as

$$T_a = e^{-ia\hat{p}/\hbar}. \tag{1.14}$$

The Hamiltonian commutes with $T_a$ thanks to the periodicity of potential $V(x)$. As a consequence, we can search the common eigenstates of $H$ and $T_a$. Since the translation operations commute with each other, all the translation operators $T$ form an Abelian group. Abelian groups only have one dimensional irreducible representations. The eigenstates are such that

$$T_a\psi(x) = \lambda\psi(x). \tag{1.15}$$

The eigenvalue $\lambda$ should be a pure phase $e^{-i\theta(a)}$ since $T_a$ is unitary. We expect the phase $\theta(a)$ to be linear with $a$ due to the commutation of translations. So we write the phase as $\theta(a) = ka$, and the eigenstate $\psi(x)$ obeys

$$e^{-ika}\psi(x) = T_a\psi(x) = \psi(x - a). \tag{1.16}$$

Defining $u(x) = e^{-ikx}\psi(x)$, we get

$$u(x - a) = e^{-ik(x-a)}\psi(x - a) = e^{-ikx}e^{ika}\psi(x - a) = e^{-ikx}\psi(x) = u(x), \tag{1.17}$$

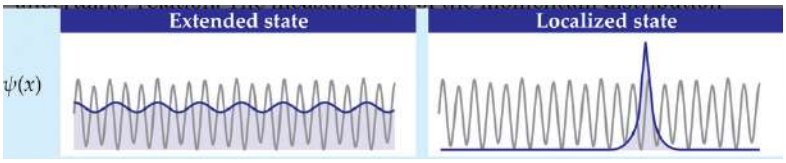


Figure 1.10: Left: an extended state. Right: a localized state. The blue curves represent the typical profiles of the wavefunctions in the two cases. This figure is from Ref. [111]

so $u(x)$ is a periodic function with period $a$.

In summary, the eigenstates of the periodic Hamiltonian can be written as

$$\psi(x) = e^{ikx}u(x), \tag{1.18}$$

where $u(x)$ is a periodic function $u(x+a) = u(x)$.

This result can be easily extended to multi-dimensional systems, noting that the translations in different directions all commute with each other. The eigenstates are just plane waves multiplied by a periodic function with the same period as the periodic potential. This gives a typical example of extended states, whose wavefunctions run across the system. See Fig. 1.10 (left) for a typical wavefunction profile of an extended state.

We can see from Eq. 1.18 that a difference of $k = 2\pi/a$ means a phase difference $e^{i2\pi x/a}$ of the Bloch wavefunction. This phase factor is itself a periodic function with period $a$, so it can be absorbed into the periodic function $u(x)$. As a result, the $k$ is defined with modulus $2\pi/a$. We can choose the range of $k$ as from $-\pi/a$ to $\pi/a$, and this range is called the Brillouin zone. For each $k$ in the Brillouin zone, there could be different $u(x)$ corresponding to wavefunction with different energies. The energies of Bloch states are grouped into energy bands, separated by energy gaps between them.

The electrons in perfect crystals obey the Bloch theorem if we neglect the interactions between the electrons and between the electrons and the phonons. Their eigenstates are given by Bloch waves and the eigenenergies are Bloch bands separated by energy gaps. Each eigenstate of an electron has a crystal momentum $\hbar k$, where $k$ lies in the Brillouin zone. The Fermi level is decided by the electron numbers in the solid. If the Fermi level is inside an energy band, a driving force can lead to an increase of the crystal momentum of all the electrons in this band and thus induce current. If the Fermi level is in an energy gap, then the energy bands are fully occupied. A driving force may still increase the crystal momentum but the electron at one end of the Brillouin zone will reenter the Brillouin zone from the other end, so the net change of the total current of the electrons is zero. As a result, we have an insulator. This kind of insulator is usually called the band insulator.

If we turn on the interaction, for weak repulsive interaction between electrons, Fermi liquid theory tells us that the above picture of free electrons still holds, as long as we replace the bare electrons by quasiparticles which are dressed

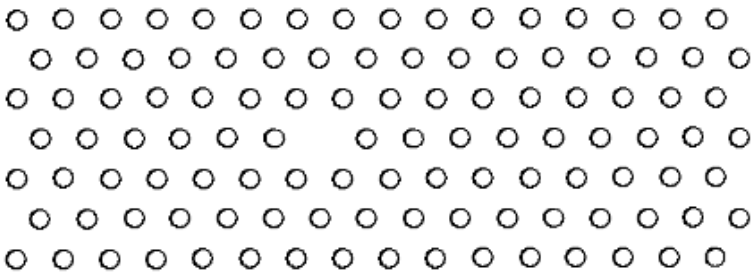

Figure 1.11: A portion of a monatomic Bravais lattice containg a vacancy. This figure is from Ref. [112]

by interactions. However, strong repulsive interactions may induce a metal-insulator phase transition when the electrons are at half filling of the band. The picture is that the electron movements are blocked due to the Pauli principle and interactions. This kind of insulator is named as Mott insulator.

### 1.2.2 Localization in disordered systems

A disordered system is characterized by a potential $V(\mathbf{r})$ containing randomness. Historically, localization transitions in disordered systems was first discussed in the context of metal-insulator transitions in condensed matter physics. Apart from band insulator and Mott insulator mentioned above, another kind of insulator transition is possible due to the localization of electron wavefunctions [81] in disordered potential.

Disorder is ubiquitous. Take a crystal for example, there could be vacancies and interstitials as the absence of ions or presence of extra ions, there could be dislocations where arrays of atoms are misaligned, there could be impurities which are different kinds of atoms present in the crystal. These crystal defects generally appear randomly in positions, thus distort the crystal from a perfect periodic lattice [112].

It is worth noting that the disorder is not something that unfortunately enter the system, but really intrinsically exist [112]. For instance, for the vacancy defects in crystals with typical energy cost $\Delta E$ as shown in Fig. 1.11, a nonzero density $n$ of defects is guaranteed by a nonzero temperature $T$. Although there is a cost in energy $\Delta E$, this can be compensated by the gain in entropy. In fact, the defects' density $n$ is given by the Boltzmann distribution $n \sim e^{-\Delta E/T}$.

Take into account the disorders in the crystal like impurities or defects, the potential is not any more a pure periodic potential but contains a certain degree of randomness. It has been shown that in the presence of strong enough disorders, single particle wavefunctions of electrons can be localized in space. See Fig. 1.10 (right) for a typical wavefunction profile of a localized state. It

covers a finite region of the space and at large distance the wavefunction only has an exponentially decaying tail. As a result, the electrons cannot move across the system and the crystal become an insulator. This metal-insulator transition due to disorder is usually called Anderson transition.

The Anderson localization transition depends strongly on dimension. This can be analysed by scaling theory [113]. The idea is to dynamically enlarge the system size and try to see whether a wavefunction in a small system tends to become more localized or more extended as the system size is being increased. One characterizes this by a dimensionless parameter $g$ [114, 115]: if $g$ is large, the particle tends to be extended; if $g$ is small, the particle tends to be localized. For a metal, $g$ represents the conductance. Dimensional analyses indicate that at the large $g$ limit where wavefunctions are extended, $g$ scales with the system size $L$ as a power law $g \sim L^{d-2}$ with $d$ the dimension of the system. On the other hand, at the small $g$ limit where wavefunctions are localized, $g$ scales with the system size $L$ exponentially as $g \sim e^{-\alpha L}$.

In order to analyze the behaviour of $g$ with respect to linear size of the system $L$, we define a scaling parameter $\beta = \frac{d \ln g}{d \ln L}$. In the small $g$ limit, $g \sim e^{-\alpha L}$ decreases as system size $L$ increases, so $\beta = \frac{d \ln g}{d \ln L}$ is negative. In the large $g$ limit, we have $\beta \sim d - 2$. A flow diagram of $\beta(g)$ is shown in Fig. 1.12, where the arrows indicate the flow direction when system sizes are increased.

In a one dimensional system with $d = 1$, the $\beta(g)$ is always negative. So $g$ decreases as the system size $L$ increases, and finally will enter the localized regime. Thus we conclude that all states are localized in one dimension with the presence of arbitrarily small disorder.

A similar situation is expected for dimension $d = 2$, though it is marginal here as the limiting value of $\beta$ at large $g$ tends to 0.

In three dimension with $d = 3$, the behaviour of $g$ is richer as $\beta(g)$ crosses 0 at a critical point $g_c$. If we start with a $\beta(g) > 0$, then the system will end in the extended regime in the infinite large $L$ limit. In contrast, if we start with a $\beta(g) < 0$, then the system will end in the localized regime in the infinite large $L$ limit. So there is a critical point of the transition between localized and extended phases.

In summary, in one dimension, all the single particle eigenstates will be localized for arbitrarily weak disorder. The same phenomenon is expected to hold for two dimensional systems as well. In three dimensions, a finite disorder is needed for the localization of single particle eigenstates. Thus there exists a critical disorder potential amplitude above which the states could be localized. In addition, for a given potential amplitude, localization also depends on the eigenenergies of the states. The energy which separates the localized states from extended states is called mobility edge.

Generally speaking, Anderson localization is a destructive coherence effect for waves propagating in a disorder medium. It is not restricted to the wavefunction in quantum mechanics and can be realized for classical waves as well [117]. In particular, Anderson localization can be observed for matter waves using cold atoms [20, 108, 110, 118, 119].

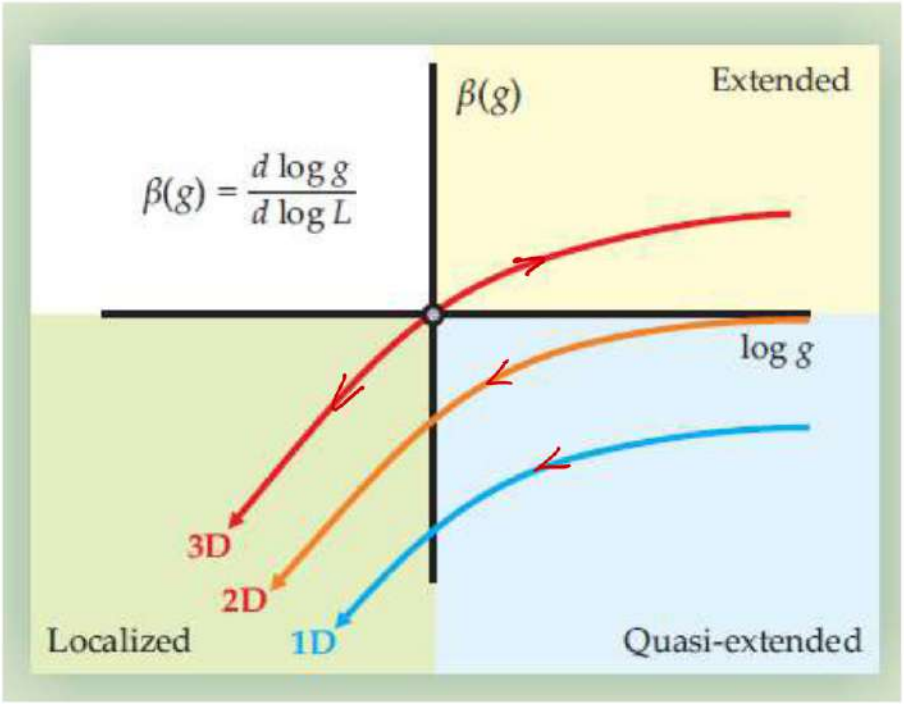


Figure 1.12: According to scaling theory, Anderson localization is a critical phenomenon, at least in three dimensions. The scaling function $\beta(g)$ describes how, or more precisely, with what exponent the average conductance $g$ grows with system size $L$. For a normal ohmic conductor in $d$ dimensions, the conductance varies as $L^{d-2}$; consequently, $\beta(g) \sim d-2$ for large $g$. Thus the beta function is positive for three dimensional conductors, zero for two-dimensional conductors, and negative in one dimension. In the localized regime, $g$ decays exponentially with sample size so that $\beta(g)$ is negative. In three dimensions, that leads to a critical point at which $\beta$ vanishes for some special value for $g$ associated with the mobility edge. Lower-dimension systems do not undergo a genuine phase transition because the conductance always decreases with system size. A small 2D conductor, for instance, will look like a metal in the quasi-extended regime, but all its states are eventually localized if the medium is large enough. The arrows indicate the renormalization flow directions as system size increases. This figure is from Ref. [116]

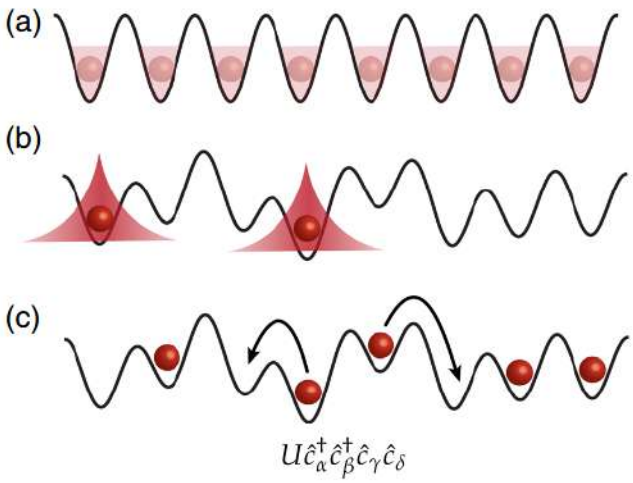


Figure 1.13: (a) In a clean crystal, eigenstates are Bloch waves, which extend throughout the sample. (b) The essence of Anderson localization of non-interacting particles is that for sufficiently strong disorder there is a vanishing probability for a particle to make a resonant transition from one site to another one spatially separated from it. This leads to eigenstates which are localized in some region of space, decaying exponentially away from it.(c) Adding interactions to an Anderson localized system. To first order, the effect of interaction is to induce hopping of pairs of particles between the single-particle localized orbitals. One may ask if the localized phase, with vanishing particle and thermal conductivities, is robust to this process. This figure is from Ref. [120]

Since the Anderson localization is a single particle localization, a natural question to ask is whether similar localization scenario will hold if the interaction is turned on, see Fig 1.13. As we have seen in the discussion of Mott transition and Anderson transition, either interactions or disorder can lead to localization. When both of them are present, the interplay between interaction and disorder is interesting and, to a great extent, open question. There is the currently still quite debatable subject of many body localization (MBL). The idea is that, for a many-body quantum system, due to the presence of disorder, the system is unable to be thermalized, or, at least, the thermalization process has a differnt form of scaling with time which is much slower than the case without disorder [120]. Interacting bosons in the presence of disorder may enter into a localized phase call Bose glass. The idea was introduced for experiments with liquid helium [121]. It is observed that on porous substrates the liquid helium may have a suppression of superfluidity. It suggests that interactions may cooperate with disorder and induce a localization phase. The Bose glass is a compressible, gapless phase and it is an insulating phase where superfluidity disappears. While the existence of a Bose glass phase was theoretically discussed in one dimension in 1988 [122] and in higher dimensions in 1989 [54], up to now a direct undisputed observation of a Bose glass in cold atoms experiments is still a challenge.

## 1.3 Quasicrystals

A quasicrystal is a structure with long range order but with no spatial periodicity. Since its experimental discovery in the 1980s [1], it has attracted tremendous attention due to fascinating properties. Quasicrystals can usually be obtained in the laboratory by rapid solidifying of alloys. It shows many novel properties including for examples exotic transport properties, intricate energy spectrum and phasonic degrees of freedoms [3, 4, 7–13, 123]. In particular, like disordered systems, quasiperiodic structures can host localized states [19, 38, 39, 49, 124, 125]. In this section, we give a concise review of quasicrystals and the localization phenomena in it.

### 1.3.1 Definition

A usual way to explore the structures of crystals are diffraction experiments. Figure 1.14 (left) shows the electron diffraction pattern of a normal crystal. It is composed of sharp peaks, reflecting the periodic order of the crystal. A normal crystal is a periodic structure which has translational and discrete rotational symmetries. The translational symmetry has a restriction over the possible types of rotational symmetry. Take a point $A$ in the Bravais lattice, which is on the rotation axis, and then take another point $B$ on the Bravais lattice, separated from $A$ by the shortest period $a$ of the lattice, as shown in Fig. 1.15. If the crystal has a $n$ fold rotational axis, then the points $A'$ and $B'$ obtained by rotations of angle $\phi = 2\pi/n$ should also be points in the Bravais lattice. The

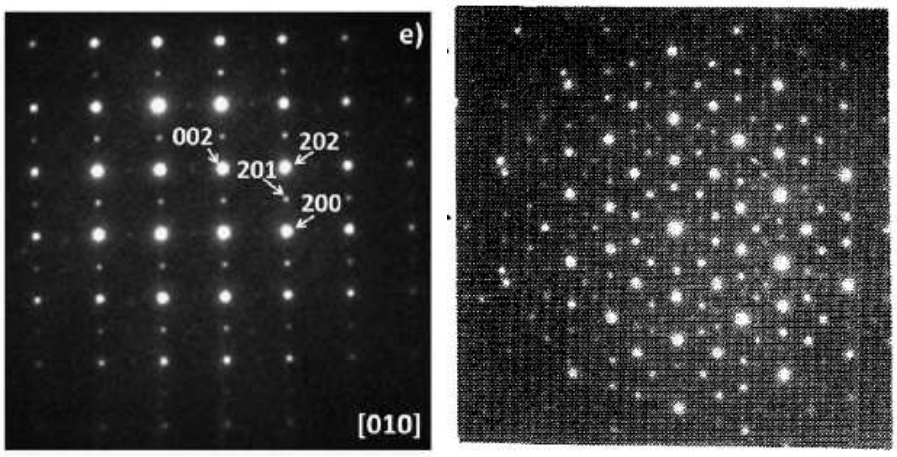


Figure 1.14: Left: Electron diffraction pattern of a crystal. This figure is from Ref. [126]. Right:Electron diffraction pattern of a quasicrystal alloy. This figure is from Ref. [1]

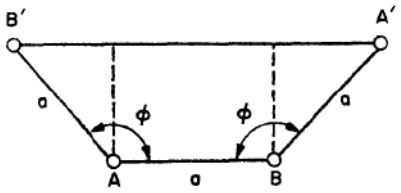


Figure 1.15: $A$ and $B$ are two points on the Bravais lattice. The rotation axis is perpendicular to the plane. This figure is from Ref. [1]

distance from $A'$ to $B'$ should be a integer times the smallest period $a$, as

$$a + 2a\sin(\phi - \pi/2) = pa, \tag{1.19}$$

with $p$ an integer. The only possible solutions for $n$ is $n = 1, 2, 3, 4, 6$. So translational symmetry of a normal crystal restricts the possible types of rotational symmetry to 1,2,3,4,6 folds.

In 1984, an electron diffraction image which does not fulfill this restriction was published [1], as shown in Fig. 1.14 (right). The rapidly cooled alloy which gave this diffraction pattern has a icosahedral point group symmetry, which is not a sub group of any of the 230 space groups for 3D crystals. It is actually a quasicrystal. In fact, it is only after some time that people started to commonly acknowledge this new structure of solids. There was a lot of debates over it as it has challenged common beliefs on the possible types of lattices that a crystal can possess. For example, Linus Pauling believed and persistently argued that it came from twinning of periodic crystals [127–133]. However, explaining

the experimental data on quasicrystals with the model of twinning of normal crystals could require very large unit cells composed of more than 10 thousand atoms [132, 134]. In the end, people has gradually realized the quasicrystals are true new order of solids, which is a paradigm shift in crystallography. On the one hand, the fact that quasicrystals' diffraction patterns are composed of sharp peaks means that quasicrystals are long range ordered structure. On the other hand, differing from traditional normal crystals, a quasicrystal has no translational symmetry, and it can have rotational symmetries which are forbidden for crystals, such as 5-fold, 7-fold, 8-fold etc.

Diffraction from periodic objects results in sharp spots, corresponding to the reciprocal lattice. One reason of the controversies over quasicrystals is that people simply took for granted the converse statement, sharp diffraction spots could only come from a periodic object, to be true [135]. The idea that sharp diffraction peaks can come from non-periodic sturctures can be more easily realized by considering a quasicrystal as the projection of a periodic lattice in a higher dimensional space to a lower dimensional space. This is usually called the cut-and-project method. For simplicity, let's illustrate this idea for a one-dimensional quasiperiodic chain projected from a two-dimensional lattice, see Fig. 1.16. Take a 2D lattice on the $xy$ plane, and take a $x'$ axis with slope $\frac{\sqrt{5}-1}{2}$. The $xy$ plane corresponds to the higher dimensional space and the $x'$ axis corresponds to the physical dimension where the quasicrystal lives. Draw the red strip parallel to $x'$ axis with a width to cover one unit cell in the 2D lattice, then project all the lattice points covered by the red strip onto the $x'$ axis. Thus we obtain a sequence of red long bar and short blue bar on the $x'$ axis, which is a one dimensional quasiperiodic structure with long range order. This sequence of long and short bars do not have translational symmetry, while it is not random either. Denoting the long red bar by $L$ and short blue bar by $S$, the sequence of $L$ and $S$ is just the Fibonacci chain. The Fibonacci chain can also be obtained from a substitution construction. If we start by $L$ and then substitute the sequence step by step with the rule: $L$ replaced by $LS$ and $S$ replaced by $L$, then we can get sequences $F_n$ as follows

$$
\begin{aligned}
F_1 =& L \\
F_2 =& LS \\
F_3 =& LSL \\
F_4 =& LSLLS \\
F_5 =& LSLLSLSL \\
F_6 =& LSLLSLSLLSLLS \\
& \cdots
\end{aligned}
$$

We can easily check that the sequence $F_n$ at step $n$ is the concatenation of the sequences of the previous two steps $F_n = F_{n-1}F_{n-2}$, just like Fibonacci numbers.

The idea of quasicrystals was historically first introduced mathematically as a tiling of a 2D plane, before the physical observation of quasicrystal materials

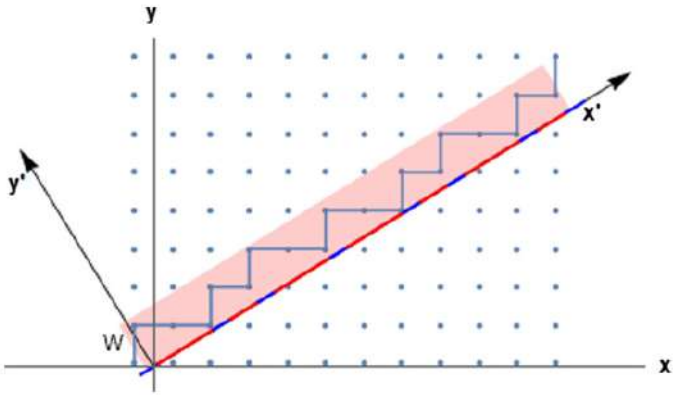


Figure 1.16: The cut-and-project method. Selected points(joined by a broken line) of a 2D square lattice are projected on to the $x'$ axis, giving the binary quasiperiodic sequence of red and blue tiles. The infinite selection strip $S$ is colored red. This figure is from Ref. [136].

in the laboratories. A tiling means a covering of a surface with some patterns of geometrical shapes, with no overlaps or gaps. Figure 1.17(left) shows a tiling of a 2D plane with two kinds of tiles, colored green and blue. It shows strong regularity as it has discrete translational symmetries. The tiling structure represents a normal periodic crystal. While it is common to have a periodic tiling of a 2D plane as in Fig. 1.17(left), there exists the aperiodic tilings, as in Fig. 1.17(right). It is still a covering of a 2D plane with no overlap or gap, though it has no translational symmetry. In particular, a kind of aperiodic tiling that is closely connected to quasicrystals is the so-called "Penrose tiling", which has no periodicity but has some reflection and rotational symmetry. An example of Penrose tiling is shown in Fig. 1.18 (left). Note that it is composed of the same two kinds of tiles as the periodic tiling shown in Fig. 1.17 (left), the only difference lies on the rules of arrangements of the tiles. It is a long range order structure with 5 fold rotational symmetry. A diffraction pattern of Penrose tiling is shown in Fig. 1.18 (right). It is composed of sharp peaks, with similarities in structure compared to the diffraction pattern shown in Fig. 1.14 (right).

### 1.3.2 Localization in quasicrystals

A quasicrystal is an intermediate situation between a periodic potential and a disordered potential, since quasicrystals have long range order but have no translational symmetry. We have seen that extended Bloch waves are hosted in periodic potentials while Anderson localization exists in disordered potentials. It is interesting to study what would be the localization physics in a quasicrystal potential, which has been studied a lot [19, 38, 39, 44, 49, 140–142].

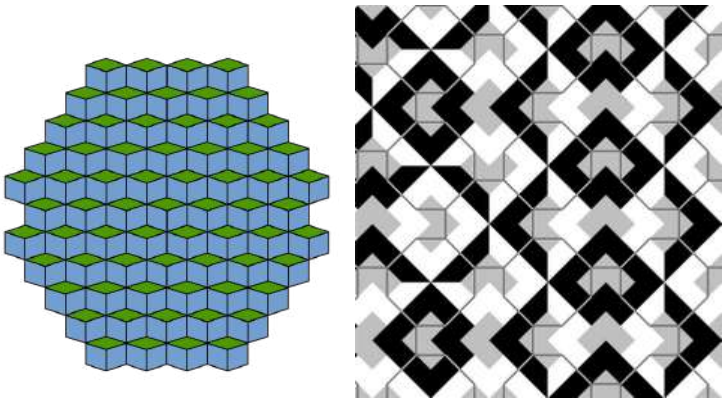

Figure 1.17: Left: a regular tiling of a two-dimensional plane with discrete translational symmetry. This figure is from Ref. [137]. Right: an aperiodic tiling of a two-dimensional plane with no translational symmetry. This figure is from Ref. [138].

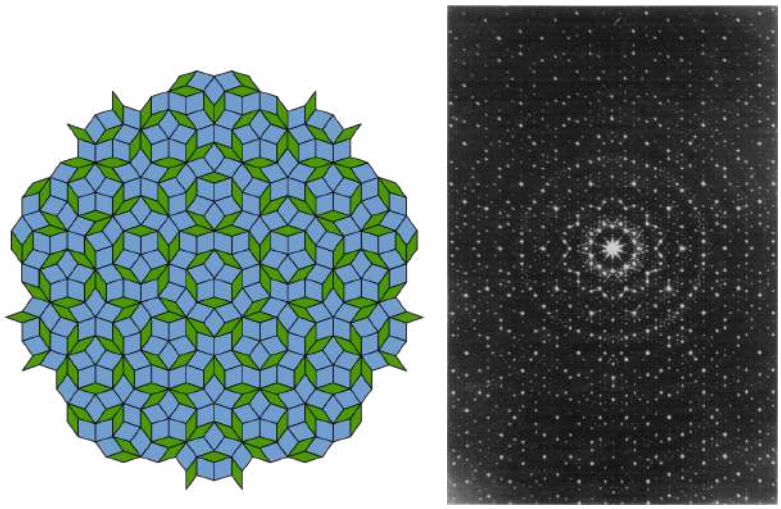

Figure 1.18: Left: a Penrose tiling, taken from Ref. [137]. Right: diffraction pattern for a Penrose tiling, taken from Ref. [139].

Now we turn to 1D for illustration. A quasiperiodic potential in one dimension can be obtained by superimposing periodic potentials with incommensurable periods. For example, a quasiperiodic bichromatic potential can be written as

$$V(x) = \frac{V_1}{2}\cos(2k_1 x) + \frac{V_2}{2}\cos(2k_2 x), \tag{1.20}$$

with $k_2/k_1 = \beta$ an irrational number. If the first potential amplitude $V_1$ is much larger than the second potential amplitude $V_2$ and the recoil energies $E_1 = \hbar^2 k_1^2/2m$, $E_2 = \hbar^2 k_2^2/2m$ of the two, i.e. $V_1 \gg V_2, E_1, E_2$, then the Hamiltonian with the quasiperiodic potential Eq. 1.20 can be discretized to be a tight binding model on a lattice, giving rise to the Aubry-André model [19], as

$$H = -J\sum_n (a_n^\dagger a_{n+1} + h.c.) - \lambda J \sum_n \cos(2\pi\beta n) a_n^\dagger a_n \tag{1.21}$$

It is a non-interacting lattice model with a constant hopping term and the modulating on-site energy showing quasiperiodic pattern.

It turns out that this model has a self duality between real space and momentum space [19]. Taking the Fourier transform of the operators as

$$b_k = \frac{1}{\sqrt{N}}\sum_n exp(2\pi i\beta k n) a_n, \tag{1.22}$$

the Hamiltonian can be rewritten as

$$H = -\frac{\lambda J}{2}\sum_k (b_k^\dagger b_{k+1} + h.c.) - 2J\sum_k \cos(2\pi\beta k) b_k^\dagger b_k. \tag{1.23}$$

We can see that the momentum space Hamiltonian has the same form as the real space one if we replace $\lambda$ by $4/\lambda$ (up to a total multiplication factor $\frac{\lambda}{2}$). Since we know a state localized in real space is extended in momentum space, and vice-versa, the self duality of Aubry-André model shows that a critical point of localization is given by $\lambda = 2$. For $\lambda < 2$, all states are extended; for $\lambda > 2$, all states are localized.

In contrast to disordered potentials, where all states are localized for arbitrary small disorder, the states in the 1D Aubry-André model can be extended or localized depending on the strength of the quasiperiodic potential. This is an example of where a quasicrystal is somehow less disordered.

# Chapter 2

# Quantum fluids of bosons

A theoretical study of quantum simulations of quasicrystals using cold bosons will be discussed in the following chapters, based on the theories of bosonic quantum liquids. The study of quantum liquids of bosons was initially driven by the observation of superfluidity in liquid helium [55, 56]. Theoretical models like the Gross-Pitaevskii equation and Bogoliubov mean field theory were developed to describe it. The early understandings of superfluidity were independent of Bose-Einstein condensation (BEC). However, it was realized later that superfluidity is closely connected to BEC. Interestingly, theses theories initially developed for liquid helium really became more realistic for the dilute Bose gas experimentally realized in the 1990s, where one can give a firmer microscopic foundation for those theories [99]. The ultracold atomic system also gave access to physics beyond what had been observed for liquid helium. For example, the combination of a dilute Bose gas and an optical lattice gave rise to strongly-interacting lattice systems of bosons, where a quantum phase transition between superfluid and Mott insulator was observed [71]. Besides analytical theories, numerical methods for quantum liquids of bosons were also developed with the advances of computer power. One of the most successful numerical methods is the path integral Monte Carlo method [143], which was later on improved with the worm algorithm [144, 145]. In this chapter, I will give a brief review of the theory of quantum fluids of bosons, in particular those that will be used in the following chapters of this thesis, and the path integral Monte Carlo numerical method, with emphasis on the key logical and physical ideas.

## 2.1 BEC and superfluid in 3D

### 2.1.1 BEC of non-interacting bosons

The BEC of non-interacting bosons was initially predicted by Einstein. After Bose proposed the indistinguishable statistics over the photons, Einstein extended this new statistics to the massive particles, where the total particle number is fixed and a condensation can be expected. It gives a typical example

of a phase transition for a non-interacting system in 3D and above. Below the critical temperature, there is a macroscopic occupation of bosons in a single state. Intuitively, one can understand this fact from the $\sqrt{n+1}$ and $\sqrt{n}$ factors in the boson creation and annilation operators, which illustrates that bosons like to stay in the same state. Mathematically, BEC is a consequence of the convergence of the total particle number that can be accommodated by all the excited states.

Non-interacting bosons obey the Bose-Einstein distribution

$$n_s = \frac{1}{e^{(E_s-\mu)/k_{\mathrm{B}}T} - 1}, \tag{2.1}$$

which gives the occupation number $n_s$ for each single particle state $s$. The single particle state energy $E_s$ is bounded below by the energy of the ground state $E_g$. In free space, the ground state energy can be chosen to be $E_g = 0$, and this will be the case that we consider.

At high temperature, the chemical potential $\mu$ is a large negative number, so $e^{(E_s-\mu)/k_{\mathrm{B}}T} \gg 1$. The Bose-Einstein distribution is approximately

$$n_s = e^{(\mu-E_s)/k_{\mathrm{B}}T}, \tag{2.2}$$

which is just the Boltzmann distribution for distinguishable particles.

If we decrease the temperature $T$ while keeping the total particle number $N$ in the system constant, the chemical potential $\mu$ will increase. However, the increase of $\mu$ is bounded by the ground state energy $E_g = 0$, otherwise the Bose-Einstein distribution $n_s$ for ground state would be meaningless. The fact that $\mu$ is always smaller than 0 gives an upper bound of the total particle number in the excited states

$$N_{exc} = \sum_{excited} \frac{1}{e^{(E_s-\mu)/k_{\mathrm{B}}T} - 1} < N_{exc}^{max} = \sum_{excited} \frac{1}{e^{E_s/k_{\mathrm{B}}T} - 1} \tag{2.3}$$

This upper bound $N_{exc}^{max}$ can be rewritten as an integral using the density of states

$$N_{exc}^{max} = \int_0^\infty d\epsilon \rho(\epsilon) \frac{1}{e^{\epsilon/k_{\mathrm{B}}T} - 1} \tag{2.4}$$

where $\rho(\epsilon)$ represents the density of states for energy $\epsilon$.

This integral is convergent in the upper limit due to the exponential factor. At low limit, the convergence of the integral depends on the form of the density of states $\rho(\epsilon)$. In 3D homogeneous space, $\rho(\epsilon) \propto \epsilon^{1/2}$, and the integrand scales as $\epsilon^{-\frac{1}{2}}$ for small $\epsilon$, so the integral converges at the lower limit. As a result, the total number of particles in the excited states are upper bounded by a finite number. As the chemical potential $\mu$ approaches 0, the number of particles in excited states reaches this upper bound, while the number of particle in the ground state diverge. So when the total particle number $N$ is larger than the upper limit of particle number in the excited states $N_{exc}^{max}$, all the remaining $N - N_{exc}^{max}$ particles will go to the ground state. Thus we have a macroscopic occupation of a single quantum state.

## 2.1.2 BEC of interacting bosons

### 2.1.2.1 Penrose and Onsager definition

For interacting bosons, the single particle states are not relevant anymore and the above definition of BEC loses its sense. However, some features of BEC of non-interacting bosons can be used to extend the definition of BEC into the interacting case [99]. Here I first give a brief review of the definition of BEC in interacting systems following the idea of Penrose and Onsager.

A many-body system of $N$ bosons can be described in quantum mechanics in the most general way as a $N$ body density matrix $\rho_N(r_1, r_2, ..., r_N; r'_1, r'_2, ..., r'_N)$.

We can define the single particle density matrix by taking the partial trace of $N-1$ coordinates as

$$\rho(r, r') \equiv N \int dr_2 ... dr_N \rho_N(r, r_2, ..., r_N; r', r_2, ..., r_N). \tag{2.5}$$

Equivalently, it can be obtained from the Bose field operator $\hat{\psi}(r)$ as

$$\rho(r, r') = \langle \hat{\psi}^\dagger(r) \hat{\psi}(r') \rangle. \tag{2.6}$$

As the $N$ body density matrix is Hermitian, it follows directly from the definition that the single particle density matrix is also Hermitian

$$\rho(r, r') = \rho^*(r', r). \tag{2.7}$$

As a result, this single particle density matrix $\rho$ can be diagonalized with all eigenvalues being real numbers, as

$$\rho(r, r') = \sum_i N_i \chi_i^*(r) \chi_i(r'). \tag{2.8}$$

The BEC for interacting systems can be defined as the case when one of the eigenvalues of $\rho(r, r')$, say $N_0$, is of order $N$. The corresponding eigenfunction $\chi_0(r)$, can be called the wavefunction of the condensate. Note that $\chi_0(r)$ is not necessarily connected with any eigenfunction of the single particle Hamiltonian. However, in many aspects, it just behaves as a single particle wavefunction. In particular, it is clear from Eq. 2.8 that $\chi_0(r)$ is defined up to a global phase factor $e^{i\phi}$ with no physical significance. This property is sometimes called $U(1)$ gauge symmetry, and it is connected with the symmetry of the Hamiltonian that it conserves the particle number. It is obvious that this definition of BEC for interacting bosons is consistent with the previous definition of BEC for non-interacting bosons.

An order parameter characterizing the BEC phase can be defined as

$$\Psi(r) = \sqrt{N_0} \chi_0(r) \tag{2.9}$$

which contains both the information of the condensate particle number and condensate wavefunction. We can write out explicitely the phase of the complex variable $\Psi(r)$ as

$$\Psi(r) = |\Psi(r)| e^{i\theta(r)}. \tag{2.10}$$

Then we can write the density of the condensate as

$$\rho_c(r) = N_0|\chi_0(r)|^2 = |\Psi(r)|^2, \tag{2.11}$$

and the current carried directly by the condensate particles as

$$j_c(r) = N_0\left(-\frac{i\hbar}{2m}\chi_0^*(r)\nabla\chi_0(r) + c.c.\right) = N_0|\chi_0(r)|^2\frac{\hbar}{m}\nabla\theta(r). \tag{2.12}$$

The ratio $j_c(r)/\rho_c(r)$, which has a dimension of velocity, can be defined as the superfluid velocity

$$v_s(r) = \frac{\hbar}{m}\nabla\theta(r). \tag{2.13}$$

We can see from this expression that the circulation of this velocity over a closed contour is always zero if the order parameter is nowhere vanishing. Otherwise if the order parameter vanishes at some points the circulation of superfluid velocity is quantized to be $\frac{2\pi n\hbar}{m}$ with $n$ an integer because the phase $\theta(r)$ is defined only modulo $2\pi$.

#### 2.1.2.2 Off-diagonal long-range order

BEC in interacting systems can also be characterized by the behaviour of the single particle density matrix $\rho(r, r')$ in the limit $|r-r'| \to \infty$. In a translational invariant homogeneous system, the single particle density matrix $\rho(r, r')$ only depends on the relative difference between the two coordinates as $\rho(r, r') = \rho(r - r')$. Consequently, it is diagonalized in momentum representation. The diagonal elements $n(k) = \langle k|\,\rho\,|k\rangle$ are just the Fourier transform of $\rho(r - r')$. A BEC implies that the momentum distribution $n(k)$ has a sharp peak at $k = 0$, as the condensate in a homogeneous system should have zero momentum. The large distance limit of the single particle density matrix $\lim_{|r-r'|\to\infty}\rho(r, r')$ is a non-zero constant given by the sharp peak of $n(k)$, while the small values of $n(k)$ for nonzero $k$ will give zero contributions due to the rapid oscillations at large distance. This nonzero large distance limit of single particle density matrix is called the off-diagonal long-range order in the BEC system.

### 2.1.3 Gross-Pitaevskii equation and Bogoliubov spectrum

The Gross-Pitaevskii equation gives a description of a BEC for interacting bosons by a non-linear differential equation of a complex field. For liquid helium, where the condensate fraction $N_0/N$ is small, the Gross-Pitaevskii equation serves as a phenomenological theory of the superfluidity, as the Ginzburg Landau theory for superconductivity. For dilute Bose gas, where we have a large condensate fraction, we can derive the Gross-Pitaevskii equation from a microscopic perspective through the variational principle.

The variation ansatz is a mean field wavefunction of the Hartree form, where all particles take the same single particle wavefunction, and the many body wavefunction is just the product of all of them

$$|\psi\rangle = |\phi(1)\rangle \otimes |\phi(2)\rangle \otimes \cdots \otimes |\phi(N)\rangle \tag{2.14}$$

The Hamiltonian for a dilute gas consists of the kinetic terms, the single particle potential, and the two-body interactions

$$H = \sum_{i=1}^{N} \left( \frac{p_i^2}{2m} + V(r) \right) + \frac{1}{2} \sum_i \sum_{j \neq i} V(r_i - r_j), \tag{2.15}$$

where we take a contact interaction potential $V(r_i - r_j) = g\delta(r_i - r_j)$.

The variation principle amounts to minimize $\langle\psi| H |\psi\rangle - \mu \langle\psi|\psi\rangle$, where $\mu$ is the Lagrange multiplier associated with the conservation of the norm of the wave function.

The functional differentiation $\delta(\langle\psi| H |\psi\rangle - \mu \langle\psi|\psi\rangle)$ leads to equation

$$-\frac{\hbar^2}{2m}\nabla^2\phi(r) + V(r)\phi(r) + (N-1)g|\phi(r)|^2\phi(r) = \mu\phi(r). \tag{2.16}$$

In addition we can replace $N - 1$ by $N$ as $N \gg 1$. This is the Gross-Pitaevskii equation. By taking the derivative of the energy with respect to particle number $N$, we can show that the Lagrange multiplier $\mu$ is just the chemical potential of the system.

The variation ansatz means all bosons are in the same state, which is just the condensate. The Gross-Pitaevskii equation gives a mean field equation for the condensate wavefunction $\phi(r)$.

The assumption that all bosons are in the condensate is not really true with interactions turned on. The condensate fraction $N_0/N$ is smaller than 1 for interacting bosons at zero temperature. This is called the quantum depletion. The interaction kicks some particles out of the condensate. We can take into account this by allowing fluctuations of the complex field $\phi(r)$. The dynamics of these fluctuations give the dispersion of the elementary excitations

$$\hbar\omega_k = \sqrt{\frac{\hbar^2k^2}{2m}\left(\frac{\hbar^2k^2}{2m} + 2gn\right)}, \tag{2.17}$$

where $n$ is the particle number density. This formula can be obtained by linearizing the Gross-Pitaevskii equation for small perturbation around the mean field solution. This dispersion is called the Bogoliubov spectrum. At low energy, it gives a linear dispersion

$$\omega_k = ck, \tag{2.18}$$

which is just the sound mode. The sound velocity is $c = \sqrt{\frac{gn}{m}}$. In the high energy limit of the Bogoliubov spectrum, we recover the free particle dispersion.

## 2.1.4 Superfluid

### 2.1.4.1 Landau criterion

A superfluid is a state of matter that can move with no viscosity. Lev Landau gave an interpretation of this as the impossibility of exciting any excitations in

the superfluid. Suppose an impurity is moving in a superfluid. In order to have viscosity between the impurity and the superfluid, the moving impurity must be able to excite some elementary excitations in the superfluid, thus transfer its momentum to the elementary excitations and slow down, while the superfluid will have a nonzero momentum, i.e. carried along by the moving impurity. Otherwise, the impurity will have nothing to scatter and will move through the superfluid without losing any momentum or energy.

During the scattering processes of the impurity and the elementary excitations, the total momentum and energy are conserved. The scattering of elementary excitations is only possible if the velocity $v$ of the moving impurity is larger than a critical value $(\omega/k)_{min}$, i.e. the minimum of $\omega/k$ for the dispersion spectrum of elementary excitations in the superfluid. For the Bogoliubov spectrum we discussed above, this critical velocity is the sound velocity $c = \sqrt{\frac{gn}{m}}$, so we conclude that a BEC with Bogoliubov excitation spectrum at $T = 0$ is superfluid. In contrast, for non-interacting BEC, the excitation dispersion is the usual quadratic dispersion relation of free particles, and the critical velocity is zero. So a non-interacting BEC is not superfluid.

#### 2.1.4.2 Two fluids model of superfluid

Generally, the moving impurity may cause the fluid to move with it, but the momentum of the moving fluid does not equal the velocity times the whole mass of the fluid. This can be simply described by a two fluid model. The idea is that the quantum liquid of bosons is a mixture of two liquids, one of which is superfluid and the other a normal fluid. The two fluids move with different velocities. While the superfluid part cannot be driven by the moving impurity, the normal fluid part has viscosity just as a normal classical fluid. Note that this two fluid model is just a theoretical description and in reality there is no such separation of the quantum liquid.

The superfluid part and normal fluid part have their densities $\rho_s$ and $\rho_n$, and velocities $v_s$ and $v_n$. The total density of the fluid is the sum of the two densities

$$\rho = \rho_s + \rho_n, \tag{2.19}$$

and the total density current $j$ of the moving fluid is the sum of the currents

$$j = \rho_s v_s + \rho_n v_n. \tag{2.20}$$

As discussed before, the superfluid velocity is related to the condensate wavefunction as

$$v_s(r) = \frac{\hbar}{m}\nabla\theta(r), \tag{2.21}$$

with $\theta(r)$ the phase of the condensate wavefunction.

Suppose we put the quantum liquid in a ring confined by two circular walls with almost the same radius $r$. If we rotate the ring with an angular velocity $\Omega$, then the normal fluid part will rotate with the walls with the same angular velocity $\Omega$. However, the circulation of superfluid velocity is quantized to be

$\frac{2\pi n\hbar}{m}$ with $n$ an integer, so the superfluid velocity cannot be arbitrarily small unless zero. For small enough angular velocity $\Omega$, the superfluid velocity can only stay to be zero, which characterize the superfluid.

From the reference frame of the rotating confining ring, the normal fluid is at rest, while the superfluid part is rotating with angular velocity $-\Omega$. If the fluid is only a normal fluid, then the whole fluid would move with the confining ring, and in the reference frame of the rotating ring, the whole fluid would be at rest. The fact that the fluid is not all a classical normal fluid but has a nonzero superfluid density means there is an increase in the free energy $\Delta F$.

The change of reference frame to the rotating ring gives two changes to the Hamiltonian in the rotating frame of reference. Firstly there is an additional centrifugal term which shifts all energy level by $\frac{1}{2}I_{class}\Omega^2$, with $I_{class}$ the moment of inertia of the fluid if there is no superfluid part. Secondly the rotating frame changes the Hamiltonian in a way similar to introducing a magnetic field with vector potential $A(r) = m\Omega r$ in the angular direction. Thus momentum $p$ in the Hamiltonian is replaced by $p - A(r)$. This modification of the Hamiltonian can actually be absorbed into the boundary condition of the wavefunction while returning to the original form of the Hamiltonian. The new boundary condition enforces a phase difference $\Theta$ when the geometrical angle $\phi$ is turned by $2\pi$

$$\psi(\phi + 2\pi) = e^{-i\Theta}\psi(\phi), \tag{2.22}$$

with phase $\Theta = 2\pi\frac{\Omega}{\Omega_c}$ and $\Omega_c = \frac{\hbar}{mr^2}$.

Thus the increase of the free energy due to the nonzero superfluid density $\rho_s$ is related to the twisted boundary condition of the wavefunction. A careful calculation gives the relation

$$\frac{\Delta F(\Theta)}{V} = \frac{\hbar^2\Theta^2}{2mL^2}\rho_s \tag{2.23}$$

where $V$ is the system volume and $L$ is the circular length $2\pi r$.

In practice, this relation can be taken as a definition of the superfluid density. Of course, it is not necessary to always use the annular geometry. The twisted boundary condition in annular geometry is equivalent to an additional phase along one direction in a cubic box as

$$\psi(x + L, y, z) = e^{-i\Theta}\psi(x, y, z), \tag{2.24}$$
$$\psi(x, y + L, z) = \psi(x, y, z), \tag{2.25}$$
$$\psi(x, y, z + L) = \psi(x, y, z). \tag{2.26}$$

## 2.2 Superfluid in 2D and BKT phase transition

### 2.2.1 Absence of long range order

It follows from the Peierls instability [146], or more generally the Mermin-Wagner-Hohenberg theorem [147, 148], that a long range order does not exist in

2D for any non-zero temperature. In fact, there is no BEC for a homogeneous, infinite 2D Bose gas. For interacting bosons at low temperature, we use a classical field $\psi(r)$ to describe it. Finite temperature leads to fluctuations of the field. Its modulus fluctuation corresponds to the fluctuation of the density of bosons. The density fluctuations are suppressed by the interaction and can be neglected compared to the phase fluctuation.

There are two kinds of excitations that contribute to the phase fluctuation. The first kind is the phonons, which give smooth fluctuations of the phase with space. There is no singularity of the phase from the phonon modes. The second kind of excitation are vortices, where the density, or equivalently the amplitude of the field $\psi(x)$, vanishes, and there is a singularity of the phase. The phase can change by multiples of $2\pi$ around the singular point of the vortex. At low temperature, the vortices only appear in pairs with opposite winding direction of the phases and thus have negligible distortion of the phase at large distance. Then the phase fluctuations are given only by the phonon modes.

As discussed above, the superfluid density $n_s$ is related to the increase of energy with a twist phase on the boundary condition. So the energy of fluctuating phase can be written as

$$E \approx \frac{\hbar^2}{2m} n_s \int (\nabla\theta)^2 d^2r \tag{2.27}$$

with $\theta$ the phase of the classical field $\psi(r)$.

The phase fluctuation can be decoupled into Fourier modes where each mode has an average fluctuation proportional to the temperature $T$. With density fluctuations neglected, the correlation function $G(r)$ can be related to the phase fluctuation as

$$G(r) =< \psi(r)\psi^*(0) > \approx n < e^{i(\theta(r)-\theta(0))} > \tag{2.28}$$

With all these ingredients, a calculation of the correlation function $G(r)$ shows that it has an algebraical decay in 2D as

$$G(r) \propto r^{-\eta}. \tag{2.29}$$

The exponent $\eta$ is related to the superfluid density $n_s$ as $\eta = \frac{1}{n_s \lambda_T^2}$, where $\lambda_T$ is the thermal de Broglie wavelength. At large distance, the correlation $g(r)$ tends to zero, in contrast to the 3D case where it tends to a constant. We see that there is no off-diagonal long-range order in a 2D bose gas.

### 2.2.2 BKT phase transition

The energy of the fluctuating phase as in Eq. 2.27 is the same as in a 2D XY model. The XY model consists of vectors $\mathbf{S}$ on a lattice, where each vector $\mathbf{S_i}$ can point in a certain direction $\theta_i$ in a 2D plane. A 2D XY model is a XY model on a two dimensional lattice. The energy is given by the coupling of the vectors as

$$E = -J \sum_{<i,j>} \mathbf{S_i} \cdot \mathbf{S_j} = -J \sum_{<i,j>} \cos(\theta_i - \theta_j). \tag{2.30}$$

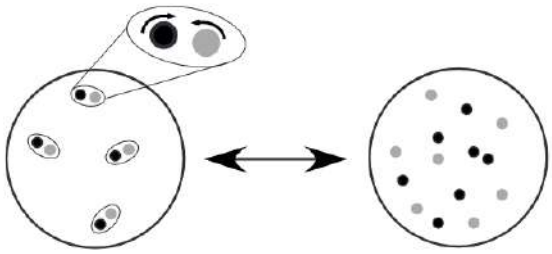

Figure 2.1: Microscopic mechanism at the superfluid transition in the uniform 2D Bose gas. Below the transition temperature, vortices exist only in the form of bound pairs formed by two vortices with opposite circulation. Above the transition temperature, free vortices proliferate, causing an exponential decay of the one-body correlation function $G(r)$. This figure is from Ref. [26]

At low energy, the slow variation of the angles $\theta$ gives an energy proportional to $\int(\nabla\theta)^2 d^2r$ in the continuous limit. This is the same form as the energy of a fluctuation phase in the superfluid in Eq. 2.27.

The 2D XY model has a phase transition induced by the vortices, which is called the BKT phase transition [149–151]. Similarly, the Bose gas also has a phase transition between superfluid and normal fluid in 2D even though a true condensate does not exist, and this transition is of the same universality class as the BKT transition in the 2D XY model. As discussed above, at low temperature, the correlation function has an algebraic decay induced by the phonons. Each vortex is bound with an anti-vortex, and the vortex/anti-vortex pair causes negligible deformation of the correlation function $g(r)$. At high temperature, individual vortices may appear. The vortices are topological defects where the phase changes by integer times $2\pi$ around it. Thus an individual vortex stongly suppresses the phase correlation and this leads to an exponential decay of the correlation function, see Fig 2.1. The Bose gas at high temperature is then in the normal fluid phase.

At the critical point, the superfluid density $n_s$ undergoes a jump from $4/\lambda_T^2$ to 0. This value of the superfluid density jump can be extracted from a thermodynamic argument. For a single vortex at the center of a disk, the velocity field is $v(r) = \frac{\hbar}{Mr}$, with $r$ the distance to the vortex center. The density at the vortex center is zero, and the size of the vortex is approximately the healing length $\xi$, a length scale set by the interactions strength over which the density recovers to the uniform value. The energy of a single vortex in a disk of radius $R$ can be approximated as

$$E = \pi M n_s \int v(r)^2 r dr = \frac{\pi\hbar^2 n_s}{M} \ln R/\xi. \tag{2.31}$$

On the other hand, the entropy of putting a vortex with size $\pi\xi^2$ in a radius

with area $\pi R^2$ is $S = k_B \ln \frac{R^2}{\xi^2}$. So the free energy $F = E - TS$ is

$$F/(k_B T) = \frac{1}{2}(n_s \lambda_T^2 - 4) \ln R/\xi. \tag{2.32}$$

For $n_s \lambda_T^2 > 4$, the free energy difference for creating a single vortex is positive and large in a large system, so the single vortex is thermodynamically unfavorable. For $n_s \lambda_T^2 < 4$, this free energy difference is large and negative, and it is favoured to have single vortices proliferate in the system. So we have the relation $n_s \lambda_T^2 = 4$ at the critical point.

### 2.2.3 Equation of state in the critical region

The thermodynamic argument above provides information about the superfluid density $n_s \lambda_T^2 = 4$ at the critical point. However, this does not inform us about the total particle number and chemical potential at the critical point. In this part, we review some results of the equation of state in the critical region obtained by a combination of analytical arguments and numerical calculations [152, 153].

At the critical point, the total particle number density and critical chemical potential are given by

$$n_c = \frac{mT}{2\pi\hbar^2} \ln\left(\frac{\xi\hbar^2}{mU}\right) \tag{2.33}$$

$$\mu_c = \frac{mTU}{\pi\hbar^2} \ln\left(\frac{\xi_\mu\hbar^2}{mU}\right) \tag{2.34}$$

where $U$ is the interaction strength and $T$ is the temperature. The $\xi$ and $\xi_\mu$ are two constants. Their values are given by Monte Carlo calculations for a classical $|\phi|^4$ model as $\xi = 380 \pm 3, \xi_\mu = 13.2 \pm 0.4$.

Next we give the equation of state and superfluid density around the critical point. The distance to the critical point is characterized by a dimensionless variable $X$ defined as

$$X = (\mu - \mu_c)/mTU. \tag{2.35}$$

Then the equation of state and superfluid density around the critical point are given by the universal thermodynamic relations

$$n - n_c = mT\lambda(X) \tag{2.36}$$

$$n_s = \frac{2mT}{\pi} f(X) \tag{2.37}$$

where $\lambda(X)$ and $f(X)$ are two dimensionless functions. The equation of state and superfluid density are fully characterized by these two dimensionless functions. The function $\lambda(X)$ can be further expressed in terms of another function $\theta(X)$ as

$$\lambda(X) = [\theta(X) - \theta_0 + X]/2 \tag{2.38}$$

TABLE I. Final results (after taking care of finite-size and finite-$U$ corrections) for the scaling functions $\theta(X)$, $g(X)$, and $f(X)$.

| $X$ | $\theta(X)$ | $g(X)$ | $f(X)$ |
|---|---|---|---|
| −4.0056 | 2.8363(3) | 0.2657(3) | |
| −3.0056 | 1.9603(5) | 0.3094(4) | |
| −2.0056 | 1.1472(6) | 0.3866(6) | |
| −1.5056 | 0.791(1) | 0.4561(8) | |
| −1.0056 | 0.514(1) | 0.581(1) | |
| −0.7556 | 0.434(3) | 0.688(3) | |
| −0.5056 | 0.442(3) | 0.869(2) | |
| −0.2556 | 0.630(4) | 1.214(4) | |
| −0.1056 | 0.885(9) | 1.560(7) | |
| −0.0556 | 0.973(9) | 1.680(7) | |
| −0.0156 | 1.041(9) | 1.774(8) | |
| −0.0056 | 1.061(4) | 1.800(3) | |
| 0.0044 | 1.075(5) | 1.821(4) | 1.077(5) |
| 0.0444 | 1.137(5) | 1.908(4) | 1.274(4) |
| 0.0944 | 1.208(5) | 2.013(4) | 1.433(5) |
| 0.2444 | 1.415(6) | 2.319(6) | 1.823(6) |
| 0.4944 | 1.734(6) | 2.800(7) | 2.37(1) |
| 0.9944 | 2.334(9) | 3.721(8) | 3.348(6) |
| 1.9944 | 3.469(9) | 5.47(1) | 5.135(10) |
| 2.9944 | 4.554(9) | 7.19(1) | 6.87(1) |
| 3.9944 | 5.631(8) | 8.870(6) | 8.58(1) |

Figure 2.2: The numerical results of the value of the dimensionless functions. This figure is from Ref. [153]

where $\theta_0 \equiv \theta(0) = \frac{1}{\pi}\ln(\xi/\xi_\mu)$.

In brief, the equation of state and superfluid density around the critical point are contained in the functions $\theta(X)$ and $f(X)$, which are calculated by Monte Carlo simulations. The numerical results are shown in figure 2.2. With the numbers in this table, the equation of state and superfluid density can be reconstructed via the above formulas.

### 2.2.4 BKT transition for 2D bosons with the presence of disorder

The BKT phase transition for 2D bosons has been shown to be stable against a certain disorder potential [154]. In the superfluid phase, the correlation function has an algebraic decay as $G(r) \propto r^{-\eta}$. The susceptibility is related to the correlation function as $\chi_s = \frac{1}{L^2}\int d\mathbf{r}d\mathbf{r}'\langle\psi^\dagger(\mathbf{r})\psi(\mathbf{r}')\rangle$. This double integral can be decoupled as an integral over one coordinate and another integral over the relative difference of the two coordinates. For a system with linear size $L$, each integral gives a factor $L^2$. So the susceptibility has a finite size scaling as $\chi_s \sim L^{2-\eta}$. In particular, at the critical point where $\eta = 1/4$, the susceptibility has finite size scaling as $\chi_s \sim L^{7/4}$. So rescaled susceptibilities $\chi_s/L^{7/4}$ for different system sizes should cross at a single point, which is just the critical point of the BKT phase transition. Monte-Carlo calculations show that this behaviour is still valid for 2D bosons in the presence of disorder, see Fig 2.3(left). In addition, the critical point of the BKT transition is recovered by shifting the chemical potential by the average value of the disorder potential, see Fig 2.3(right).

## 2.3 Bosons in a lattice

The dilute Bose gas make it possible in experiments to confine the bosons in deep lattices by utilising the optical lattices. This can give new phases in addition to the superfluid of bosons.

### 2.3.1 Superfluid-Mott insulator transition for Bose-Hubbard model

A discrete lattice model can be obtained from the continuous system by introducing the localized Wannier functions and using these wavefunctions as the basis of the Hilbert space. If the first energy band is well separated from the other bands, it is reasonable to restrict the Hilbert space to the first band. In addition, if the Wannier functions decay fast over a lattice space, we can consider only the nearest neighbour hopping. These considerations lead to the Bose-Hubbard model, with Hamiltonian

$$H = -J\sum_{\langle ij\rangle} a_i^\dagger a_j + \frac{U}{2}\sum_i n_i(n_i-1) + \sum_i \epsilon_i n_i \tag{2.39}$$

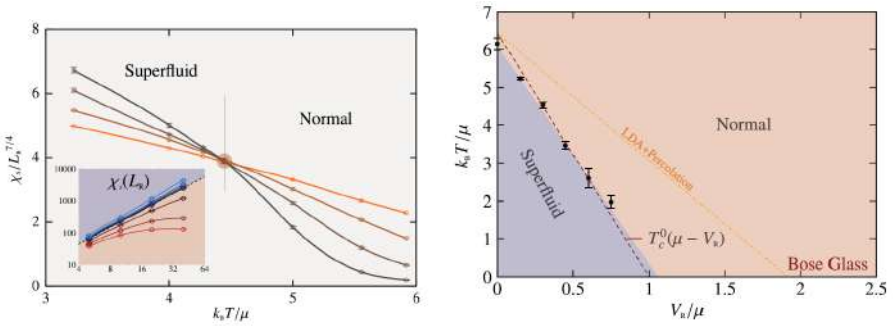


Figure 2.3: Left: Scaled superfluid susceptibility against temperature for system sizes in the range $L_R = L/\sigma_R = 5 - 40$ with $\sigma_R$ the correlation radius of disorder, at disorder strength $V_R/\mu = 0.3$ and interaction strength $\tilde{g} = 0.1$. Darker curves mark increasingly large sizes. In the inset, the susceptibility is shown as a function of $L_R$ (temperature increases from top to bottom). The divergence predicted by the BKT transition for clean systems ($\eta = 1/4$) is indicated by the dashed line. Right: Phase diagram of two-dimensional interacting bosons at fixed chemical potential and interaction strength $\tilde{g} = 0.1$. The dark dashed line is the critical temperature of the clean system with a renormalized chemical potential. For strong disorder, the normal system goes to the Bose-glass phase in the zero-$T$ limit. These two figures are from Ref. [154]

where $\langle ij \rangle$ denotes summation over nearest neighbours.

The physics of the Bose-Hubbard model is governed by the competition between the kinetic energy $J$ and interaction energy $U$. The kinetic term tends to delocalize particles over lattice sites in an extended Bloch state, while the interaction term tends to localize each particle on a single site. Consequently, in the limit of $U \to 0$, the bosons are in a superfluid phase, while in the limit of $J \to 0$, the bosons will be in a Mott insulator phase with integer number of bosons on each site. The overall phase diagram is shown in Fig 2.4(left).

At the limit of zero hopping $J = 0$, the system is separated on each site and the Hamiltonian of each site is diagonal in the particle number $n_i$ of each site. The system is clearly in a Mott insulator phase with each site populated by an integer number of bosons. Its energy spectrum has a Mott gap of order $U$. The particle number is governed by the chemical potential $\mu$ in the unit of interaction $U$. Now we turn on the hopping term. For small hopping $J$, the system can be understood in the perturbation picture as the energy differences between unperturbed states are of order $U$. Then the unperturbed states are coupled to other states by the hopping terms. The hopping terms conserve the total particle number. So with nonzero $J$, though there is fluctuation of particle number $n_i$ on each site, the average particle number of the total system is still an exact integer. This gives the Mott lobes in Fig 2.4(left). For larger particle number on each site, the $\sqrt{n}$ matrix elements of bosons effectively enhance the hopping strength. So the Mott lobes for larger $n$ is smaller in the range of $J/U$.

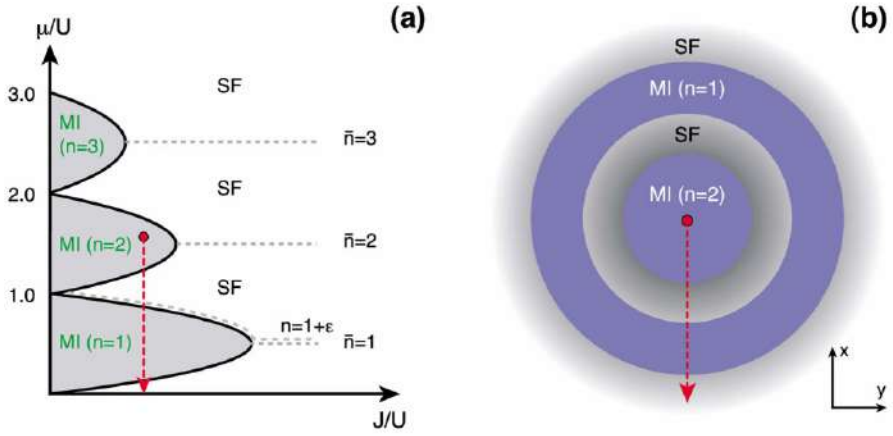


Figure 2.4: Schematic zero-temperature phase diagram of the Bose-Hubbard model. Dashed lines of constant-integer density $< \hat{n} >= 1, 2, 3$ in the superfluid hit the corresponding Mott insulator phases at the tips of the lobes at a critical value of $J/U$, which decreases with increasing density $\overline{n}$. For $< \hat{n} >= 1 + \epsilon$ the line of constant density stays outside the $\overline{n} = 1$ Mott insulator because a fraction $\epsilon$ of the particles remains superfluid down to the lowest values of $J$. In an external trap with an $\overline{n} = 2$ Mott insulator phase in the center, a series of Mott insulator and superfluid regions appear on going toward the edge of the cloud, where the local chemical potential has dropped to zero. These two figures are from Ref. [26]

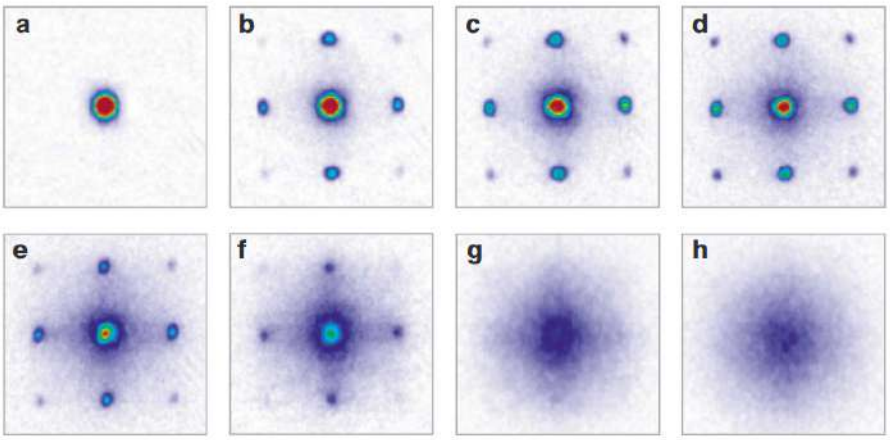


Figure 2.5: Absorption images of multiple matter-wave interference patterns after atoms were released from an optical lattice potential with a potential depth of (a)$0E_r$,(b)$3E_r$,(c)$7E_r$,(d)$10E_r$,(e)$13E_r$,(f)$14E_r$,(g)$16E_r$, and(h)$20E_r$. The ballistic expansion time was 15ms. These figures are from Ref. [71].

Although a superfluid is a $U(1)$ symmetry breaking phase, the $d$ dimensional zero temperature superfluid transition between Mott insulator and superfluid is actually not always in the universality class of the $(d+1)$ dimensional XY model. Such a $(d+1)$ dimensional XY model universality class is only realized at the multicritical points as we follow the constant-density curves on the phase diagram. On the other hand, the superfluid transitions in general, for example as we follow the red dashed line in Fig 2.4(left) by changing the chemical potential, behaves as the zero-density transition when the boson density is increased from zero in the absence of external potential, i.e. a vacuum-superfluid transition.

If we start at a point in a Mott lobe and then decrease the chemical potential, as the red arrow in Fig 2.4(left), the system will go through a series of Mott insulator and superfluid phase. In experiments, the Bose gas is usually trapped in a harmonic potential well. Under the local density approximation, the local chemical potential decreases from the trap center to the periphery. So there is a bunch of rings of superfluid and Mott insulator phases next to each other.

In experiments, the ratio $J/U$ can be tuned through the strength of the optical lattice. The dependence of hopping $J$ on lattice depth $V$ has an exponential factor, while the interaction $U$ approximately depends on lattice depth $V$ as a power law. So changing the lattice depth $V$ can greatly change the ratio $J/U$. This superfluid to Mott insulator phase transition was initially observed experimentally by a time-of-flight method [71], see Fig 2.5. For a weak lattice potential, the system is in the superfluid phase. The phase coherence gives the diffraction pattern from the time-of-flight images. As the lattice potential increases, the system enters the Mott insulator phase and loses the phase

coherence. The diffraction patterns have no more sharp peaks.

### 2.3.2 Bose-Hubbard model with disorder

The Bose-Hubbard model with weak disorder potential was studied in Ref. [54]. In addition to the standard Bose-Hubbard Hamiltonian as in Eq. 2.39, there is additional random on-site potentials $\delta\mu_i$, with the strength of disorder given by a parameter $\Delta$. With the presence of the disorder, a third Bose glass phase exists in addition to the superfluid and Mott insulator phase for interacting bosons. Different from superfluid and Mott insulators, the Bose glass is a gapless compressible insulating phase.

For bosons in a random potential, if the interaction is zero, all bosons will be condensed in the localized eigenstate with lowest eigenenergy. For interacting bosons, repulsive interaction is essential to prevent all bosons from condensing in the same single particle eigenstate and the noninteracting bosons picture does not give a good starting point to perform a perturbative treatment. The phase diagram at zero temperature results from the competition of various factors. On the one hand, the kinetic energy tries to delocalize the bosons and reduce the fluctuations of phases. On the other hand, both repulsive interaction and the disorder try to localize the bosons and reduce the particle number fluctuations. The zero temperature phase diagram for bosons in a disordered potential is shown in Fig 2.6. Compared to Fig. 2.4, now the superfluid phase and Mott insulator phase are separated by the Bose glass phase, a localization phase due to the disorder potential. In addition, for strong disorders the Mott phase can be completely destroyed. The phase transitions between the superfluid phase, the Mott insulator phase and the Bose glass phase for 2D bosons in a quasicrystal potential will be one of the subject of the following chapters.

## 2.4 Path integral Monte Carlo for bosons

A successful numerical method for bosonic systems is the path integral Monte Carlo method [143], which was further improved by the worm algorithm [144, 145]. A detailed discussion of the approach can be found in Ref. [155]. In this part we will give a brief review of the key ideas of these numerical methods.

### 2.4.1 Path integral

Path integrals in general gives an alternative approach to quantum mechanics. The idea is that the evolution of a physical system just go through all processes, and the propagator in the end is a coherent summation of all probability amplitudes of each process [156]. The probability amplitude of a single process is the exponential of a phase, which is just given by the action of this process. The summation of all the processes is a path integral. The classical physics is the saddle point of this path integral in the limit $\hbar \to 0$.

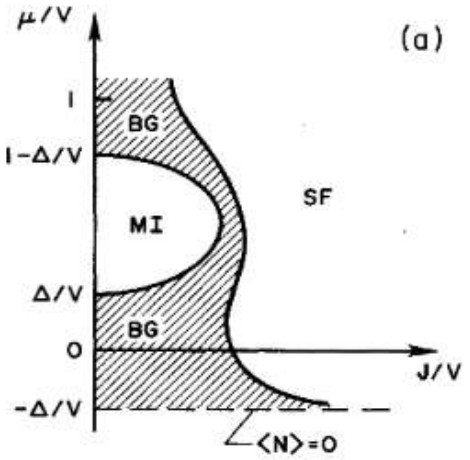


Figure 2.6: Zero-temperature phase diagram for the lattice boson model with weak bounded disorder, $\Delta/U < 1/2$, with $\Delta$ being the strength of the disorder. This figure is from Ref. [54]

Take a single particle for example. The propagator $K(x_2, t_2; x_1, t_1)$ between two space-time points $(x_1, t_1)$ and $(x_2, t_2)$, i.e. the matrix elements of the evolution operator $e^{-i\hat{H}t/\hbar}$, reads $\langle x_2| e^{-i\hat{H}(t_2-t_1)/\hbar} |x_1\rangle$. Dividing the time interval into $N = (t_2 - t_1)/\epsilon$ infinitely small steps $\epsilon$, permits the approximation of the form

$$e^{\epsilon(\hat{A}+\hat{B})} \simeq e^{\epsilon\hat{A}} e^{\epsilon\hat{B}} \tag{2.40}$$

which is generally not true for finite $\epsilon$ if $[\hat{A}, \hat{B}] \neq 0$. In particular, for Hamiltonian $\hat{H} = \hat{p}^2/2m + V(\hat{x})$, the propagator from $x$ to $x'$ during infinitely small time interval $\epsilon$ reads

$$\begin{aligned} K(x, x'; \epsilon) &= \langle x| e^{-i\hat{H}\epsilon/\hbar} |x'\rangle \\ &\sim \langle x| e^{-i\frac{\hat{p}^2}{2m}\epsilon} e^{-iV(\hat{x})\epsilon} |x'\rangle \\ &\sim \int dp \, \langle x| e^{-i\frac{\hat{p}^2}{2m}\epsilon} |p\rangle \, \langle p| e^{-iV(\hat{x})\epsilon} |x'\rangle \, . \end{aligned}$$

At this step, the operators disappear in the path integral formalism. Using $\langle x|p\rangle \sim e^{ipx/\hbar}$ we get

$$\begin{aligned} K(x, x'; \epsilon) &\sim \int dp \, exp\left[-i\frac{p^2}{2m}\epsilon + ip(x - x')/\hbar - iV(x)\epsilon\right] \\ &\sim \exp\left\{i\frac{\epsilon}{\hbar}\left[\frac{m(x - x')^2}{2\epsilon^2} - V(x)\right]\right\} \end{aligned}$$

upon completing the square and performing the Gaussian integral of $p$, with all normalization prefactors omitted. Note that for infinitely small $\epsilon$, $\frac{x-x'}{\epsilon}$ is just

the velocity and $\frac{m(x-x')^2}{2\epsilon^2} - V(x)$ is just the Lagragian $L$, so the infinitely small time propagator is

$$K(x, x'; \epsilon) \sim e^{i\frac{\epsilon}{\hbar}L} \tag{2.41}$$

For a certain path $x(t)$, the total phase is just $\frac{i}{\hbar}\int dtL = \frac{i}{\hbar}S(x(t))$, with $S(x(t))$ the action of the path $x(t)$. The total propagator is the path integral of all paths, as

$$K(x_2, t_2; x_1, t_1) \sim \mathcal{D}x(t)\, e^{\frac{i}{\hbar}S(x(t))}. \tag{2.42}$$

A thermal density matrix with Gibbs distribution is of the form $\rho \sim e^{-\beta H}$. This is of the same mathematical form as the evolution operator $e^{-iHt/\hbar}$, with the only difference that the prefactor of $H$ is a real number $\beta$ instead of $\frac{it}{\hbar}$. A path integral formalism can also be written for a density matrix at finite temperature by taking an imaginary time. At temperature $T = \frac{1}{k_B\beta}$, the density matrix $\rho = \exp(-\beta H)$ can be rewritten as

$$\rho \sim [\exp(-\epsilon H)]^N \tag{2.43}$$

with $\epsilon = \beta/N$. A small $\epsilon$ allows for approximations when calculating the matrix elements of the propagator $\exp(-\epsilon H)$ of a small time slice.

### 2.4.2 Path integral Monte Carlo for bosons

The path integral formalism can be applied to many body systems composed of identical bosons. A typical quantity to be calculated is the mean value of an observable $A$,

$$< A >= Tr(\rho A) = \int d\mathbf{R}\, \langle \mathbf{R}|\, \rho A S\, |\mathbf{R}\rangle \tag{2.44}$$

where $\rho$ is the density matrix and $\mathbf{R} = (\mathbf{r_1}, \mathbf{r_2}, ...)$ represents the set of positions of all bosons. A symmetrization operator $S = \frac{1}{N!}\sum_\sigma |\sigma\mathbf{R}\rangle \langle \mathbf{R}|$ is included to take into account the particle exchanges due to indistinguishability of bosons, by averaging over all permutations $\sigma$ of $N$ elements. In the path integral formalism, the mean value of $A$ reads

$$<A>=\int d\mathbf{R_0}...d\mathbf{R_{N-1}}\langle \mathbf{R_0}|e^{-\epsilon H}|\mathbf{R_{N-1}}\rangle\langle \mathbf{R_{N-1}}|e^{-\epsilon H}|\mathbf{R_{N-2}}\rangle...\langle \mathbf{R_1}|e^{-\epsilon H}AS|\mathbf{R_0}\rangle \tag{2.45}$$

The sets $\mathbf{R_0}, \mathbf{R_1}, ..., \mathbf{R_{N-1}}$ give the paths of all bosons in the imaginary time direction, see Fig. 2.7, and the mean value of $A$ becomes an integral over all possible paths. The ensemble of $\mathbf{R_0}, \mathbf{R_1}, ..., \mathbf{R_{N-1}}$ is called a configuration.

The Monte Carlo method gives an efficient way of calculating integrals. This is how Monte Carlo enters the story. For example, instead of calculating the exact integral $I = \int dx\ f(x)$, we can rewrite this integral as $I = \int dx\ p(x)\frac{f(x)}{p(x)}$ with $p(x)$ a probability distribution of variable $x$. The Monte Carlo method samples a random variable $x_i$ according to the probability distribution $p(x)$ and then take the statistical average $\frac{1}{N}\sum_{i=1}^{N}\frac{f(x)}{p(x)}$. This will not give the exact result of the integral, but for large $N$, it can give a reasonably good estimation of the

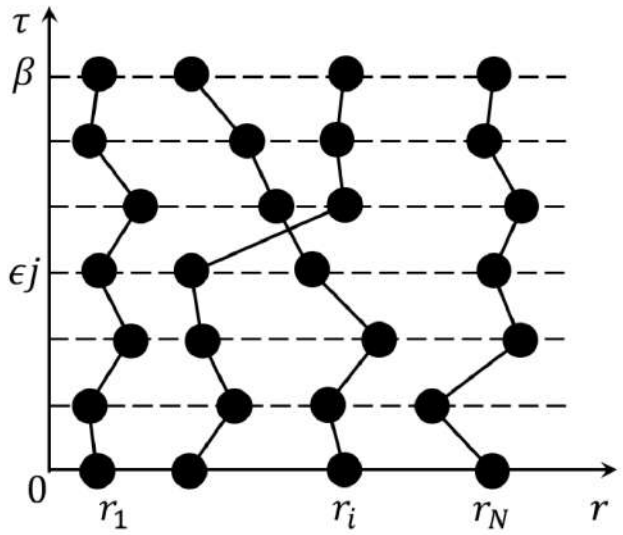


Figure 2.7: Path integral representation of the many particle propagator. The plot illustrate a configuration of $N$ particles.

integral with much less computation resources compared to directly calculating the integral exactly.

The path integral is just an integral over all configurations with corresponding weights. This integration over configurations can be calculated by the Monte Carlo method, with sampling weights calculated from the matrix elements of short time propagator $e^{-\epsilon H}$. The sampling is generated with a Markov chain, by proposing a certain move and then deciding whether to accept this move or not, respecting the configurations' relative statistical weights. The propose-and-judge process is to give high acceptance rates in practice. This Monte Carlo method is used to calculate the various physical observables. In particular, following the idea that the superfluid density can be obtained by a twisted boundary condition, superfluid density can be calculated with this path integral method by counting the total winding number, i.e. the total number of bosons going across the full system.

### 2.4.3 Worm algorithm

The path integral Monte Carlo method introduced above has an intrinsic drawback in the presence of Bose-Einstein condensation. The off-diagonal long-range order reflects the fact that bosons can be exchanged with each other with a very far distance between them. In the path integral numerical method, this becomes very inefficient because this kind of exchange processes will dramatically change the topology of the world lines and as a result it is very hard to efficiently sample this kind of processes. This problem can be improved by in-

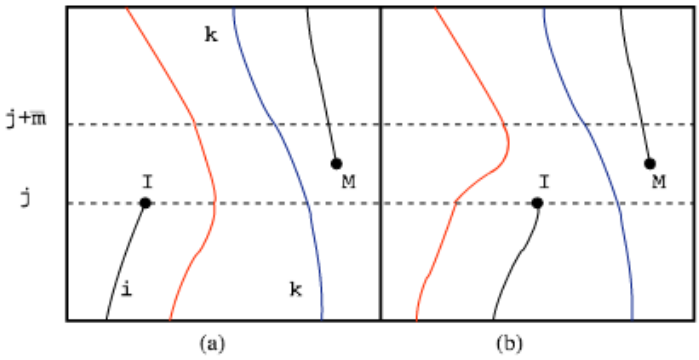


Figure 2.8: Schematic illustration of a swap move. (a) before the move. (b) after the move. This figure is from Ref. [144]

troducing the so-called worms, which are just open world lines, into the system. For example see Fig. 2.8 for a swap move, where the topological structure of the wordlines is changed by a local update of the wordlines. This makes the sampling of the exchange processes of bosons much more efficient, as it replaces a global update by a local update. The worm algorithm also helps for the calculation of Green's functions, as each configuration with open wordlines just corresponds to a single particle Matsubara Green's function.

# Chapter 3

# Localization and spectral structure

The physics of single quantum particles in a quasicrystal potential plays a important role, not only for their unique properties but also for understanding the many-body problem. For instance, it has been recently shown that the emergence of a Bose glass and an insulating Mott phase in strongly-correlated Bose gases subjected to shallow quasicrystal potentials can be related to localization and spectral gaps of noninteracting systems [157].

In this chapter, we investigate the localization properties and the structure of the energy spectrum of non-interacting quantum particles in two-dimensional quasicrystal potentials, as realized for ultracold-atom quantum simulators. To observe localization phenomena in quasicrystal potentials using cold atoms, the temperature should be small compared to the typical energy scale of the quasiperiodic structure. For a deep quasiperiodic potential, for example giving rise to a Aubry-André model upon discretization, the relevant energy scale is the tunnelling $J$, which is usually a small energy and reaching a temperature much below this scale could be challenging. On the other hand, for a shallow quasicrystal potential created by the optical lattice, the relevant energy scale is the recoil energy $E_r$. This is the limiting temperature of laser cooling. Ultracold atomic systems obtained by additional evaporation cooling is naturally much colder than this. So using a shallow quasicrystal potential has a practical advantage in ultracold atoms experiments. In addition, from the theoretical aspect, a shallow quasiperiodic potential also shows a novel localization picture compared to the deep lattice model. This was studied in one dimension for example in [38].

We show results for single particle properties of a 2D shallow quasicrystal potential in this chapter. While quantum states are generally localized at low energies and extended at high energies, we find an alternation of localized and critical states at intermediate energies. A finite-size scaling analysis of the inverse participation ratio unveils a power law scaling, with a non-integer fractal

dimension, for systems up to sizes of several hundreds of the natural length scale (optical wavelength). Furthermore, the energy spectrum shows a complex succession of bands and gaps, and we show that the most prominent gap is generated by localized ring states, and the gap width is controlled by the energy splitting between states with different quantized winding numbers.

We present our results as follows. We first show how the localizations can be quantitatively characterized by the inverse participation ratio (IPR) in Sec. 3.1. Then we recall the single particle properties of a 1D quasiperiodic potential in Sec. 3.2. A 2D optical quasicrystal with eight-fold rotational symmetry is introduced in Sec. 3.3 and we provide a general overview of the localization and spectral properties in Sec. 3.4. The localization properties are then discussed in greater detail within Sec. 3.5, including the structure of localized, critical, and extended states, and their identification from a finite-size scaling analysis of the inverse participation ratio. Next, in Sec. 3.6, we investigate the formation of gaps in the energy spectrum and show that they originate from localized ring states with different winding numbers. Finally, in Sec. 3.7, we extend this discussion to quasicrystal potentials with other discrete rotational symmetries, before ending with our conclusions and the implications of our results in Sec. 3.8.

## 3.1 Inverse participation ratio

Though a simple picture of localization can be visualized as whether a state extends across the system, a quantitative characterization of localization can be given by the so-called inverse participation ratio (IPR), defined as

$$\mathrm{IPR} = \frac{\int d\mathbf{r}|\psi(\mathbf{r})|^4}{(\int d\mathbf{r}|\psi(\mathbf{r})|^2)^2}. \tag{3.1}$$

To illustrate how it works, we consider several one dimensional examples, as shown in Fig. 3.1. The wavefunctions are of differernt forms and they are plotted in Fig. 3.1 with a typical length scale $a$ chosen to be $a = 1$ for the relevant cases. We take the system size to be $L$. Figure 3.1 (a) shows the wavefunction magnitude of a plane wave. It is clearly extended with a constant magnitude across the system, with IPR $= \frac{1}{L}$. For large $L$, the IPR is small. On the other hand, for localized states with typical length scale $a$, the IPR scales as $\sim \frac{1}{a}$. For example, a wavefunction $\psi(x) = \frac{1}{(2\pi a^2)^{1/4}} e^{-\frac{x^2}{4a^2}}$ which gives a Gaussian probability distribution, shown in Fig. 3.1 (b), has IPR $= \frac{1}{2\sqrt{\pi}a}$. And for a box wavefunction which only has non-zero magnitude $|\psi(x)| = \frac{1}{\sqrt{a}}$ for $x \in [0, a]$, see Fig. 3.1 (c), it has IPR $= \frac{1}{a}$. We see that for those wavefunctions with a length scale $a$, a small $a$ gives a large IPR. Typically a state tends to be extended if it has a large IPR and a state tends to be localized if it has a small IPR. However, this could actually be misleading, as we can see from the example shown in Fig. 3.1 (d). It depicts a wavefunction whose magnitude is a nonzero constant value in the ranges $x \in [n, n + r]$ for all integer values of $n$ and $0 < r < 1$. Its IPR is IPR $= \frac{1}{Lr}$. For a finite $L$, as is usually the case

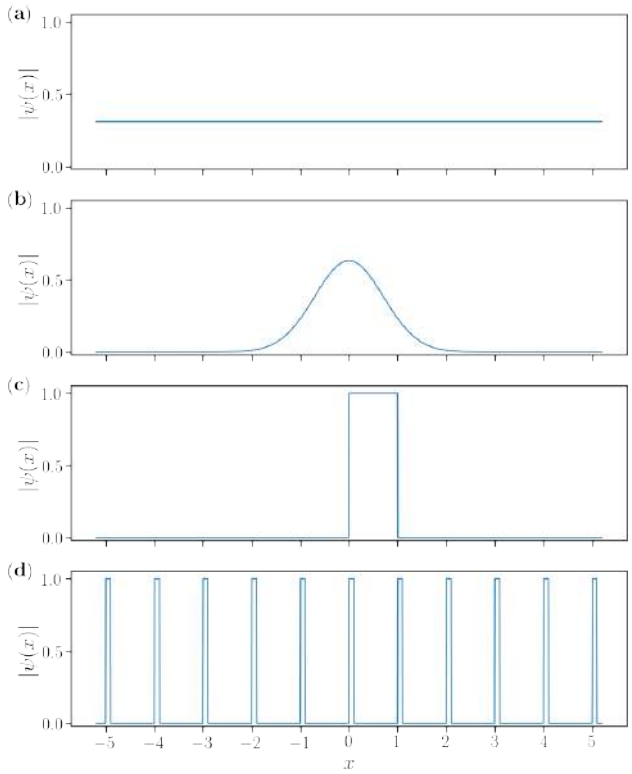


Figure 3.1: Various kinds of 1D wavefunctions. The length scale is $a = 1$ for the relevant cases.

for numerical calculations, we can get a large IPR if $r$ is small, even though this state is clearly an extended periodic state. A more rigorous analysis of localization should be done by looking at how the IPR scales with the system size $L$. In one dimensional systems, an extended state's IPR scales with system size $L$ as IPR $\sim L^{-1}$ and a localized state's IPR scales as IPR $\sim L^0$. We can see that the wavefunction of Fig. 3.1 (d) clearly has a IPR $\sim L^{-1}$ scaling as an extended state.

## 3.2 Single particle properties of 1D quasiperiodic potential

As we said, a shallow quasicrystal potential not only has certain advantages in cold atoms experiments but also can show different localization pictures compared to a deep lattice model. Here we review the results obtained for the

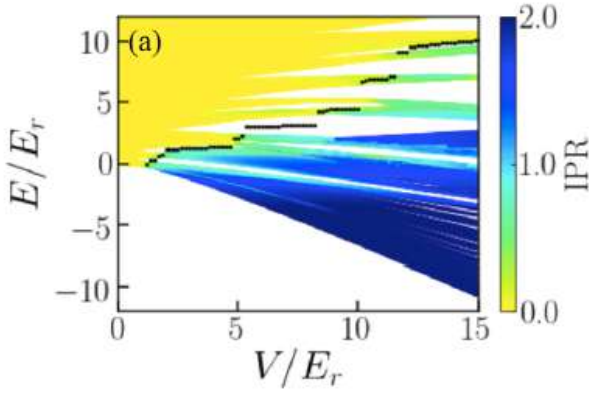


Figure 3.2: Localization transition for the balanced bichromatic potential, Eq. (3.2). IPR versus particle energy $E$ and lattice amplitude $V$ for the system size $L = 100a$. Localized states correspond to large values of the IPR (blue) and extended to vanishingly small values (yellow). The ME, found from finite-L scaling analysis of the IPR, is shown as black points. This figure is from [38].

one-dimensional case in continuous space [38]. The quasiperiodic potential reads

$$V(x) = \frac{V}{2}\cos(2k_1 x) + \frac{V}{2}\cos(2k_2 x + \phi) \tag{3.2}$$

with $k_2/k_1 = \frac{\sqrt{5}-1}{2}$ an irrational number. A relative phase shift is chosen as $\phi = 4$, avoiding any unnecessary special symmetry.

Eigenenergies and eigenstate wavefunctions are calculated by exact diagonalization for a system with size $L = 100a$ where $a = \pi/k_1$ notes the spatial period of the first periodic potential. The IPR is calculated for each single particle eigenstate. The IPR versus the eigenenergy $E$ and potential amplitude $V$ are shown in Fig. 3.2. The black dots indicating the mobility edge separating localized states and extended states, are obtained by finite size scaling analysis of the IPR. First we see that for low enough potential amplitude $V$ all the states are extended. So there is a critical potential, $V_c \simeq 1.112 \pm 0.002 E_r$, where the localized states start to appear for larger potential amplitude. For $V > V_c$, the localized states appear at low energy and extended states appear at high energy, separated by a single mobility edge. Furthermore, finite size analysis shows that the single particle gaps, as the white spaces between the colored bands shown in Fig. 3.2, have fractal structure. For larger system sizes, the gaps dissolve into smaller gaps in a fractal way.

We see that the localization picture is different from the 1D Aubry-André model. In the Aubry-André model, all states are extended below the critical point, while all states are localized above the critical point. Here in the shallow quasiperiodic potential we observe both localized states and extended states for $V > V_c$. In addition, the localized states and extended states are always

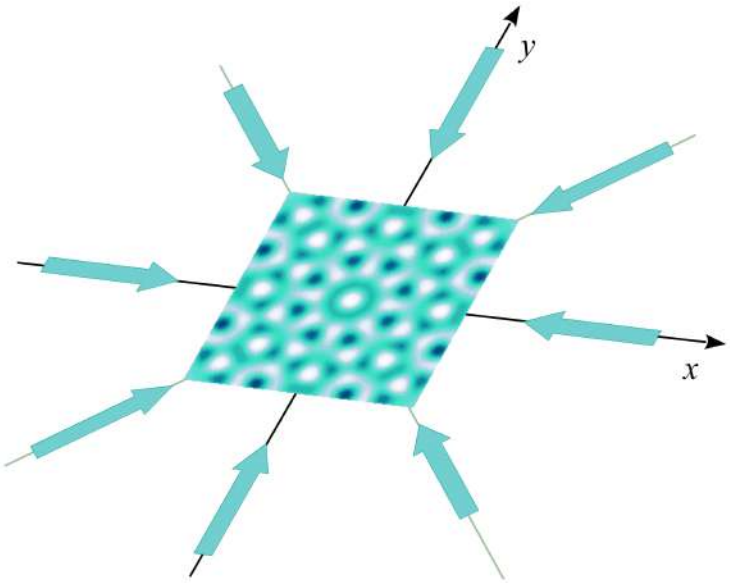


Figure 3.3: Two-dimensional optical quasicrystal for ultracold atoms. A 2D quasicrystal potential with eight-fold rotation symmetry is realized using four pairs of counterpropagating laser beams, making successive angles of 45° each, with small frequency shifts to suppress mutual coherence.

separated by a single sharp mobility edge. As we will see, this will not be the case for the 2D quasicrystal potential on which we will focus hereafter.

## 3.3 Two-dimension quasicrystal potential

We now turn to two-dimensional quasicrystals. A 2D quasicrystal potential can be created using an optical lattice by certain geometrical arrangements of multiple laser beams [46]. In particular, a 2D quasicrystal with 8-fold rotational symmetry can be created by four intersecting laser beams [48]. It is the sum of four one-dimensional standing waves with amplitude $V_0$ and lattice period $a = \pi/|\mathbf{G}_k|$, and successively rotated by an angle of 45°, see Fig. 3.3. It can be written as

$$V(\mathbf{r}) = V_0 \sum_{k=1}^{4} \cos^2 \left( \mathbf{G}_k \cdot \mathbf{r} + \phi_k \right), \tag{3.3}$$

with $\mathbf{G}_1 = \frac{\pi}{a}(1,0)$, $\mathbf{G}_2 = \frac{\pi}{a}(\frac{1}{\sqrt{2}}, \frac{1}{\sqrt{2}})$, $\mathbf{G}_3 = \frac{\pi}{a}(0,1)$, $\mathbf{G}_4 = \frac{\pi}{a}(-\frac{1}{\sqrt{2}}, \frac{1}{\sqrt{2}})$, position vectors $\mathbf{r} = (x, y)$ and phase factors $\phi_k$ of laser beam $k$. This potential can be realized in ultracold-atom experiments using four retro-reflected laser beams with slightly shifted frequencies to suppress mutual coherence [47, 49, 158]. This is the quasicrystal potential we consider. Generalizations to quasicrystal

potentials with higher rotational symmetries are discussed in Sec. 3.7.

The eight-fold quasicrystal potential with all $\phi_k = 0$ is shown at different length scales in Fig. 3.4(a), (b) and (c), which show the quasi-repetition of short-range structures. Here, we can observe the underlying eight-fold rotational symmetry, which is incompatible with periodic order. This is better seen in Fig. 3.4(d), which shows the Fourier transform of the 2D potential, Eq. (3.3). The discreteness of the Fourier pattern is a characteristic of long-range order, while the eight spots regularly arranged on a circle of radius $|k| = 2\pi/a$ directly reflects the eight-fold discrete rotational symmetry and absence of periodic order. For $\phi_k = 0$, the origin of the 2D system at $\mathbf{r} = 0$ is a rotational symmetry center. The spot at $k_x = k_y = 0$ is due to the finite average value of the potential, $\int \frac{d\mathbf{r}}{L^2} V(\mathbf{r}) = 2V_0$, where $L$ is the linear system size. It can be cancelled out by shifting the potential by $-2V_0$.

To avoid exact rotation symmetry around the center at $(x, y) = (0, 0)$, for the majority of our results, we consider an off-centered square area, which is more generic. For instance, it lifts exact degeneracies of strongly-localized states around potential minima, that are, however, very far apart from each other. This facilitates the discrimination of localized and extended states. In practice, we shift the center from $(x, y) = (0, 0)$ to $(x_0, y_0) = (-13543a, 196419a)$, which is far beyond the system borders we consider. This is equivalent to phase shifts of the laser beams with $\phi_1 = 0$, $\phi_2 \simeq 0.8597\pi$, $\phi_3 = \pi$, and $\phi_4 \simeq 1.5540\pi$. Note that the direction of the symmetry center to the system center is $\theta = \arctan(y_0/x_0) \simeq -86.06°$. It is away from any special directions associated with the discrete rotation symmetry, which are multiples of 22.5°.

## 3.4 Single particle spectrum

We now consider massive quantum particles in the quasicrystal potential of Eq. (3.3). The single-particle Hamiltonian is

$$H = \frac{\mathbf{p}^2}{2M} + V(\mathbf{r}), \tag{3.4}$$

where $\mathbf{p} = -i\hbar\nabla$ is the 2D momentum operator and $M$ is the particle mass. The eigenstates of this Hamiltonian are obtained using exact numerical diagonalization. In practice, the diagonalizations are performed in square areas of linear sizes $L$ with periodic boundary conditions. We use the lattice constant $a$ as the length unit and the recoil energy $E_\mathrm{r} = \pi^2\hbar^2/2Ma^2$ as the energy unit. We use the spatial discretization $dx = 0.1a$ and the typical system size is $L = 60a$, except whenever mentioned. Due to the finite discretization, only the lowest energy eigenstates are retained. They correspond to those whose variation scale $\lambda$ significantly exceeds the discretization $dx$. For an eigenstate with energy $E$, the typical de Broglie wavelength is $\lambda = \frac{2\pi\hbar}{\sqrt{2ME}}$, which yields the restriction on the eigenenergy as $E/E_\mathrm{r} \ll \frac{4}{(dx/a)^2} = 400$. In practice, we consider potential amplitudes up to $V_0 = 10E_\mathrm{r}$ and we keep the eigenstates up to energy $E = 8V_0$.

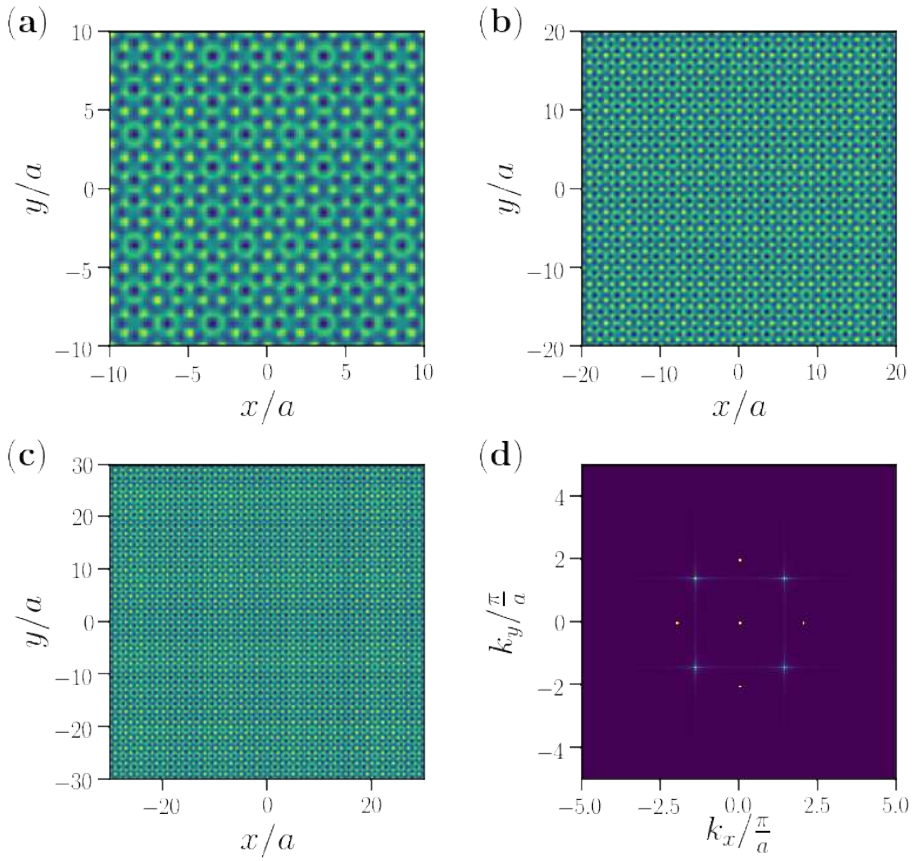


Figure 3.4: Eight-fold quasicrystal potential. (a)-(c) Real-space potential, Eq. (3.3) with $\phi_k = 0$ for all $k$, plotted at various scales, for the linear system sizes (a) $L = 20a$, (b) $L = 40a$, and (c) $L = 60a$, all centered at $\mathbf{r} = 0$. (d) Fourier transform of the potential. The color scale represents the value of the potential or its Fourier transform from low values (dark colors) to high values (light colors).

In the numerics, we must impose boundary conditions. Owing to the non-periodicity of the potential, any choice would distort the wavefunctions in the vicinity of the edges and some care should be taken over the states obtained in finite squares. We should indeed keep the states that faithfully represent the spectrum at thermodynamic limit, and discard the states that are created by boundary effects. Here, we choose periodic boundary conditions, where non-physical edge states may appear in the vicinity of the system boundaries. We have checked that such edge states disappear from their initial location when we repeat the diagonalization in a larger system; while new edge states appear near

the new boundaries, confirming that they are indeed created by the boundaries. To get a spectrum representative of the thermodynamic limit, these edges states are excluded as follows: We first reduce each wavefunction to a binary map. If the wavefunction magnitude at a certain position is larger than 10% of the maximum of the wavefunction magnitude, it maps to 1; Otherwise it maps to 0. Then, at each point with value 1, we compute the quantity $Z = 1-2d/L$, where $d$ the distance to the nearest edge, as well as, for each eigenstate, its average $\overline{Z}$. The criterion used in this work to only keep bulk states is the combination of the following two: (i) $\overline{Z} < 0.9$ and (ii) the position of the wavefunction maximum is at a distance larger than $3a$ from the nearest edge of the system. If an eigenstate fulfills both conditions, it is identified as a legitimate bulk state; Otherwise, it is identified as an edge state and is excluded.

Figure 3.5 shows the single-particle spectrum of the Hamiltonian versus the quasicrystal amplitude $V_0$ and the eigenenergy $E$, up to $8E_\mathrm{r}$ (the color scale represents the IPR of each eigenstate, see Sec. 3.5). The spectrum has a rich structure and shows a series of energy gaps (highlighted in red), each in specific ranges of the quasicrystal amplitude. The largest gap has been identified earlier [157, 159], while the smallest are more elusive. To locate these gaps systematically, we apply the following method for each spectrum corresponding to different values of $V_0$: For each set of successive 500 eigenstates, we calculate all the eigenenergy differences between neighbouring bulk states and then take the average value of all these eigenenergy differences. If any eigenenergy difference is larger than 50 times that mean value, it is identified as a gap. Otherwise, it is considered to be in an energy band.

We have checked that the gaps thus identified for a system of linear size $L = 60a$ agree with another approach where the energy resolution is fixed, and are stable against increasing system sizes: Careful identification of the true energy gaps in the spectrum can be captured by performing a finite-size scaling analysis. Here we compute the density of state (DOS) using

$$g_\epsilon(E) = \frac{\delta W(E,\epsilon)}{\epsilon}, \tag{3.5}$$

where $\epsilon = 0.005E_\mathrm{r}$ is a finite energy resolution and $\delta W(E,\epsilon)$ is the number of states in the energy window $[E, E+\epsilon)$. A good estimate of the DOS is obtained when the energy resolution $\epsilon$ is smaller than the typical variation scale of the DOS and larger than the inverse of the typical DOS so that several states are in each energy slice, $g_\epsilon(E)\epsilon \gg 1$. For the homogeneous 2D gas, we have $g(E)^{-1}E_\mathrm{r} = 4a^2/\pi L^2 \simeq 0.003$ for the smallest system size $L = 20a$.

Figure 3.6 shows the DOS per unit area versus energy for different system sizes from $L = 20a$ to $90a$. Each point with zero DOS gives an energy gap, so that all gaps larger than the energy resolution $\epsilon$ are revealed. For the smallest system size of $L = 20a$ in Fig. 3.6, the DOS displays many small gaps and a few large energy gaps. While the two large gaps are stable against increasing the system size, only a few small gaps survive for large system sizes. For the energy resolution $\epsilon = 0.005E_\mathrm{r}$, the structure of the spectrum is stable when the system size is larger than $L \simeq 60a$.

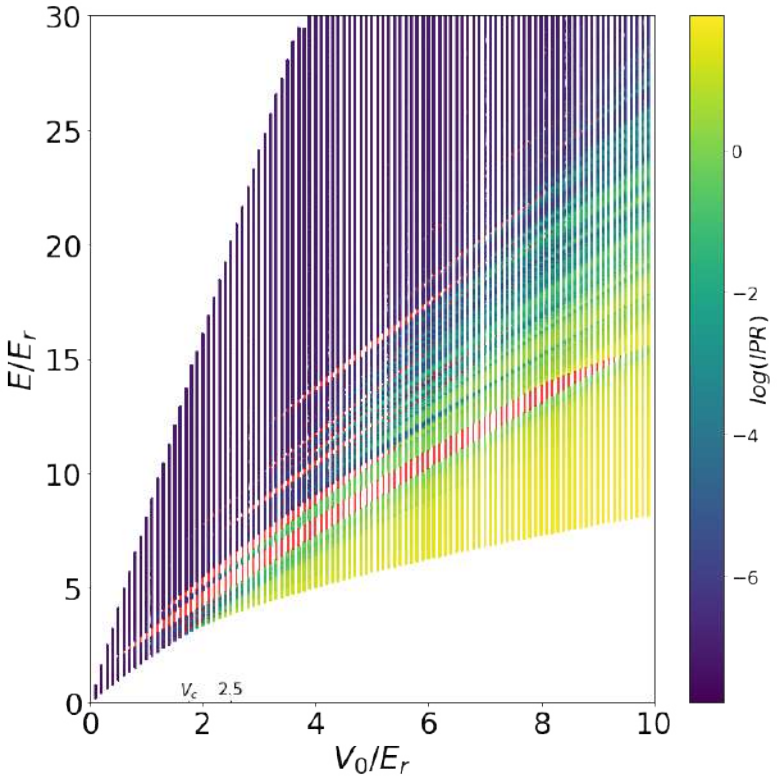


Figure 3.5: Energy spectrum of the 8-fold quasicrystal potential for various $V_0$. The system size is $L = 60a$, centered at $(x_0, y_0) = (-13543a, 196419a)$. We keep the eigenstates with energy up to $8V_0$ for potential amplitude $V_0 \lesssim 4E_\mathrm{r}$ and up to $30E_\mathrm{r}$ for larger potential $V_0$. The color scale shows the value of log(IPR) for each eigenstate, while the gaps are colored red.

## 3.5 Localization properties

Quasiperiodic systems are known to exhibit localization of eigenstates [19, 38, 81, 124, 160, 161]. To study these properties, we compute, for each single-particle eigenstate $\psi(\mathbf{r})$, the inverse participation ratio (IPR) as defined in Eq. 3.1. Generally, in sufficiently large systems, states with large IPR are localized while states with small IPR are delocalized, which may be either extended or critical. Figure 3.5 shows, for every eigenstate, log(IPR) versus $V_0$ and $E$ in color scale. For small quasicrystal amplitude $V_0$, all the eigenstates appear delocalized. This is consistent with the critical potential for localization $V_\mathrm{c} \simeq 1.76E_\mathrm{r}$, found in previous works [52, 162]. As $V_0$ increases, the low energy eigenstates tend to localize since long-range coherence is suppressed as the quasicrystal becomes deeper, while higher energy eigenstates remain delocalized.

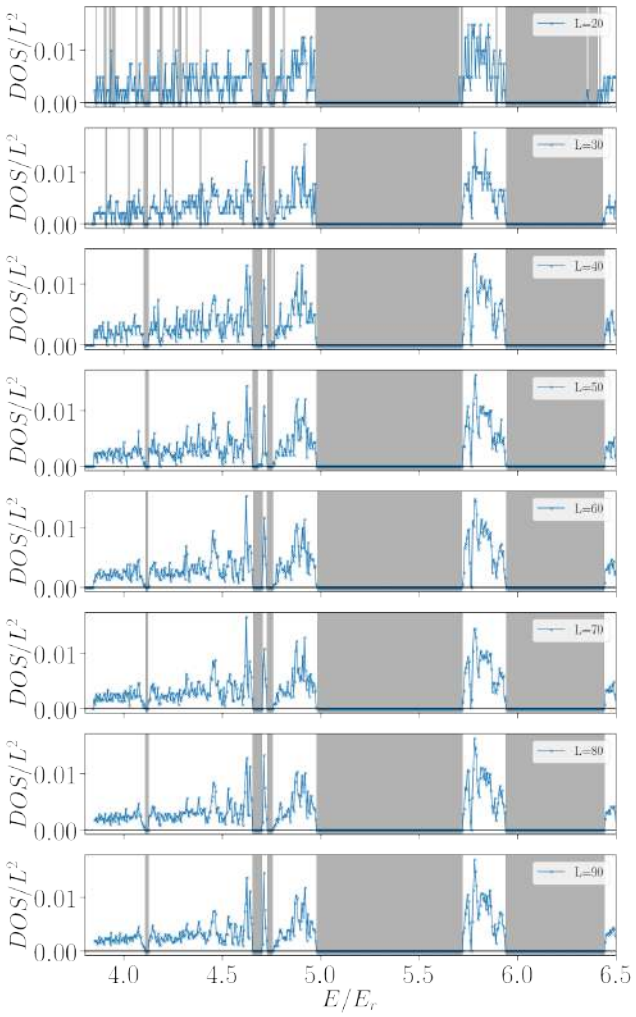


Figure 3.6: Density of states per unit area versus energy for the quasicrystal amplitude $V_0 = 2.5E_\mathrm{r}$ and the energy resolution $\epsilon = 0.005E_\mathrm{r}$. The various panels correspond to increasing system size from $L = 20a$ (top) to $L = 90a$ (bottom). The energy gaps are indicated by grey shaded areas.

In the intermediate energy range, the localization behaviour is richer. We find that eigenstates with large and small IPR coexist, and in particular, the IPR is nonmonotonous against energy.

### 3.5.1 Finite-size scaling analysis

As we have discussed in Sec. 3.1, to study localization in more detail, the bare value of the IPR is insufficient and we consider a more rigorous characterization of localization. It is provided by the scaling of IPR with the system size $L$, $\mathrm{IPR} \sim L^{\gamma}$. In 2D, localized states are characterized by $\gamma = 0$ and extended states by $\gamma = -2$. Any intermediate value of $\gamma$ between 0 and $-2$ then identifies a critical state [160, 161]. In the following, we focus on the case $V_0 = 2.5E_{\mathrm{r}}$, which is larger than the critical potential $V_{\mathrm{c}} \simeq 1.76E_{\mathrm{r}}$, but similar results are found for other amplitudes of the quasicrystal potential.

Studying the finite-size scaling properties of the IPR requires comparing eigenstates for different sizes. However, diagonalization in systems with different sizes gives different total numbers of eigenstates, as the density of states generally scales with the system area. Hence, given an eigenstate for a certain system size, there is always some arbitrariness on picking up the corresponding eigenstate for another system size to be compared with. To overcome this issue, we compute the averaged IPR of all eigenstates in a narrow energy window, $\overline{\mathrm{IPR}}$. The width of the energy window is chosen to be $\delta E = 0.01E_{\mathrm{r}}$, narrow enough such that the eigenstates in the energy window have similar localization properties, but large enough to have enough states to average. Then, the scaling exponent $\gamma$ considered below refers to this averaged $\overline{\mathrm{IPR}}$, and characterizes the localization properties in the corresponding energy window.

For instance, Fig. 3.7 shows the scaling of the IPR versus the system size from $L = 20a$ to $L = 300a$, for three different energy windows. In all cases, it shows a clear power-law scaling, $\mathrm{IPR} \sim L^{\gamma}$, and the exponent $\gamma$ is found by a linear fit of $\log\big(\overline{\mathrm{IPR}}\big)$ versus $\log(L/a)$. Figure 3.7(a1) corresponds to energy $E \simeq 4E_{\mathrm{r}}$. The quantity $\log\big(\overline{\mathrm{IPR}}\big)$ fluctuates with the system size but shows no clear increasing or decreasing tendency. Linear regression of the data points yields the slope $\gamma = -0.04 \pm 0.03$. The small value of $|\gamma|$ indicates that the states in this energy window are localized. An example of the wavefunction of an eigenstate in this energy window is plotted in Fig. 3.7(b1). The state is localized in a few local potential wells, consistently with strong localization. Figure 3.7(a2) corresponds to energy $E \simeq 6E_{\mathrm{r}}$. In this case, linear regression yields the slope $\gamma = -2.06 \pm 0.06$, corresponding to extended states. The wavefunction of an eigenstate in this energy window, shown in Fig. 3.7(b2), consistently covers the full system area, although not homogeneously. Finally, Fig. 3.7(a3) corresponds to energy $E \simeq 5.81E_{\mathrm{r}}$. It also shows a clear linear behaviour in log-log scale and the slope is found to be $\gamma = -1.25 \pm 0.09$, significantly far from both 0 or $-2$. In this energy window, the states are thus neither localized nor extended, i.e. they are critical. A typical eigenstate is plotted in Fig. 3.7(b3). Unlike localized states, these critical states extend over the full system but, compared to extend states, they only cover a limited proportion of the area.

Systematic finite size scaling and linear fits are performed over the full spectrum, with results shown in Fig. 3.8. Generally, the system sizes range from $L = 20a$ to $L = 100a$. For some energy windows, notably where critical states appear, we use larger sizes, up to $L = 300a$, so as to check that the scaling be-

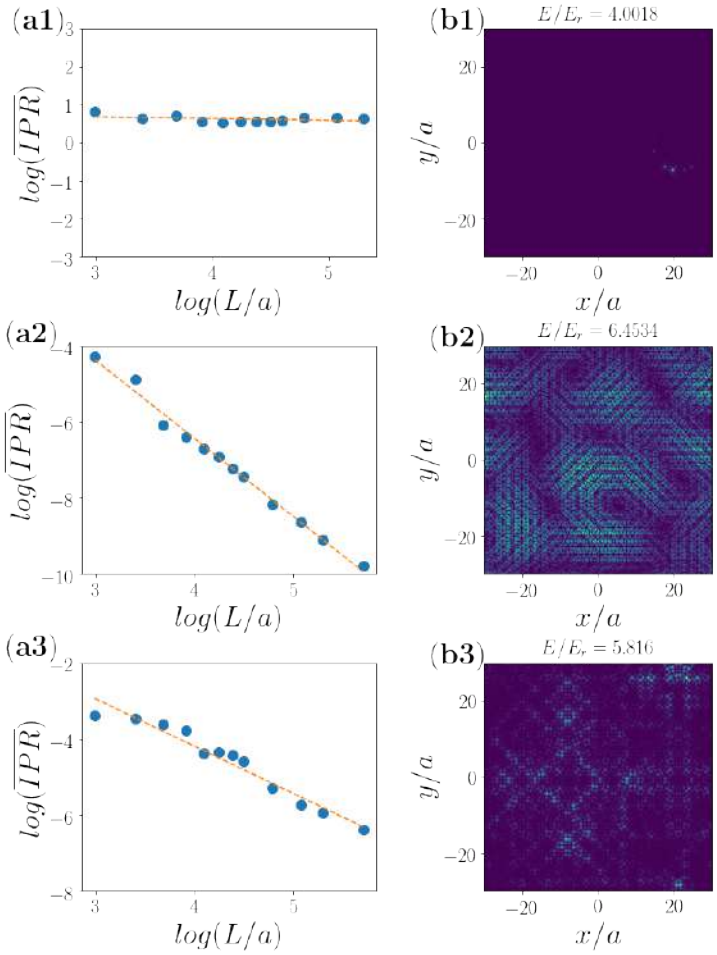


Figure 3.7: Localization properties of some eigenstates. The left column, (a), shows $\log\big(\overline{\mathrm{IPR}}\big)$ versus $\log(L/a)$ for all eigenstates in various energy windows. Blue disks are data points while orange dash lines show linear fits. The quasicrystal amplitude is $V_0 = 2.5E_\mathrm{r}$ and the system sizes for linear regressions range from $L = 20a$ to $L = 300a$. (a1) The energy window is $E/E_\mathrm{r} \in [4.00, 4.01]$ and the linear fit yields $\gamma = -0.04 \pm 0.03$. (a2) The energy window is $E/E_\mathrm{r} \in [6.45, 6.46]$ and the linear fit yields $\gamma = -2.06 \pm 0.06$. (a3) The energy window is $E/E_\mathrm{r} \in [5.81, 5.82]$ and the linear fit yields $\gamma = -1.25 \pm 0.09$. The right column, (b), show examples of eigenstates in the corresponding energy windows, with energies indicated on the top of each panel. The wavefunctions plotted here are computed for the system size $L = 60a$.

haviour of the IPR persists for larger system sizes. The exponent $\gamma$, such that $\mathrm{IPR} \sim L^\gamma$, is found from linear fits of $\log\big(\overline{\mathrm{IPR}}\big)$ versus $\log(L/a)$, with results

shown in the first row of Fig. 3.8. To characterize the fit quality, we compute the Pearson correlation coefficient,

$$r = \frac{\sum_i (x_i - \overline{x})(y_i - \overline{y})}{\sqrt{\sum_i (x_i - \overline{x})^2 \sum_i (y_i - \overline{y})^2}}, \tag{3.6}$$

for two data sets $x_i$, $y_i$ where $\overline{x}$ and $\overline{y}$ are their mean values. A value of $|r|$ close to 1 indicates good linear correlation between the data sets, while $|r|$ close to 0 indicates poor linear behaviour. The correlation coefficient for linear fitting of $\log\big(\overline{\mathrm{IPR}}\big)$ and $\log(L/a)$ is shown in the second row of Fig. 3.8. It shows good linear behaviour with $r \simeq -1$ and $\gamma \simeq -2$ for energy $E \gtrsim 6.45E_\mathrm{r}$, and the states in this energy range are clearly extended. For a lower energy range, however, the coefficients $r$ are much worse, which questions the corresponding results. This is actually misleading as when the slope $\gamma$ is about 0, even weak fluctuations of data points around a constant value can greatly affect the coefficients $r$.

To circumvent this issue, we repeat the linear regression for $\log\big(\overline{\mathrm{IPR}} \cdot L/a\big)$ versus $\log(L/a)$ with slope $\gamma' + 1$ and for $\log\big(\overline{\mathrm{IPR}} \cdot (L/a)^2\big)$ versus $\log(L/a)$ with slope $\gamma'' + 2$. The results, together with the corresponding correlation coefficients, $r'$ and $r''$ respectively, are shown in the lower rows of Fig. 3.8. The three linear regressions give almost indistinguishable results for the exponent $\gamma$, $\gamma'$, and $\gamma''$, and, for each energy $E$, at least one of the three correlation coefficients $r$, $r'$ or $r''$ is close to 1. For instance, the coefficient $|r''|$ has values away from 1 for $E \gtrsim 6.45E_\mathrm{r}$, since the slope $\gamma'' + 2$ for $\log\big(\overline{\mathrm{IPR}} \cdot (L/a)^2\big)$ is about 0. It is, however, close to 1 for low energy states, and the scaling given by $\gamma''$ (essentially equal to $\gamma$ and $\gamma'$) is reliable in this regime. In general, the fitted slope $\gamma$ yields the correct scaling and the quality is assessed by either $r$, $r'$ or $r''$.

The results show that the lowest energy states are localized, with $\gamma \simeq 0$. For energy $E \gtrsim 6.45E_\mathrm{r}$, i.e. above the second large energy gap, all states are extended, with $\gamma \simeq -2$. In the intermediate energy range, there are critical states whose scaling exponent $\gamma$ is neither 0 nor $-2$ but clearly in between. Taking into account the uncertainty of the fitted exponents $\gamma$, energy ranges with different kinds of localization properties can be identified as follows, with results shown in the lower row of Fig. 3.9: Localized states for $\gamma > -0.25$ (green), extended states for $\gamma < -1.75$ (blue), and critical states for $-1.75 < \gamma < -0.25$ (yellow). Also shown is log(IPR) for each eigenstate calculated for $L = 80a$ (red dots). The behaviour of the DOS shows that that there is a significant number of states of each kind in the spectrum. The behaviour of log(IPR) is rather smooth, up to significant fluctuations. Interestingly, we find that critical and localized states can coexist at intermediate energies, with no clear mobility edge, or separation between localized and critical domains. This is reminiscent of "anomalous mobility edges" separating bands of localized states and bands of critical states as found in other quasiperiodic models [45].

General properties of localized, extended, and critical states are further discussed in the following subsections.

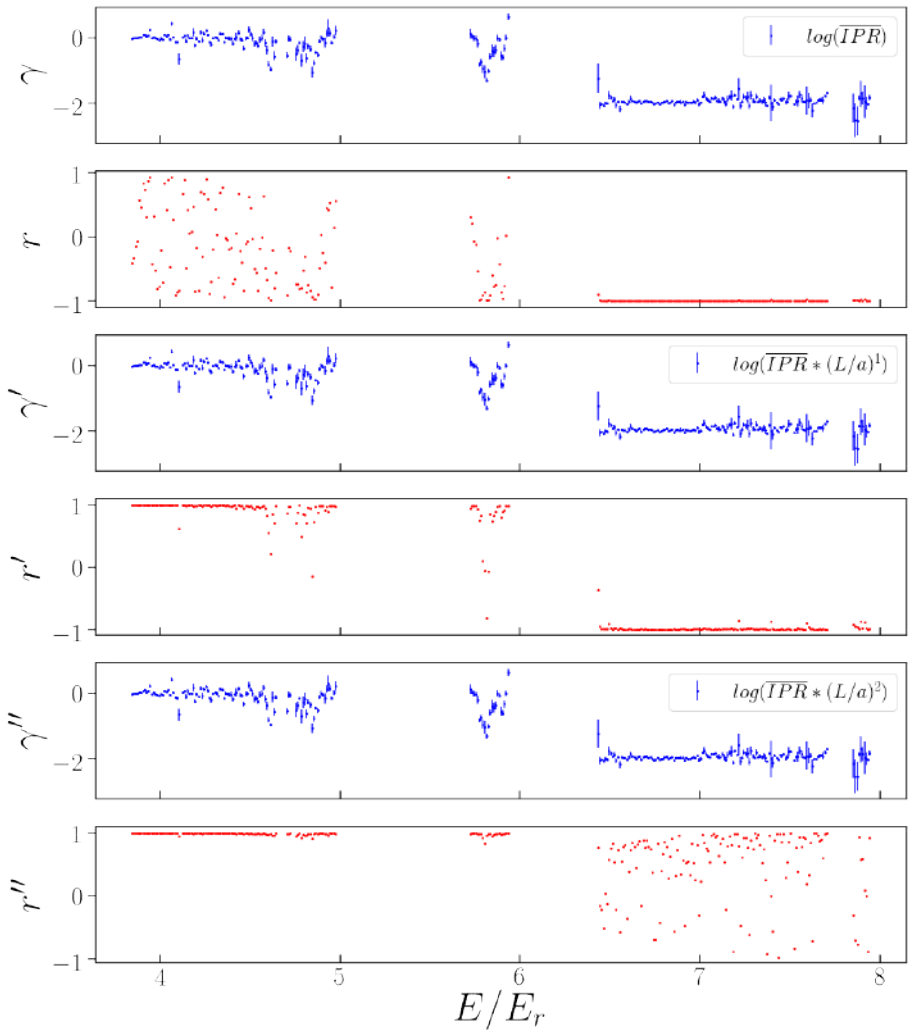


Figure 3.8: Finite size scaling of the IPR, performed as in Fig. 3.7, for system sizes ranging from $L = 20a$ to $L = 100a$, except in some narrow energy windows where data for larger sizes, $L = 120a, 160a, 200a, 300a$, are also calculated. The panels, from top to bottom, show, successively the scaling exponent and the corresponding regression coefficient: (i) $\gamma$ and $r$ for $\log\left(\overline{\mathrm{IPR}}\right)$ versus $\log(L/a)$, (ii) $\gamma'$ and $r'$ for $\log\left(\overline{\mathrm{IPR}} \cdot L/a\right)$ versus $\log(L/a)$, and (iii) $\gamma''$ and $r''$ for $\log\left(\overline{\mathrm{IPR}} \cdot (L/a)^2\right)$ versus $\log(L/a)$.

### 3.5.2 Localized states

Localized states generally appear in the low energy range, as well as at some energy band edges, near by energy gaps, see Fig. 3.9. Typical localized states $|\psi|$ in different energy ranges are plotted on Fig. 3.10, with eigenenergy increasing in the reader order, from panel (a) to panel (h). The insets show magnification of the main panel in the vicinity of the localization center. The states with lowest energies are strongly localized in a single local potential well, see Fig. 3.10(a). As the energy increases, the states start to cover a few potential wells. Some states are localized in regions where the local potential is almost eight-fold rotational symmetric, and the eigenstates form rings composed of eight almost equivalent spots, see Fig. 3.10(b). Similar ring states exist with 16 spots (not shown). Other localized states cover a small cluster of different potential wells, such that the tunnelling between them is large enough to compensate the eigenenergy differences between the local potential wells, see Figs. 3.10(c) and (d). As the energy further increases, states composed of one or many small rings begin to appear. Figure 3.10(e) shows such a localized state with one small ring, with eigenenergy slightly below the energy gap at $E \simeq 4.65E_{\mathrm{r}}$. The small ring actually corresponds to a set of several local shallow potential wells that are very near by each other, and the wavefunction on these wells merge into an almost homogeneous circle. Figures 3.10(f) and (g) are localized states with energies, respectively, right below and right above the first large energy gap in, approximately, $E/E_{\mathrm{r}} \in [5, 5.7]$. They are also states located on small rings of nearby potential wells, as for Fig. 3.10(e). However, unlike in Fig. 3.10(e),

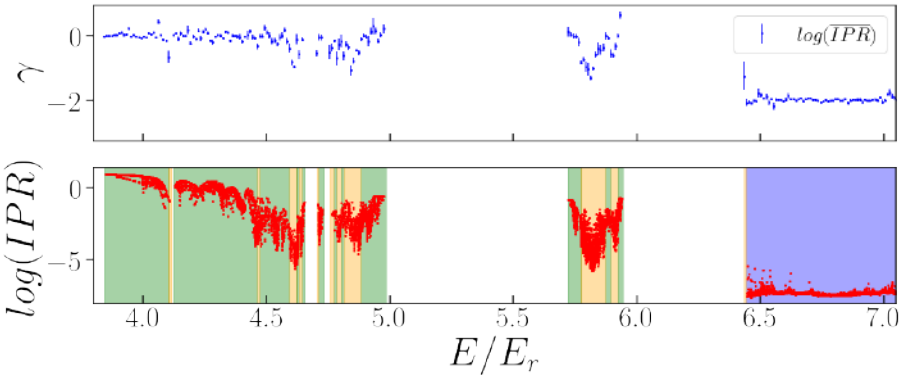


Figure 3.9: Localization spectrum in the quasicrystal potential. Upper row: Scaling exponent $\gamma$ of the IPR $\sim L^{\gamma}$. Same data as the first row of Fig. 3.8, for the convenience of comparison to the lower row. Lower row: Classification of different kinds of states. The values of log(IPR) for all eigenstates with system size $L = 80a$ is plotted versus their eigenenergies. Localization properties are shown as background colors: green for localized states, blue for extended states, and orange for critical states. The potential amplitude is $V_0 = 2.5E_{\mathrm{r}}$.

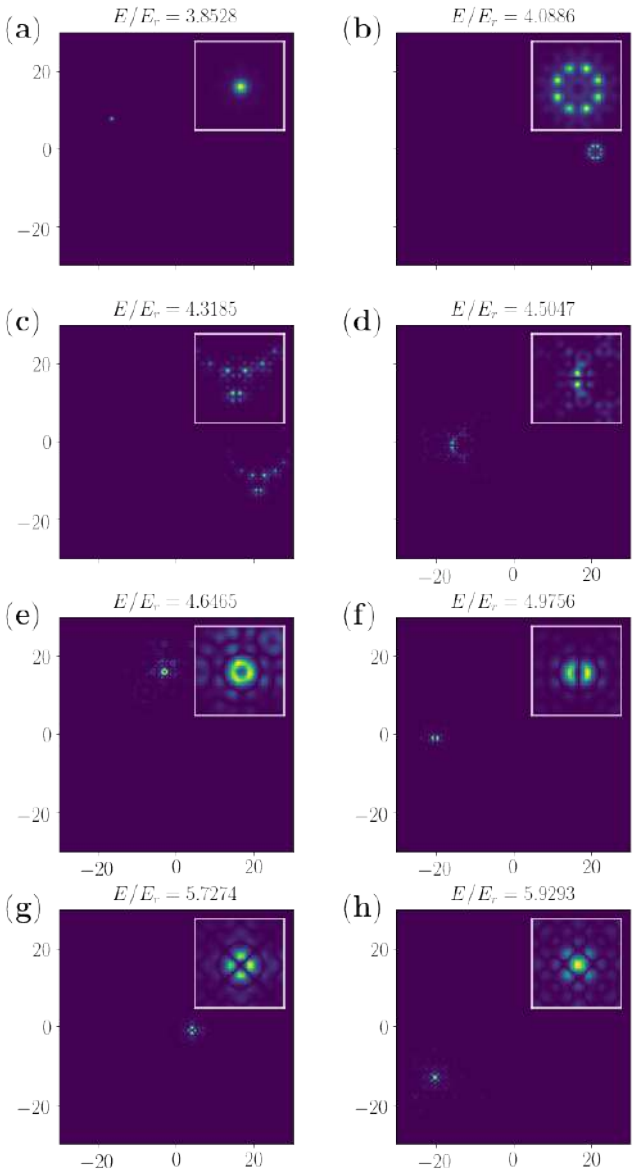


Figure 3.10: Wavefunctions of typical localized states in various energy ranges. The eigenenergy, indicated on the top of each panel, increases in the reading order, from (a) to (h). The quasicrystal potential amplitude is $V_0 = 2.5E_\mathrm{r}$ and the system size is $L = 60a$. The insets show magnifications of the corresponding panel in the vicinity of the localization center.

these small-ring wavefunctions have, respectively, one or two node lines due to different phase winding numbers. These states play special roles in the spectral structure and will be further discussed in Sec. 3.6. Localized states with relatively high energies do not all have similar ring structures. Some of these states are localized in one or multiple potential wells, as in Fig. 3.10(h).

### 3.5.3 Extended states

States with high enough eigenenergies are all extended, see Fig. 3.9. For a potential amplitude $V_0 = 2.5E_\mathrm{r}$, extended states appear after the second large gap, i.e. for energy $E \gtrsim 6.45E_\mathrm{r}$. Typical extended states are plotted in Fig. 3.11. They cover the full system area quasi-homogeneously, even though some dark node regions due to large scale modulation of the wavefunction may appear, as for instance in Fig. 3.11(a3). Extended wavefunctions contain many spots separated by node lines. For low-enough energy, each island has a size comparable with the lattice constant $a$, and forms a rather ordered pattern, see Fig. 3.11(a3). For states with higher energy, the wavefunction variations become stronger and the typical size of the islands gets smaller. It goes down to the de Broglie wavelength, $\lambda = 2\pi\hbar/\sqrt{2mE}$, of the quasi-plane waves rather than the potential profile. Correspondingly, the states show a complex, quite disordered, pattern determined by multiple scattering on the quasicrystal potential, see Figs. 3.11(a1) and (a2).

While the IPR alone does not seem to characterise the crossover from "ordered" extended states to "disordered" ones, a better understanding can be gained by looking at the density profiles in momentum space, as shown in Figs. 3.11 (b1), (b2), and (b3). Consider first the highest energy states [Figs. 3.11 (b1) and (b2)]. The momentum distribution of such states is concentrated around a marked circle, with a smaller spreading when the energy increases. This structure may be understood using simple perturbation theory: Extended states with high-enough energy $E$ are constructed from plane waves with momentum $k_E$ such that $E = \hbar^2 k_E^2/2M + \langle V \rangle$, where $\langle V \rangle \simeq 2V_0$ is the potential-energy contribution for purely plane waves. We consistently find that the circle with radius $k_E$ [shown in red in Figs. 3.11(b1), (b2), and (b3)] coincides with the dominant momentum components of the extended wavefunction. The quasicrystal potential weakly couples many plane waves with a modulus of the momentum nearly equal to $k_E$ in almost all directions and within a structure consistent with the quasicrystalline eightfold rotational symmetry.

The formation of the momentum profile of extended states at a smaller energy is more subtle. In this case, the extended wavefunctions are dominated by the quasicrystal potential and we now have a quasiperiodic, lattice-like structure [Fig. 3.11(b3)]. The origin of this structure can be deduced as follows. First, we note that the extended state in real space is made of hybridized ring states with 3 nodes lines. The rings are located around some potential maxima, which forms a discrete lattice in real space, shown in Fig. 3.11(a4). The wavefunction

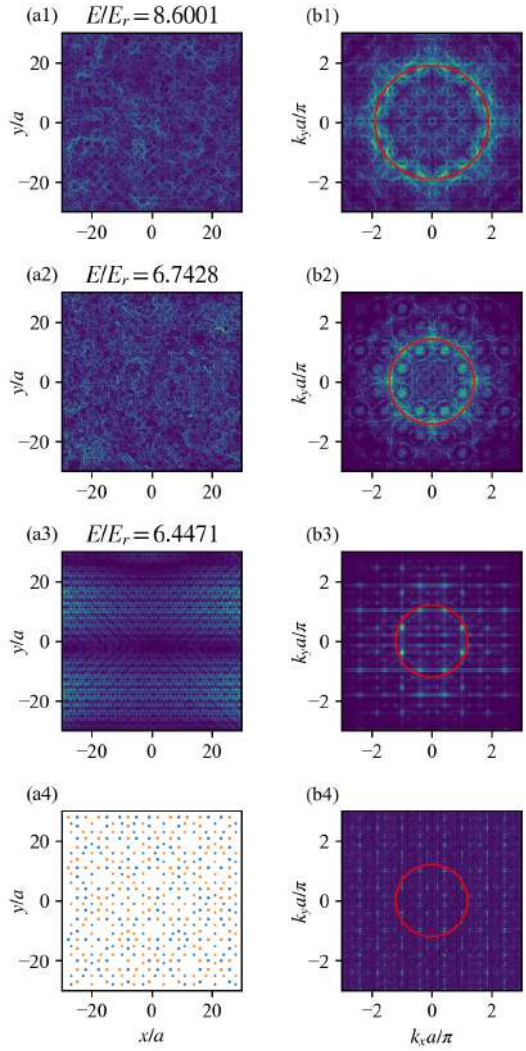


Figure 3.11: Wavefunctions of extended states, with energies given on top of each panel, $V_0 = 2.5E_\mathrm{r}$, and $L = 60a$. We show the (a1)-(a3) real-space density profiles and corresponding (b1)-(b3) Fourier space momentum distributions. The red circle indicates the momentum $k_E$ given by a perturbation theory. Panels (a4) and (b4) show the reconstructed components of (a3)-(b3), Eq. (3.8). The spots in (a4) show the positions of the local maxima $\mathbf{r}_j$, with color indicating the phase (blue : $\phi_j = 0$, orange: $\phi_j = \pi$). Panel (b4) shows the square modulus of the Fourier transform of Eq. (3.8). The positions of spots in (b4) match well with those in (b3).

can thus be approximated as

$$\psi(\mathbf{r}) \simeq \int d\mathbf{r}' \psi_0(\mathbf{r}) f(\mathbf{r} - \mathbf{r}') \tag{3.7}$$

and

$$f(\mathbf{r}) = \sum_j e^{i\phi_j} \delta(\mathbf{r} - \mathbf{r}_j), \tag{3.8}$$

where $\psi_0(\mathbf{r})$ is a sample of the ring states with 3 node lines, $\mathbf{r}_j$ is the position of the $j$th potential maxima and $\phi_j$ is a phase factor of either 0 or $\pi$, which gives the correct alignment of the local structures in the original wavefunction. The phase factor is encoded in the color (blue or orange) of the lattice points in Fig. 3.11(a4). To check this interpretation, we compute the Fourier transform of $f(\mathbf{r})$ in Eq. (3.8) and plot it in Fig. 3.11(b4). The result reproduces well the primary features of the momentum profile found in Fig. 3.11(b3), namely the quasiperiodic, lattice-like structure, and some of the most significant spots. This shows that the structure of the lowest-energy extended states is strongly related to the quasiperiodic nature of the potential. When the energy $E$ is further increased, the quasiperiodic structure becomes less significant, with the progressive emergence of the plane-wave momentum circles observed in Figs. 3.11(a1) and (a2).

### 3.5.4 Critical states

Critical states generally appear in between the localized states not far from the edges of energy bands, see Fig. 3.9. The critical states typically extend across the full system, with complex geometrical patterns, separated in different classes, see Figs. 3.12 and 3.13.

Figure 3.12 displays the states with energy closest to $E = 4.6218E_{\mathrm{r}}$ for different system sizes. For this energy, the scaling exponent is $\gamma = -1.49 \pm 0.24$, clearly different from 0 and $-2$. As visible on Fig. 3.12(a), these critical states are all composed of the small rings, similar to localized states with no node lines in the rings as in Fig. 3.10(e). These critical states, which contain a countless number of the small rings, have energies slightly smaller than the localized states containing only one or a few small rings, owing to hybridization, which minimizes the tunnelling energy. Since the ring states that form the building blocks of such critical states are roughly isotropic, they do not favor any clear direction, and, on a larger scale, they group together and form larger ring structures containing eight small rings, and eventually form a "ring of ring", see Fig. 3.12(b). On even larger scales, these rings of rings also group together forming more complex structures, see Figs. 3.12(c)-(h).

Fig. 3.13 shows an example of another class of critical states, found at a higher energy. It displays the states with energy closest to $E = 5.803E_{\mathrm{r}}$ for different system sizes. Here the scaling exponent is $\gamma = -0.87 \pm 0.18$, also corresponding to critical states. However, unlike Fig. 3.12, which contains rings at different scales, Fig. 3.13 displays square-shaped structures. On large enough

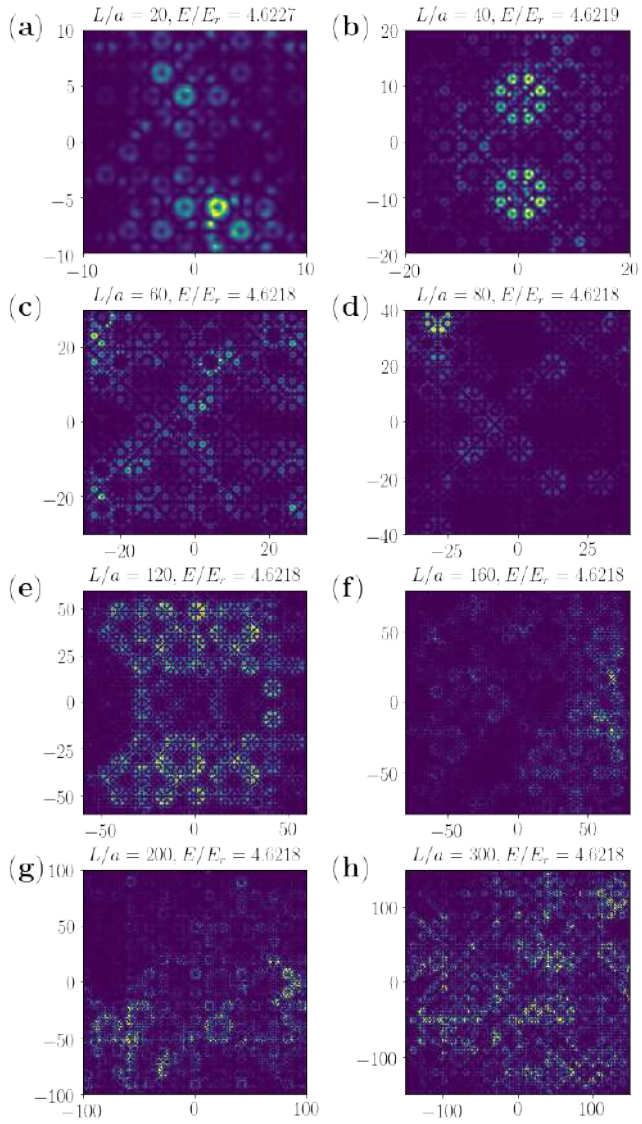


Figure 3.12: Wavefunctions in the critical regime at $E \simeq 4.6218E_{\rm r}$ for $V_0 = 2.5E_{\rm r}$, shown at different scales. The various panels show the wavefunction of the state with eigenenergy closest to $E = 4.6218E_{\rm r}$ for system sizes increasing in the reader order, from (a) $L = 20a$ to (h) $L = 300a$. Note that the colors have been rescaled to increase the contrast.

scales, we find that these states display straight lines either along the main axes ($x$ and $y$) or along the diagonals. In fact, these states are also built from ring states, but here with two node lines, similar to that shown on Fig. 3.10(g). For

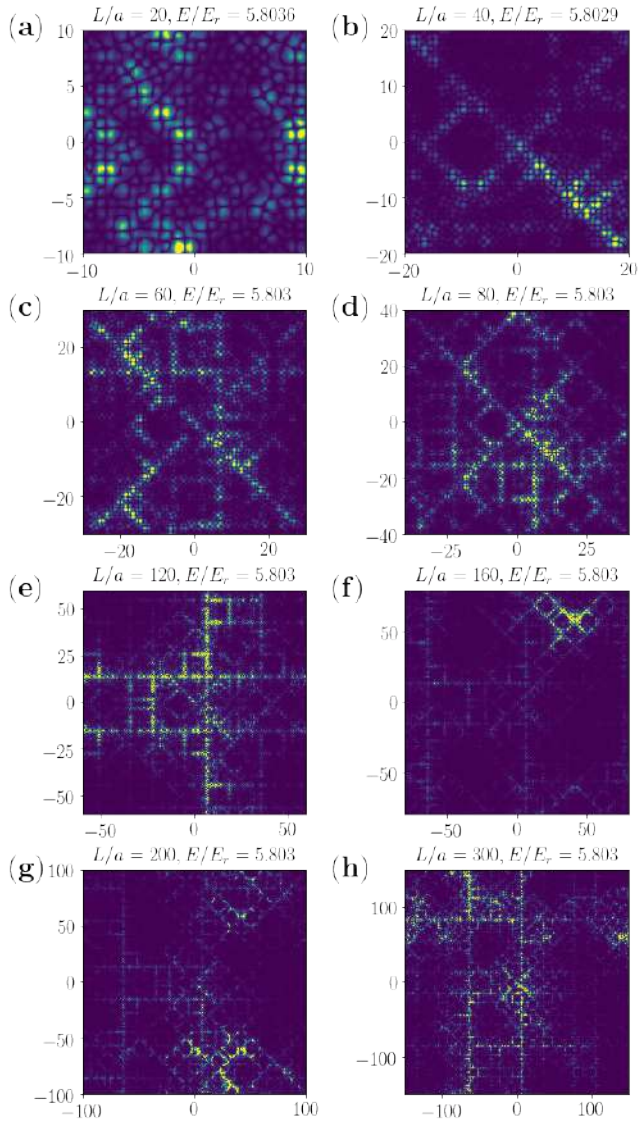


Figure 3.13: Wavefunctions in the critical regime at $E \simeq 5.803E_{\mathrm{r}}$ for $V_0 = 2.5E_{\mathrm{r}}$, shown at different scales. The various panels show the wavefunction of the state with eigenenergy closest to $E = 5.803E_{\mathrm{r}}$ for system sizes increasing in the reader order, from (a) $L = 20a$ to (h) $L = 300a$. Note that the colors have been rescaled to increase the contrast.

such ring states with node lines along the diagonals, hybridization is favored along the main axes, which maximizes the overlap of wavefunctions from adjacent rings. This explains the appearance of lines along the main axes. Moreover,

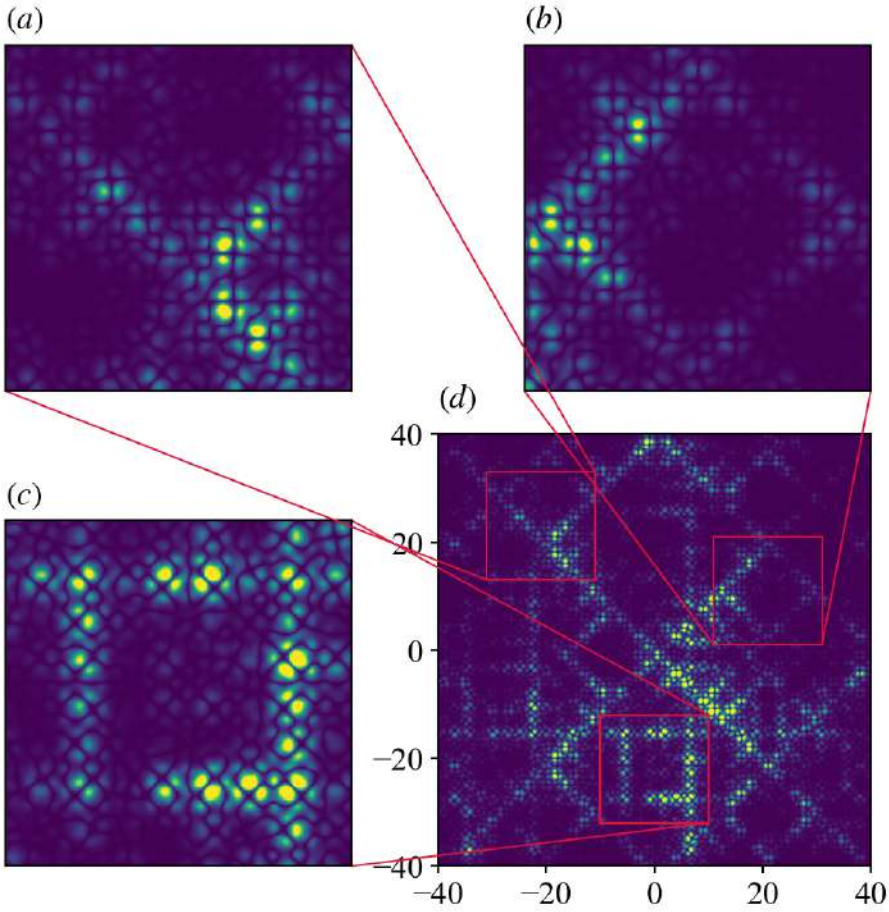


Figure 3.14: (a), (b) and (c): Zoomed up plots of several regions of the wavefunction shown in (d), which is a copy of Fig. 3.13 (d).

owing to the eightfold rotation symmetry of the potential, there are also ring states with two node lines, but now oriented along the main axes. For such states, the hybridization is then favored along the diagonals, which creates the distinct lines across the diagonals. Finally, since all the ring states with two node lines along either the main axes or along the diagonals are quasi-degenerate, square-like structures oriented in either directions also hybridize, hence forming the complex structure observed in Fig. 3.13. In support of this interpretation, zooms of the wavefunction show that the lines parallel to the main axes are formed of ring states with two node lines along the diagonals while the lines along the diagonals are formed of ring states with two node lines along the main axes, see Fig. 3.14.

Finally, in Fig. 3.15, we show two examples of critical states with energy near

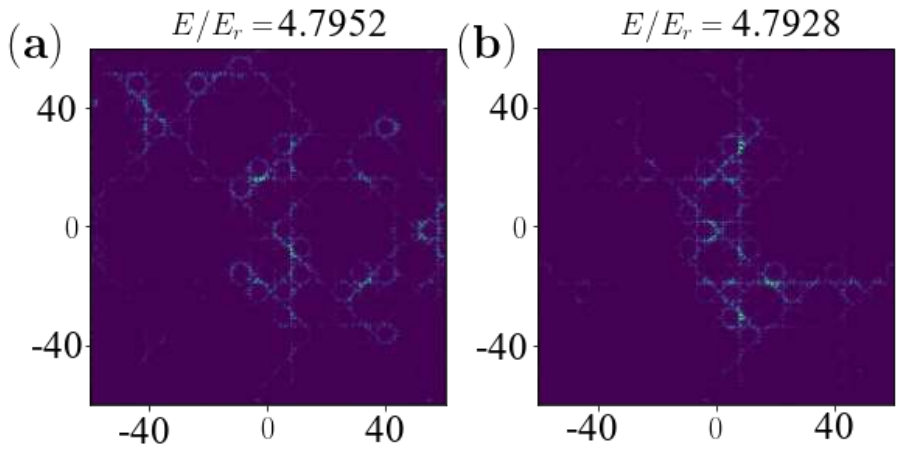


Figure 3.15: Examples of critical states with energy near $E \simeq 4.8E_{\rm r}$, which are composed of $m = 1$ ring state components (i.e. a single node line). We consider $V_0 = 2.5E_{\rm r}$ and $L/a = 100$. Localized components become coupled in circular, ring-like arrangements. These circular structures are then coupled with a square-shaped pattern.

$E \simeq 4.8E_{\rm r}$. These states are composed of hybridized ring-like structures on small scale, with a similar square-shaped pattern to what has been observed before on large scale. At the intermediate length scale, we observe circular structures composed of several ring states with a single node line each (i.e. $m = 1$ ring states). The node lines are aligned in such a way to face the centre of the circle. Different circles couple together and form extensive critical states.

## 3.6 Gaps bounded by ring states with phase winding

We now study the structure of the energy spectrum. The DOS for the quasicrystal with amplitude $V_0 = 2.5E_{\rm r}$ and a large system size, $L = 80a$, is shown in Fig. 3.16. It displays two main gaps, in the energy windows $E/E_{\rm r} \in [4.98, 5.72]$ and $E/E_{\rm r} \in [5.94, 6.44]$, respectively, as well as three smaller gaps at $E/E_{\rm r} \simeq 4.11$, $E/E_{\rm r} \simeq 4.65$, and $E/E_{\rm r} \simeq 4.71$. To understand the origin of these energy gaps, we study the properties of eigenstates in the vicinity of the band edges.

### 3.6.1 Ring states at band edges

States localized in small ring structures of the potential play an important role in the energy spectrum, as also observed in Ref. [159]. For instance, the states right before the small gap at $E \simeq 4.65E_{\rm r}$ are composed of small rings

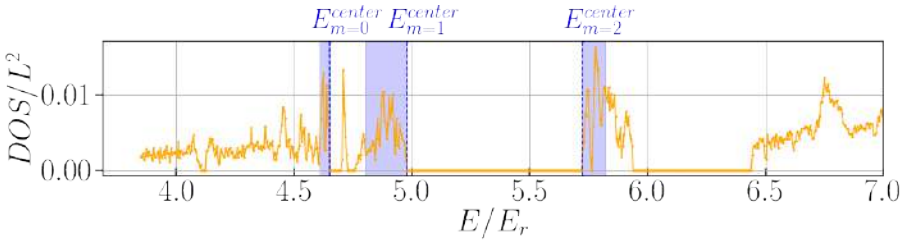


Figure 3.16: Density of states per unit area versus energy for potential amplitude $V_0 = 2.5E_\mathrm{r}$ and system size $L = 80a$. The energies of the centered small rings with winding $m = 0$, 1, and 2 are indicated by the dashed lines. The shaded areas indicate the regions of the corresponding off-centered rings with the same winding numbers.

with a roughly homogeneous density, similar to that shown in Fig. 3.10(e), and spread over different locations. The states right before the first large energy gap at $E/E_\mathrm{r} \in [4.98, 5.72]$ are similar ring states but with one node line, similar to that shown in Fig. 3.10(f). The states right after the same large gap are also ring states but with two node lines, similar to that shown in Fig. 3.10(g). The energies of ring states with 0, 1 or 2 node lines are highlighted with the shaded blue areas in Fig. 3.16.

Although we have so far excluded the symmetry center of the potential by considering off-centered systems, it is useful to re-incorporate it in the discussion of these ring states. Indeed, very regular ring states exist for the eight-fold quasicrystal potential around the symmetry center at $\mathbf{r} = 0$, see Fig. 3.17(a). Remarkably, these centered ring states have energies that exactly limit certain bands, as indicated by the vertical, dashed blue lines in Fig. 3.16. For instance, the centered ring state with no node lines, Fig. 3.17(a1), is the very last state of the energy band before the small gap at $E \simeq 4.65E_\mathrm{r}$. Then, there are two degenerate centered ring states with a single node line each, Figs. 3.17(a2) and (a3), which lie immediately before the first large gap, at $E \simeq 4.98E_\mathrm{r}$. Finally, there are another two degenerate, centered ring states with two node lines, Figs. 3.17(a4) and (a5), immediately after the first large gap, at $E \simeq 5.72E_\mathrm{r}$. The other ring states with 0, 1 or 2 node lines that are situated in rings away from the center of the quasicrystal are slightly distorted, see Figs. 3.17(b1)-(b5), and their energies lie deeper in the energy bands, as indicated by the shaded areas in Fig. 3.16. As discussed below, rejection of the off-centered ring states inside the energy bands may be interpreted as a level repulsion effect.

For the sake of completeness, note that the first state after the second large gap at $E \simeq 6.44E_\mathrm{r}$ is made of ring states with three node lines. In this case, however, many such rings are connected, hence forming a quite compact extended state. The states at the band edges of the gap at $E/E_\mathrm{r} \simeq 4.11$ are localized states, and will be briefly discussed later in Sec. 3.6.5. Finally, the states at the other band edges before $E \simeq 6.44E_\mathrm{r}$ are also localized states, without any

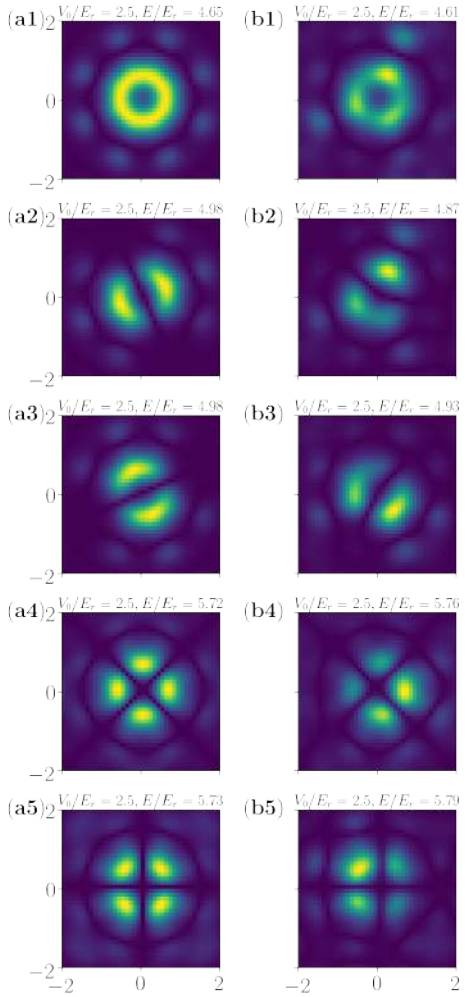


Figure 3.17: Centered (left) and off-centered (right) ring states in the eight-fold quasicrystal potential centered at $\mathbf{r}_0 = (0, 0)$, with amplitude $V_0 = 2.5E_\mathrm{r}$. (a1)-(a5) States at energy band edges: (a1) Last state before the small gap at $E/E_\mathrm{r} \simeq 4.65$; (a2) and (a3) Two almost degenerate states immediately before the first large gap in $E/E_\mathrm{r} \sim [4.98, 5.72]$; (a4) and (a5) Two almost degenerate states immediately after the same first large gap. They are eigenstates for the smallest ring around $\mathbf{r} = 0$ with winding numbers (node line numbers) $m = 0, \pm 1, \pm 2$. (b1)-(b5) Off-centered ring states around $\mathbf{r}_0 = (19.06a, 4.95a)$ obtained by diagonalization in a square with size $L = 4a$.

particular features in their patterns.

These observations indicate that the small ring states, especially the ones centered on the symmetry center of the quasicrystal potential at $\mathbf{r} = 0$, play

special roles in the structure of the spectrum, and we discuss them in more detail below.

### 3.6.2 Central ring

We first consider the ring states around the quasicrystal symmetry center at $\mathbf{r} = 0$, see Fig. 3.17(a). They are located in a nearly isotropic annular potential well of radius $\rho_0 \simeq 0.61a$. More precisely, the potential has eight very shallow potential wells along the ring, which may, however, be neglected. In particular, we find that the ring-state with no node, Fig. 3.17(a1), has a nearly isotropic density with modulations less than 10%. As a result, the small ring states in Fig. 3.17(a) may be approximated by states localized in the nearly isotropic annular potential well with almost isotropic density and $\mathrm{O}(2)$ rotational symmetry around the symmetry center $\mathbf{r} = 0$. In the vicinity of the annular well, the Hamiltonian and the planar angular momentum operator $\hat{L}_z$ can be diagonalized simultaneously, and the wavefunctions can be written as $\phi^0_m(\mathbf{r}) \simeq u_m(r)\mathrm{e}^{im\theta}$, where $u_m(r)$ is a real-valued function, $\theta$ is the polar angle, and $m \in \mathbb{Z}$ is the phase winding number.

Writing $u_m(r) = r^{-1/2} f_m(r)$, the amplitude $f_m(r)$ is then governed by the semi-infinite one-dimensional, radial equation

$$-\frac{\hbar^2}{2M}\frac{\mathrm{d}^2}{\mathrm{d}r^2} f_m(r) + V_m(r) f_m(r) = E_m f_m(r), \quad r > 0, \tag{3.9}$$

with the effective potential

$$V_m(r) = V(r) + \frac{\hbar^2}{2M}\frac{4m^2 - 1}{4r^2}. \tag{3.10}$$

The latter consists of the bare potential $V(r)$ and a centrifugal term.

A shown in Fig. 3.18, the centrifugal term strongly deforms the potential for $r \lesssim 0.1a$, but the distortion near the minimum, $r_0 \simeq 0.61a$, is weak enough that the radial eigenfunction $f_m(r)$ weakly depends on $m$ for sufficiently large $V_0$ and small $m$. For a sufficiently deep potential well, we may use a harmonic approximation and write

$$V_m(r) \simeq V_m(r_0) + \frac{1}{2} M\omega_m^2 (r - r_0)^2. \tag{3.11}$$

The dependence of $\omega_m$ on $m$ is less than 10% for $V_0 > 3E_\mathrm{r}$ and $|m| \leq 2$, and similarly, the radius of the local minimum is almost independent of $m$ in the same range of parameters. So for sufficiently strong potential amplitude $V_0$ and low winding number $m$, the functions $u_m(r)$ are strongly confined around $r = \rho_0$ and we may neglect the $m$-dependence originating from the centrifugal term.

Figure 3.17(a1) is the state with winding number $m = 0$. The states in Figs. 3.17(a2) and (a3) correspond to winding numbers $m = \pm 1$. Since the states $\phi^0_{\pm 1}(\mathbf{r})$ are strictly degenerate, any linear combination of both is also an eigenstate of the Hamiltonian. Numerical diagonalization returns real-valued wavefunctions, i.e. $\psi^0_{+1}(\mathbf{r}) \simeq \sqrt{2}u(r)\cos(\theta - \theta_1)$ and $\psi^0_{-1}(\mathbf{r}) \simeq \sqrt{2}u(r)\sin(\theta - \theta_1)$,

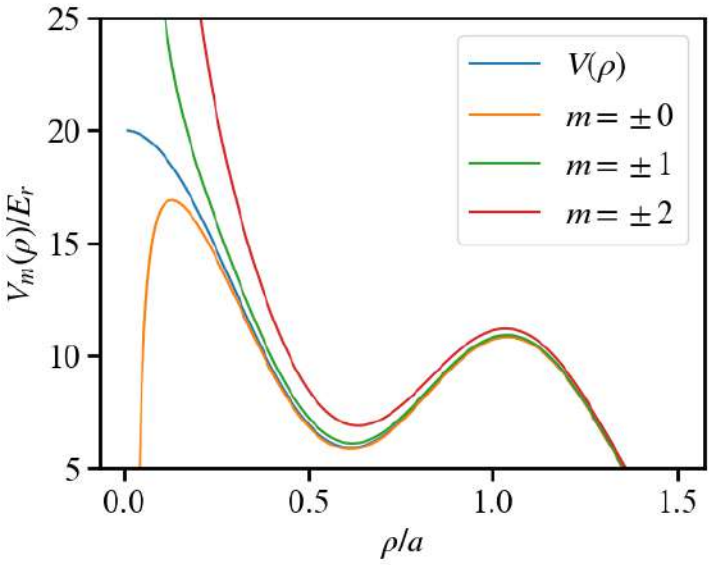


Figure 3.18: Effective potential $V_m(r)$ for a quasicrystal potential with amplitude $V_0 = 5E_\mathrm{r}$ and for varius winding numbers $m$.

where $\theta_1$ is some reference angle. Consequently, the two states in Figs. 3.17(a2) and (a3) show orthogonal node lines at the angles $\theta_1 + \pi/2$ and $\theta_1$, respectively. The angle $\theta_1$ is determined by the small modulations of potential along the annular well and, in the numerics, by the discretization, which does not satisfy an exact eight-fold rotation symmetry. Similarly, Figs. 3.17(a4) and (a5) show states with two node lines, corresponding to linear combinations of the two degenerate states with winding numbers $m = \pm 2$, $\psi^0_{+2}(\mathbf{r}) \simeq \sqrt{2}u(r)\cos(2\theta - \theta_2)$ and $\psi^0_{-2}(\mathbf{r}) \simeq \sqrt{2}u(r)\sin(2\theta - \theta_2)$, with some angle $\theta_2$.

We now check the validity and accuracy of our model. On the one hand, because of their strong localization, we can find the exact centered ring states by performing diagonalization in a small square around $\mathbf{r} = 0$ with size $L = 4a$, larger than the ring diameter $2\rho_0 \simeq 1.2a$. Figure 3.19(a) shows the eigenenergies hence obtained subtracted by the eigenenergy of the state with winding number $m = 0$ (dashed red line, zero by construction), i.e. $E_m - E_0$ for $m = \pm 1$ (dashed blue line) and $m = \pm 2$ (dashed green line). On the other hand, according to our model, the energies of the centered ring states only differ by their orbital rotation energy, which can be written as

$$E_m \simeq E_0 + \frac{\hbar^2 m^2}{2M\rho_0^2}, \tag{3.12}$$

where we have neglected the $m$-dependence of the radial Hamiltonian as well as the radial extension of $u(r)$ around the radius of the ring, $\rho_0$. The results of this prediction are shown as dashed black lines in Fig. 3.19(a), which corresponds

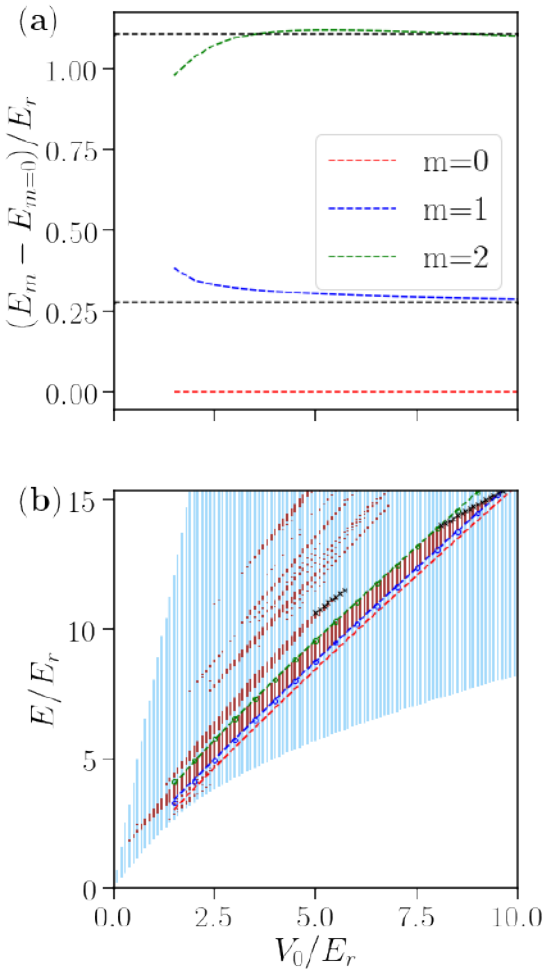


Figure 3.19: Centered ring states. (a) Energy differences $E_m - E_0$ between the ring states with winding numbers $m = \pm 1$ (blue) and $\pm 2$ (green), and the ring state with winding number $m = 0$ (red, zero by construction). The dashed black lines show the corresponding theoretical estimates, $\hbar^2\, m^2/2M\rho_0^2$, see Eq. (3.12), for $m = \pm 1$ and $m = \pm 2$. (b) Energy spectrum (reproduced from Fig. 3.5) showing bands (blue) and gaps (red). The dashed lines show the energies of the ring states $E_m$ obtained from diagonalization in a small system with size $L = 4a$ for $m = \pm 1$ (blue) and $m = \pm 2$ (green). The circles are the theoretical estimates using Eq. (3.12) with $E_0$ corresponding to the numerical value. They are almost on top of the corresponding dashed curves. The black crosses show the energies of states which enter and finally close the large gaps at large $V_0$, see discussion in Sec. 3.6.4.

to the orbital rotation energy for winding numbers $m = \pm 1$ and $m = \pm 2$, respectively. As expected, we find an increasingly better estimate of the ring states energies as the amplitude of the quasicrystal potential increases, owing to a stronger radial confinement. In addition, the energies of these ring states are also plotted on top of the full spectrum for a large system of size $L = 60a$ in Fig. 3.19(b). The full spectrum is reproduced from Fig. 3.5, with blue denoting the bands and red the gaps. The dashed lines show the energies of the ring states $E_m$ with $m = 0$ (red), $m = \pm 1$ (blue), and $m = \pm 2$ (green) as obtained from diagonalization in a small system with size $L = 4a$ and the open disks represent the corresponding theoretical estimates, Eq. (3.12). The ring state energies lie on the bands edges. This is consistent with the fact that the large gap is created by the centered, localized ring states with winding number $m = \pm 1$ and $m = \pm 2$, before it starts to close at $V \simeq 8E_{\rm r}$.

### 3.6.3 Off-centered rings

Let us now examine the off-centered ring states, which are located in annular potential wells around various positions away from the symmetry center of the quasicrystal potential. A typical example is shown in Fig. 3.17(b), which corresponds to ring states centered at $\mathbf{r}_0 = (19.06a, 4.95a)$ with 0, 1 or 2 node lines. Quasiperiodicity of the system implies that the potential around such states is similar to that around the central ring, but with distortions. The latter are weak but clearly nonnegligible, see Fig. 3.20(a). In particular, the potential and the ring states do not strictly fulfill eight-fold rotation symmetry around the local center at $\mathbf{r}_0 \neq 0$, see in particular the appearance of three deeper wells around the central ring (dashed red line). As a consequence, the corresponding ring states, Figs. 3.17(b1)-(b5), are not as symmetric as the centered ones, Figs. 3.17(a1)-(a5). Nevertheless, the off-centered ring states have nearly the same radius as the centred one, $\rho_0 \simeq 0.61a$, and can still be classified according to their winding number, or equivalently, node line number $m$. Similar properties are found around other ring states centered at different locations.

As mentioned above, we have observed that the off-centered ring states with winding number $m = 0$ or $m = \pm 1$ have lower energy than their centered counterparts. In contrast, for winding number $m = \pm 2$, the off-centered ring states have a higher energy than their centered counterparts. This phenomenon is due to level repulsion, as we show now. Owing to the similarity of the off-centered annular potential wells and ring states with their centered counterparts, we may understand the properties of the former as a perturbation of the latter. To lowest pertubation order, we write the off-centered ring states as the shifted centered one, $\phi_m(\mathbf{r}) \simeq \phi^0_m(\mathbf{r} - \mathbf{r}_0)$, and the perturbation potential as $\Delta V(\mathbf{r}) = V(\mathbf{r}) - V(\mathbf{r} - \mathbf{r}_0)$. Working in the sub-Hilbert space of these states, the perturbation matrix elements are

$$\langle \phi_{m_1} | \, \Delta V \, | \phi_{m_2} \rangle \propto \int d\theta \, \Delta V(\rho_0, \theta) \mathrm{e}^{i(m_2 - m_1)\theta}. \tag{3.13}$$

On the one hand, the left hand side of Eq. (3.13) can be calculated numerically,

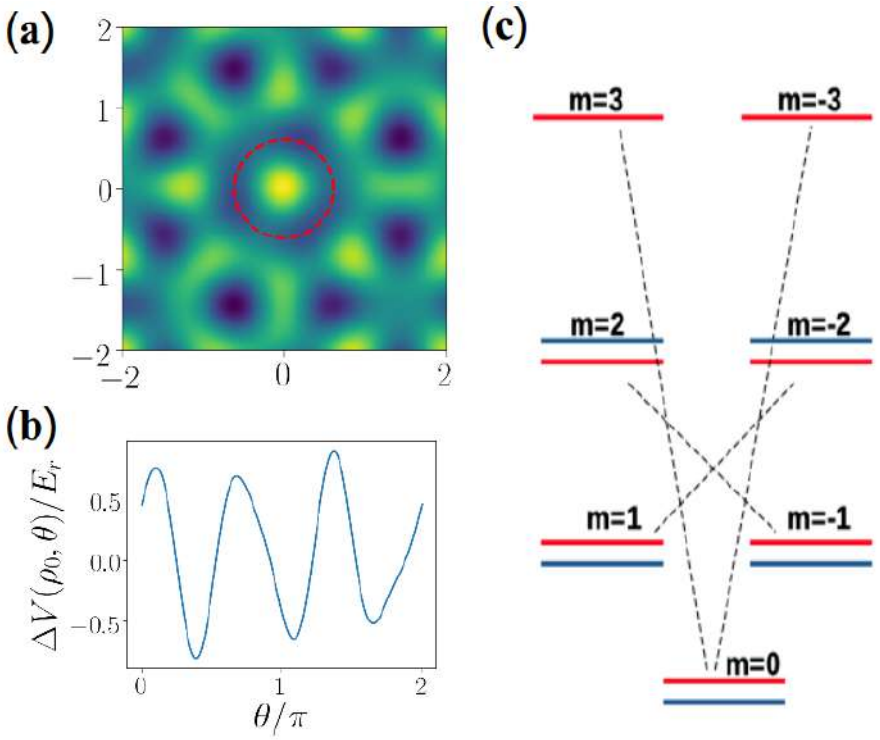


Figure 3.20: Off-centered ring states. (a) Quasicrystal potential in the vicinity of an off-centered annular potential well, centered at $\mathbf{r}_0 = (19.06a, 4.95a)$. Color scales represent the potential from low values (dark purple) to high values (light yellow). The dashed circle is the ring of radius $\rho_0 = 0.61a$ around the local maximum. (b) Perturbation potential $V(\rho_0, \theta)$ along the ring as a function of the polar angle $\theta$. (c) Sketch of the energy-level repulsion picture. The red lines represent energy levels of the centered (unperturbed) ring states with different winding numbers, and the blue lines their off-centered (perturbed) counterparts. The dash lines represent the dominant couplings.

where the required wavefunctions are reconstructed by linear combination of the real-valued numerical wavefunctions, using $\phi_m(\mathbf{r}) = [\psi_{+m}(\mathbf{r}) + i\psi_{-m}(\mathbf{r})]/\sqrt{2}$ for $m \in \mathbb{Z}$. On the other hand, the right hand side is found by neglecting the radial extension of the ring states and $\Delta V(\rho_0, \theta)$ is a shorthand notation for the perturbed potential along the ring of radius $\rho_0$ with $\theta$ the polar angle. Due to the three-period oscillation of the potential around the ring shown in Fig. 3.20(b), the Fourier integral in Eq. (3.13) shows two resonances for $m_2 - m_1 = \pm 3$, and we expect that the couplings are dominated by the processes such as $m \leftrightarrow m \pm 3$. We indeed find that the corresponding couplings are at least one order of magnitude larger than the other ones. Figure 3.21 shows, in units of $E_\mathrm{r}$, the moduli of all

| $\Delta V/E_r$ | $m=0$ | $m=+1$ | $m=-1$ | $m=-2$ | $m=+2$ | $m=-3$ | $m=+3$ |
|---|---|---|---|---|---|---|---|
| $m=0$ | 0.01082852 | 0.00425186 | 0.00425186 | 0.03266841 | 0.03266841 | 0.12117409 | 0.12117409 |
| $m=+1$ | | 0.01138857 | 0.03902952 | 0.24707624 | 0.02948781 | 0.00013442 | 0.01177908 |
| $m=-1$ | | | 0.01138857 | 0.02948781 | 0.24707624 | 0.01177908 | 0.00013442 |
| $m=-2$ | | | | 0.00954469 | 0.00070855 | 0.03857501 | 0.12243 |
| $m=+2$ | | | | | 0.00954469 | 0.12243 | 0.03857501 |
| $m=-3$ | | | | | | 0.00321993 | 0.04628118 |
| $m=+3$ | | | | | | | 0.00321993 |

Figure 3.21: Perturbation matrix of the ring states.

the perturbation matrix elements $\langle\phi_{m_1}|\,\Delta V\,|\phi_{m_2}\rangle$, see Eq. (3.13), between the 7 ring states with winding numbers $m=0$, $\pm1$, $\pm2$, and $\pm3$. The perturbation $\Delta V$ is the difference between the potentials around $\mathbf{r}_0=(19.06a, 4.95a)$ and around $\mathbf{r}=0$. Since the matrix is symmetric, only the upper half is shown. The numbers in red are the strongest couplings while those in black are at least about one order of magnitude smaller.

Since perturbation is stronger for states with closer unperturbed eigenenergies, the strong couplings between $m\leftrightarrow m\pm3$ effectively creates a 2-level system for states $|m=+1\rangle$ and $|m=-2\rangle$ on the one hand, and for states $|m=-1\rangle$ and $|m=+2\rangle$, on the other hand. The state $|m=0\rangle$ is strongly coupled to both states $|m=3\rangle$ and $|m=-3\rangle$, hence forming a three-level system. The overall effective system is sketched in Fig. 3.20(c). Energy level repulsion in the 2-level systems shifts down the energies of the states with winding number $m=\pm1$ and up the energies of the states with winding number $m=\pm2$. Note that the diagonal perturbation terms, $\langle\phi_m|\,\Delta V\,|\phi_m\rangle$ are negligible. The couplings between state $|m=0\rangle$ and states $|m=3\rangle$ and $|m=-3\rangle$ shifts down the energy of $|m=0\rangle$, since off-diagonal perturbations always yields negative corrections to the ground-state energy.

As a result, the energies for the off-centered ring states with windings $m=0,\pm1,\pm2$ are shifted in specific directions, which is in agreement with our numerical diagonalization. As the largest energy gap corresponds to that between ring states with winding numbers $m=\pm1$ on the one hand and $m=\pm2$ on the other hand, we have shown that the bottom of this gap is bounded by the winding $m\pm1$ ring states at center $\mathbf{r}=0$. Likewise, the top of this gap is bounded by the winding $m=\pm2$ ring states at center $\mathbf{r}=0$. This persists in the thermodynamic limit, and the gap width is just the energy difference between these centered ring states.

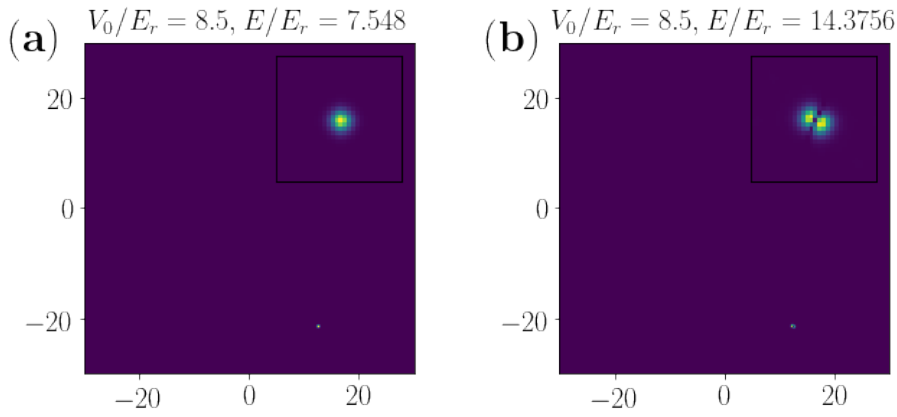


Figure 3.22: (a) Ground state of the system alongside (b) the first state after the first large energy gap, corresponding to the two red triangles in Fig. 3.19(b). The system size is $L = 60a$ and the potential amplitude is $V_0 = 8.5E_\mathrm{r}$. The insets show magnifications of the strongly localized states.

### 3.6.4 Closing of gaps

Our model relates the large gaps to ring states with different winding numbers. According to Eq. (3.12), valid for strong radial confinement, the gap widths may thus be expected to reach a constant value for large enough potential depth $V_0$, see also Fig. 3.19(a). Consistently, we indeed observe that the blue and green dashed lines in Fig. 3.19(b), which show the energies of the centered ring states with winding numbers $m = \pm 1$ and $m = \pm 2$, respectively, are almost parallel to each other. They match the boundaries of the largest gap, shown in red, for a significant energy range, for $2 \lesssim V_0/E_\mathrm{r} \lesssim 8.1$. However, this gap, as well as the next one right above, close progressively, respectively in the ranges $8.1E_\mathrm{r} \lesssim V_0 \lesssim 9.6E_\mathrm{r}$ and $5E_\mathrm{r} \lesssim V_0 \lesssim 5.7E_\mathrm{r}$, see the black crosses in Fig. 3.19(b), which indicate the upper limit of the gaps in these regions. In fact, the closing of both these gaps is due to another kind of strongly-localized states. For weak potential amplitude $V_0$, these strongly-localized states have an energy well inside a energy band above the second gap, but when $V_0$ increases, they enter successively each gap between the ring states and create the new upper limit of the gaps. The state closing the largest gap for $V_0 = 8.5E_r$ [upper red triangle in Fig. 3.19(b)] is shown in Fig. 3.22(b) and, for comparison, the ground state of the system [lower red triangle in Fig. 3.19(b)] is shown in Fig. 3.22(a). Both these states turn out to be strongly localized in the same deep potential well, and correspond to the ground state and the first excited state of this well. More precisely, we may approximate the deep potential well by a harmonic potential. The state in Figure 3.22(a) is then the ground state of the trap, while the state in Figure 3.22(b) is the first excited state of the same trap. Consistently with this interpretation, we note that the local minimum of the trap has a vanish-

ingly small potential energy and the energy of the excited state in Fig. 3.22(b) is about twice that of the state in Fig. 3.22(a), see values on top of the figures. This is what is expected for a 2D isotropic harmonic trap. The discrepancy to exact energy doubling (about 5%) may be attributed to slight anisotropy and/or anharmonicity of the trap. Such kind of deep potential wells spread over the system and similar states as in Figure 3.22 located around these potential wells are found with similar energies. As the potential amplitude increases, the first excited states of such deep potential wells, similar to Fig. 3.22(b), enter the higher large gap at about $V_0 \simeq 5E_\mathrm{r}$ and comletely close it at about $V_0 \simeq 5.7E_\mathrm{r}$. Then, as the potential amplitude further increases, those states enter the lower large gap at about $V_0 \simeq 8.1E_\mathrm{r}$ and close it at about $V_0 \simeq 9.6E_\mathrm{r}$, see black crosses in Fig. 3.19(b).

A similar phenomenon explains why we do not observe gaps at a higher energy. In principle, Eq. (3.12) suggests even larger gaps at higher energies. However, we find that various kinds of states other than the ring states appear inside the gaps induced by the sole ring states and the latter are not visible. Moreover, these different kinds of states hybridize at high energy and the structure of the spectrum is not governed by clear ring states any more.

### 3.6.5 Self-similarity and minigaps

The spectrum in Fig. 3.5 presents self-similar structures. Figure 3.23(a) shows a zoom of the latter around $V_0 = 2E_\mathrm{r}$ and $E = 3.5E_\mathrm{r}$. It clearly shows several gaps, the lowest two for instance around energy $E \simeq 3.4E_\mathrm{r}$ for $V_0 = 1.9E_\mathrm{r}$, and different energy for different $V_0$. Although these gaps are almost invisible on Figs. 3.5 and 3.19(b), we have checked that they are legitimate gaps, according to the procedure presented in Sec. 3.4.

To identity the nature of these gaps, the states at their edges are plotted in Figs. 3.23(b)-(e). Figure 3.23(b) shows the state at the bottom edge of the first gap. It is a state localized around the quasicrystal center $\mathbf{r} = 0$ and it is composed of eight spots corresponding to eight local potential wells. The latter are identical to each other due to exact eightfold rotational symmetry around $\mathbf{r} = 0$. They lie on a ring larger than the small ring discussed above [shown for reference as a dash red circle in Figs. 3.23(b), (c), and (e)]. The states localized on this larger ring can still be classified according to their winding numbers or equivalently node line numbers. The state in Fig. 3.23(b) shows one clear node line and it has thus winding number $m = \pm 1$. Similarly Fig. 3.23(c) shows the state with winding number $m = \pm 2$, which lies near the top of the first gap, and the state at the top of the second gap shown in Fig. 3.23(e) that with winding number $m = \pm 3$. Note that the state of Fig. 3.23(c) is not strictly at the top of the first gap. The state at the very top edge of the first gap is composed of four off-centered copies of Fig. 3.23(c) connected together and has a slightly lower energy than the centered state shown in Fig. 3.23(c). The state at the bottom edge of the second gap shown in Fig. 3.23(d) is not localized at $\mathbf{r} = 0$ and has no clear special structure.

The general picture of these small gaps is thus similar to that of the large

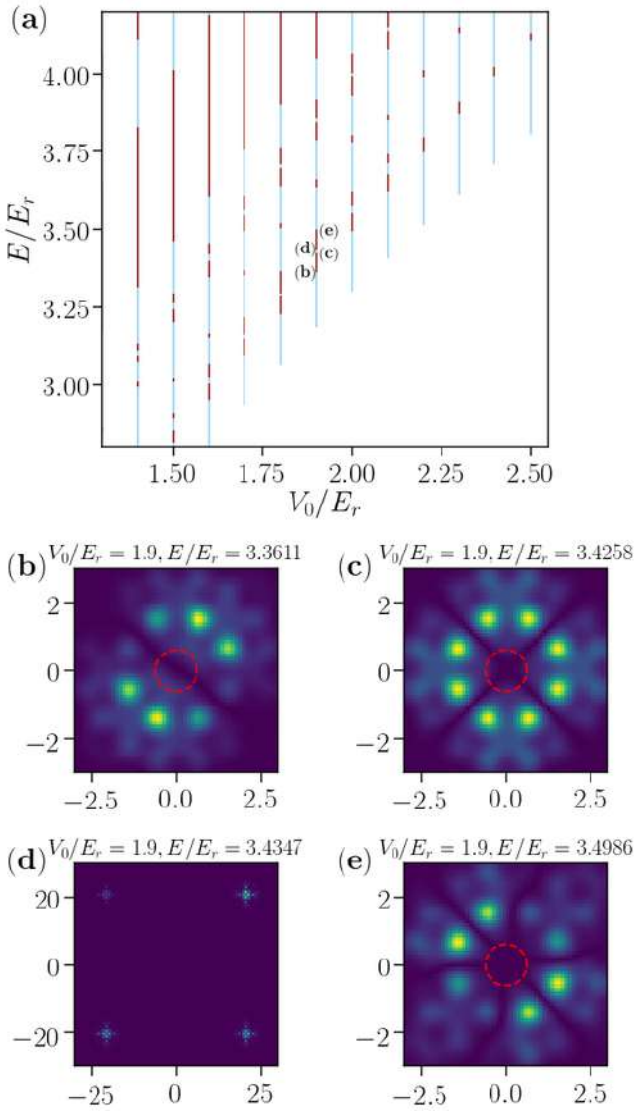


Figure 3.23: (a) Zoomed spectrum of the eight-fold quasicrystal potential for various amplitudes $V_0$. Bands are colored blue and gaps are red. (b)-(e) Eigenstates at band edges for the two gaps with energy around $E = 3.4E_\mathrm{r}$ for $V_0 = 1.9E_\mathrm{r}$. (b), (c) Bottom and top states of the first gap. (d), (e) Bottom and top states of the second gap.

gaps discussed above created by the small ring states with different winding numbers. The only difference is that the ring states creating the small gaps have a larger ring radius, so that the energy differences due to phase windings

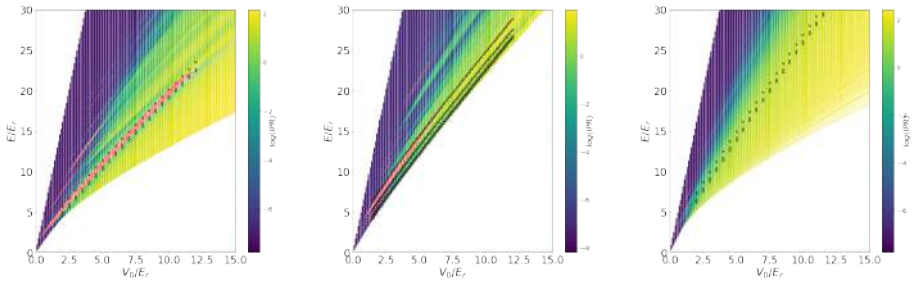

Figure 3.24: Energy spectra of quasicrystal potentials with different rotational symmetries as created by $n$ pairs of counterpropagating laser beams, with $n = 5$ (left, ten-fold), $n = 6$ (middlet, twelve-fold), and $n = 7$ (right, fourteen-fold). The system size is $L = 60a$, centered at $x = -13543a, y = 196419a$. The color scale represents the value of log(IPR) of each eigenstate, while the gaps are all colored red. The energies of the first few centered ring states are shown as black crosses.

are much smaller, and the gap sizes are comparatively much smaller than the gaps created by the small rings.

## 3.7 Quasicrystal potentials with different rotational symmetries

So far, we have considered the localization and spectral properties of a quasicrystal potential with eightfold rotational symmetry. Here we briefly discuss whether or not quasicrystals with different rotational symmetries may also possess similar properties. To answer this, we study quasicrystal potentials that are generated by interfering a larger number $n$ of laser beams. The general formula of a quasicrystal potential with a $2n$-fold rotational symmetry is

$$V(\mathbf{r}) = V_0 \sum_{k=1}^{n} \cos^2\left(\mathbf{G}_k \cdot \mathbf{r} + \phi_k\right), \tag{3.14}$$

with $\mathbf{G}_k = \frac{\pi}{a}\big(\cos(k\pi/n), \sin(k\pi/n)\big)$. Realization of such potentials have been recently proposed in Ref. [163]. In Fig. 3.24, we plot the energy spectra for $n = 5$, 6, and 7. The general localization picture is similar to that previously discussed for the eightfold quasicrystal potential ($n = 4$): For sufficiently large amplitude $V_0$, the eigenstates are typically localized at low energy and extended at high energy. At intermediate energy, we find a nonmonotonous energy-dependence of the localization strength. Moreover, for $n = 5$ or $n = 6$, the spectrum also has at least one large gap, similar to that found for $n = 4$, as well as smaller but visible gaps. For $n = 7$ instead, the gaps become much narrower and almost invisible at the scale of Fig. 3.24. To understand the origin of these gaps, we

note that the quasicrystal potentials created by more than 4 laser pairs also have an annular potential well around the center at $\mathbf{r} = 0$, with almost the same radius, $\rho_0 \simeq 0.61a$. As a result, this annular potential well also hosts ring states with different winding numbers, the energies of which are still approximately given by Eq. (3.12). The energy differences are thus almost the same as for $n = 4$, but the reference energy $E_0$ may be dependent on $n$. Moreover, they are almost independent of the potential amplitude for large enough $V_0$. The energies of the first few centered ring states for each quasicrystal potential are plotted as black crosses in Fig. 3.24.

For $n = 5$, the structure of the spectrum is very similar to that discussed above for $n = 4$. In particular, the largest gap is also created by the gap between the ring states with winding numbers $m = \pm 1$ and $m = \pm 2$, and the gap width is almost the same as for $n = 4$. For $n = 6$, the largest gap may also be related to ring states, now with winding numbers $m = \pm 2$ and $m = \pm 3$, and the gap size is larger. More precisely, the top of the gap is indeed composed of centered ring states with winding number $m = \pm 3$. In contrast, the bottom of the gap is not strictly a centered ring state with winding number $m = \pm 2$, since off-centered ring states with the same winding number have higher energies than the centered one, as discussed above. For a limited range of quasicrystal amplitude, $2E_\mathrm{r} \lesssim V_0 \lesssim 4E_\mathrm{r}$, the centered and off-centered ring states with $m = \pm 2$ lie near by the band edge, but the true edge state turns out to be a different state, which can be either localized or extended with a complex structure, depending on $V_0$. For $V_0 \gtrsim 4E_r$, new localized states enter the bottom of the gap, and progressively closes it from below. Note also that for a certain range of $V_0$, roughly between $2E_\mathrm{r}$ and $7E_\mathrm{r}$, the ground state of the whole spectrum is the centered ring state with winding number $m = 0$. Finally, we find that for $n = 7$ the gaps have almost negligible sizes, and there is no large gap near the energies of the ring states. This is because other kinds of states coexist with those ring states in the same eigenenergy ranges, even though ring states still have the same energy differences for different winding numbers. For larger $n$, we found that large gaps generated by ring states remain closed.

## 3.8 Conclusion

In summary, we have shown that 2D optical quasicrystals host exotic localization properties and intriguing spectral features. For the eight-fold rotationally symmetric potential, a finite-size scaling analysis of the IPR reveals the presence of localized, critical, and extended states. Extended states dominate the energy spectrum at large energies, as expected. Similarly, localized states populate the low energy spectrum. However, at intermediate energies, we find that localized states can appear alongside critical states, with no clear separation between them. Furthermore, large gaps appear in the spectrum, with some states at the band edges having a strongly localized profile. These localized states can take the form of ring states with different quantized winding numbers. By modelling these ring states, we have found that the band edges

coincide with the theoretical energy of ring states, thus confirming that they play an important role in the formation of energy gaps within optical quasicrystals. Finally, we have also confirmed that quasicrystals with other rotational symmetries can also possess similar kinds of localization properties and energy spectra, with ring states again playing an important role. In all cases, the most prominent gaps of the spectra are stable across a range of potential depths $V_0$ and rotational symmetries, provided that other localized states do not compete or enter the gap generated by the ring states. Our results shed new light on localization and spectral properties of optical quasicrystal potentials, as realized in recent experiments [47, 49, 158, 163]. Further application and development of this work may be expected in two directions.

On the one hand, our results are directly applicable to the above-mentioned experiments. The eightfold quasicrystal potential studied in the main part of the paper has been implemented in the experiments reported in Refs. [47, 49, 158] and potentials with higher order discrete rotation symmetry can be implemented in a similar manner by using a suitable number of laser beams, see for instance Refs. [46, 163]. The quasicrystal potential amplitudes considered here, $V_0 \simeq 1 - 15E_\mathrm{r}$, are also relevant for these experiments and inter-atomic interactions can be cancelled with high accuracy using Feshbach resonance methods [95, 164]. Localization may be unveiled in ultracold atomic gases using expansion schemes, as proposed in Refs. [46, 119] and realized for instance in Refs. [20, 118, 165, 166], see also Refs. [167–171] for further theoretical discussions. In this scheme, an initially trapped ultracold-atom gas is released into the quasicrystal potential, generating a wavepacket covering a tunable range of energy components. The components whose energy corresponds to a band of localized states stop expanding on a short length scale, while those whose energy corresponds to a band of extended states show normal diffusive expansion. Direct imaging at different times can thus be used to distinguish between them. For the 2D quasicrystal lattice considered here, bands of critical states also exist, for which we can anticipate anomalous diffusion, also observable in the expansion dynamics. In such schemes, a cut-off energy can be set using the chemical potential of an initially interacting Bose-Einstein condensate or the Fermi energy of an ultracold gas of fermions. When controlled by the initial interaction strength and/or the number of atoms, we expect to observe a localized gas at low chemical potential, anomalous diffusion on top of a localized component at intermediate chemical potential, and an additional normal diffusion when the spectral range contains extended states. Note, however, the coexistence of localized, critical, and extended components may make their segregation difficult. To overcome this issue, fine selection of a particular energy can also be achieved using radio-frequency transfer from an internal atomic state insensitive to the quasicrystal potential towards a sensitive state [172]. Here, the width of the selected energy range is proportional to the inverse of the pulse duration and can be chosen from a band of either localized, critical or extended states. Expansion then leads, respectively, to pure localization, anomalous diffusion or normal diffusion. The non-transferred part undergoes ballistic expansion or can even be eliminated by transfer to a non-imaged internal atomic state. This makes it pos-

sible to reconstruct bands of localized, critical, and extended states, as shown in Fig. 3.9. The existence of the gaps discussed here can also be demonstrated by this approach.

On the other hand, our results on localization and spectral properties of the single-particle problem studied here also play an important role in the physics of correlated quantum gases in a 2D quasicrystalline potential. This is particularly the case for a gas of correlated bosons. In one dimension and in the regime of strong interactions, a gas of bosons can be exactly mapped onto a gas of free fermions, a phenomenon known as fermionization. This makes it possible to map Mott insulators onto free spectral gaps and Bose glass onto localized states. In dimensions higher than one such exact mapping breaks down, but fermionization persists nonetheless when the Bose gas populates only states that are spatially separated from one another. In this case, strong repulsive interactions suppress multiple occupation of each localized state, hence mimicking an effective Pauli principle in real space. Our results could thus help understand the onset of a Bose glass as well as a Mott plateau in the strongly-interacting regime, found in recent work [157].

# Chapter 4

# Thermodynamic Phase Diagram

As we have discussed in chapter 2, interacting bosons in a periodic lattice may be in the superfluid (SF) or Mott insulator (MI) phases. In the presence of additional disorder, the bosons may then fall into a localization phase called Bose glass (BG), which is an emblematic compressible insulator, characteristic of disordered or quasi-disordered systems and distinct from the superfluid (SF) and Mott insulator (MI) phases. In bosonic models, however, thermal fluctuations compete with (quasi-)disorder, which has so far hindered the observation of the BG phase [34, 35]. It has been recently proposed that this issue may be overcome by scaling up characteristic energies using shallow quasiperiodic potentials [38]. Before our work, this has been investigated only in 1D [39] and 2D harmonically trapped [173] systems. In contrast, the case of a 2D Bose gas with genuine long-range quasicrystal order remains unexplored. Moreover, the central issue of discriminating the BG phase from trivial thermal phases has been hardly addressed. As argued below, this cannot be achieved similarly as in 1D [35, 39] due to the special nature in 2D, and requires specific analysis.

In this chapter, we discuss the behaviour of weakly to strongly interacting 2D Bose gases in a shallow quasicrystal potential and in particular discuss the thermodynamic phase diagrams at finite temperatures. Quantum Monte Carlo simulations are performed in quasicrystal, homogeneous potentials and finite-size effects are carefully taken into account. The SF, MI, and BG quantum phases, induced by the competition of interactions and quasicrystal potential, are systematically discriminated from the normal fluid (NF), which is instead dominated by thermal fluctuations. Most importantly, we find that the BG phase survives up to significantly high temperatures. Our results in the strongly-interacting regime are interpreted using a fermionization picture and implications to experiments in ultracold atom systems are discussed.

## 4.1 The model

The dynamics of the 2D Bose gas is governed by the Hamiltonian

$$\begin{aligned}\hat{H} &= \int d\mathbf{r}\, \Psi(\mathbf{r})^\dagger \left[\frac{-\hbar^2\nabla^2}{2m} + V(\mathbf{r})\right] \Psi(\mathbf{r}), \\ &\quad + \frac{1}{2}\int d\mathbf{r}\, d\mathbf{r}'\, \Psi(\mathbf{r})^\dagger \Psi(\mathbf{r}')^\dagger U(\mathbf{r}-\mathbf{r}')\Psi(\mathbf{r}')\Psi(\mathbf{r}),\end{aligned} \tag{4.1}$$

where $m$ is the particle mass and $\Psi(\mathbf{r})$ is the bosonic field operator at position $\mathbf{r}$, obeying the commutation relation

$$[\Psi(\mathbf{r}), \Psi(\mathbf{r}')] = \delta(\mathbf{r}-\mathbf{r}'). \tag{4.2}$$

The quasicrystal potential,

$$V(\mathbf{r}) = V_0 \sum_{k=1}^{4} \cos^2\left(\mathbf{G}_k \cdot \mathbf{r}\right), \tag{4.3}$$

is the sum of four standing waves with amplitude $V_0$ and lattice period $a = \pi/|\mathbf{G}_k|$, and successively rotated by an angle of 45°, giving a quasicrystal potential with an eightfold discrete rotational symmetry. This is the same potential that has been studied in chapter 3, where we focus on the single particle properties. Here instead, we study the interacting bosons in this potential. The bosons interact via the two-body scattering potential $U(\mathbf{r}-\mathbf{r}')$. As introduced in chapter 1, at low energy, the collisions are dominated by s-wave scattering and hence fully characterized by the sole 2D scattering length $a_{2\mathrm{D}}$. Due to the logarithmic scaling of the interaction strength versus the scattering length in 2D [174–176], it is convenient to use the interaction parameter

$$\tilde{g}_0 = \frac{2\pi}{\ln(a/a_{2\mathrm{D}})}. \tag{4.4}$$

The model considered here is similar to that recently emulated in ultracold-atom quantum simulators in Refs. [47, 49]. The typical potential amplitude $V_0$ ranges from zero to a few tens of recoil energies, $E_\mathrm{r} = \pi^2\hbar^2/2ma^2$. In the eightfold quasicrystal potential (4.3), the critical amplitude for single-particle localization is $V_0 \simeq 1.76E_\mathrm{r}$ [52]. So far, ultracold bosons in such 2D quasicrystal potential have been studied for vanishing or weak interactions, up to $\tilde{g}_0 \simeq 0.86$ [49]. However, significantly higher values can be realized using transverse confinement or Feshbach resonances, up to the strongly-interacting regime, where $\tilde{g}_0 \sim 1-5$ [177]. The typical temperature in ultracold atom experiments is $k_\mathrm{B}T/E_\mathrm{r} \sim 0.01-0.5$ with $k_\mathrm{B}$ the Boltzmann constant.

## 4.2 Mean field zero temperature phase diagram

In this section we review some previous results of this model [52], which serves as a starting point for further more elaborated studies.

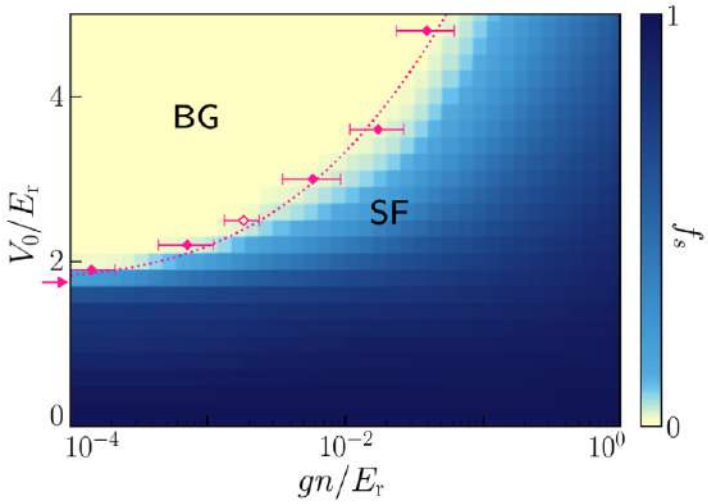


Figure 4.1: Phase diagram of the weakly interacting Bose gas in a 2D quasicrystal lattice. The y axis is the quasicrystal potential amplitude and the x axis is the interaction strength $g$ times the particle number density $n$, scaled by recoil energy $E_r$. The mean field superfluid fraction $f_s$ is shown in color scale for a system of linear size $L = 20a$. It exhibits a Bose glass phase ($f_s = 0$, yellow) and a superfluid phase ($f_s > 0$, blue), separated by a narrow intermediate region. The exact critical line is found from quantum Monte Carlo calculations at $\tilde{g}_0 = 0.03$ (pink points; the dotted line is a guide to the eye). The pink arrow indicated the single-particle critical point $V_c \simeq 1.76E_r$. This figure is from Ref. [52].

A zero temperature phase diagram for weakly-interacting bosons can be obtained with a relatively simpler method, namely a mean-field calculation [52]. The result is helpful to grasp the general picture of the localization of bosons in the quasicrystal potential. In the regime of weak interaction, the authors of ref. [52] gave the phase diagram, resulting from the competition of localization and interactions. While the quasicrystal potential tends to localize the bosons and favor a Bose glass phase with a superfluid fraction $f_s = 0$, the repulsive interactions tend to delocalize the bosons and restore superfluidity with a nonzero superfluid fraction $f_s$. The sole superfluid fraction $f_s$ can thus serve as an order parameter.

As introduced in chapter 2, using a mean field approach for the weakly interacting Bose gas, the ground state dynamics is governed by the Gross-Pitaevskii equation

$$\mu\psi = -\hbar^2\nabla^2\psi/2m + V(\mathbf{r})\psi + gN|\psi|^2\psi, \tag{4.5}$$

where $\psi(\mathbf{r})$ is normalized as $\int d\mathbf{r}|\psi(\mathbf{r})|^2 = 1$. $V(\mathbf{r})$ represents the quasicrystal potential. A dimensionful coupling constant, characterizing the interaction strength, is denoted as $g = (\hbar^2/2m)\tilde{g}$. Within the Gross-Pitaevskii approxima-

tion, the mean field phase diagram is determined by only two universal dimensionless parameters: the potential amplitude $V_0/E_r$ and the coupling coefficient $gn/E_r$. The authors calculated the field $\psi(\mathbf{r})$ by solving the equation (4.5). It gives the total energy $E$ and the chemical potential $\mu$. As discussed in chapter 2, the superfluid fraction can be calculated by using the twisted boundary condition method. The authors applied this method to get the superfluid fraction as

$$f_s = \frac{2m}{\hbar^2 n} \lim_{\theta \to 0} \frac{E_\theta - E_0}{\theta^2} \tag{4.6}$$

where $E_\theta$ is the energy with a phase difference $\theta$ at opposite sides of the system.

The phase diagram for the weakly interacting Bose gas against $V_0/E_r$ and $gn/E_r$ is shown in Fig. 4.1. The color codes refer to the value of superfluid fraction, from $f_s = 1$ (dark blue) to $f_s = 0$ (light yellow). We see that there is a region where superfluidity vanishes, for low interactions and/or a strong quasicrystal potential. This is the Bose glass phase. We know that in a homogeneous system, weakly interacting bosons at zero temperature is always in the superfluid phase. The appearance of the BG phase is due to the localization effect of the quasicrystal potential. Indeed, at low interaction limit $gn \to 0$, the onset point of the BG phase agrees with the critical potential $V_c \simeq 1.76E_r$ of single particle localization, indicated by the pink arrow on Fig. 4.1. As the repulsive interaction increased, the bosons tend to be more delocalized and a stronger quasicrystal potential is needed to enter the localization phase. As mean field approximation does not work well in the critical region, the authors also did quantum Monte Carlo calculations to locate the transitions more accurately. The data show sharp transitions between the two phases, indicated by the red points in Fig. 4.1.

## 4.3 Thermodynamic phase diagrams

### 4.3.1 Phase diagrams and order parameters

We now turn to the discussions for stronger interactions and finite temperatures. Figure 4.2 shows the thermodynamic phase diagrams of the interacting Bose gas in a quasicrystal potential of amplitude $V_0 = 2.5E_\mathrm{r}$ (above the critical localization potential) for three values of the interaction parameter $\tilde{g}_0$, ranging from weak to strong interactions. The numerical calculations are performed using path-integral quantum Monte Carlo (QMC) simulations within the grand-canonical ensemble at temperature $T$ and chemical potential $\mu$. Details about the analysis of the numerical results, in particular as regards finite-size effects, appear below. In brief, we compute the compressibility $\kappa = L^{-2}\partial N/\partial\mu$, where $N$ is the average particle number and $L$ the system's linear size, as well as the superfluid fraction $f_\mathrm{s}$, found using the winding number estimator with periodic boundary conditions [143]. These two quantities are sufficient to identify the expected zero-temperature quantum phases: SF ($\kappa \neq 0$ and $f_\mathrm{s} \neq 0$), BG ($\kappa \neq 0$ and $f_\mathrm{s} = 0$), and MI ($\kappa = 0$ and $f_\mathrm{s} = 0$). For high enough temperatures, however, one may expect a NF regime, dominated by thermal fluctuations. It is

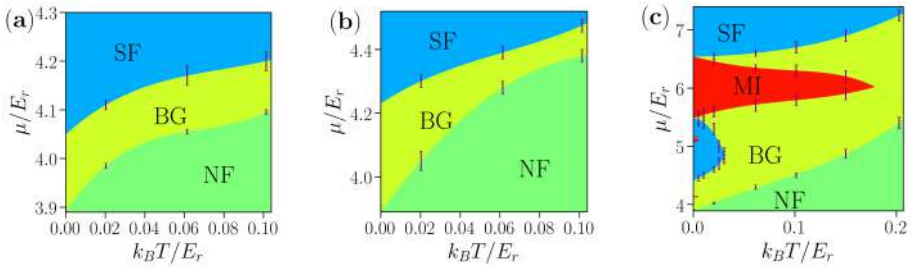


Figure 4.2: Thermodynamic phase diagrams of 2D bosons in the eightfold quasicrystal potential of Eq. (4.3) with amplitude $V_0 = 2.5E_\mathrm{r}$ and different interaction strengths, (a) $\tilde{g}_0 = 0.05$, (b) $\tilde{g}_0 = 0.86$, and (c) $\tilde{g}_0 = 5$. The quantum phases, SF (blue), BG (yellow), and MI (red), are distinguished from the NF regime (green). Note the small MI lobes in panel (c) at $\mu \simeq 4.1E_\mathrm{r}$ and $\mu \simeq 5.1E_\mathrm{r}$, which survive only at very low temperatures. QMC results are shown as data points with errorbars, while color boundaries are guides to the eye.

characterized by a finite compressibility and absence of superfluidity ($\kappa \neq 0$ and $f_\mathrm{s} = 0$), just as the BG phase.

### 4.3.2 Strategy to locate the NF-BG transition

To discriminate a genuine BG against a trivial NF, we use the criterion that phase coherence and superfluidity must be destroyed by quasi-disorder and not thermal fluctuations [53, 122]. In 1D, any finite temperature destroys superfluidity so that the BG phase is strictly well defined only at zero temperature. In practice, it is thus sufficient to identify a NF by the onset of a sizable temperature dependence of characteristic quantities, as done in Refs. [34, 35, 39]. In dimensions higher than one, however, quantum phases can survive at finite temperature while showing a significant temperature dependence of the characteristic quantities, and the above criterion breaks down. To discriminate the BG from the NF in the 2D Bose gas, we thus proceed differently and systematically compare the obtained phases in the presence of the quasicrystal potential with those of the homogeneous gas for the same temperature and the same average number of particles: If the gas is a SF in the absence of the quasicrystal potential, we identify a BG phase as soon as the quasicrystal potential amplitude is sufficient to destroy superfluidity; Otherwise, we have a NF.

As a result, the BG-NF transition point (with chemical potential $\mu_c$) has a particle number density $n$ equal to the critical particle number density $n_c^{BKT}$ at the BKT transition of 2D bosons in homogeneous system. Since both particle number density $n$ and superfluid fraction $f_s$ are monotonous functions of chemical potential $\mu$ in a quasicrystal system and homogeneous system, it can be deducted that the thermodynamic states with chemical potential $\mu < \mu_c$ are

all in NF phase, while the states with $\mu > \mu_c$ are all in BG phase(if not SF or MI).

## 4.4 Bosons in homogeneous system

With the motivation of differentiating the Bose glass phase from the normal fluid phase, we first discuss the behaviour of 2D bosons in the homogeneous system, i.e. the external potential is identically zero $V(\mathbf{r}) = 0$. As discussed in chapter2, interacting 2D bosons show the BKT transition. We performed quantum Monte Carlo simulations to locate this transition point and calculate the equation of state around the critical region.

### 4.4.1 Weak interaction

As introduced in chapter2, the BKT transition is characterised by different behaviour of the one-body correlation function

$$g(r) =< \psi^\dagger(r_0 + r)\psi(r_0) > \tag{4.7}$$

in different phases. In the superfluid phase, the function $g(r)$ has a power law dependence over the distance $r$, while in the normal fluid phase, it displays an exponential decay. If we denote the power law scaling of $g(r)$ as $g(r) \sim r^{-\eta}$, then the susceptibility $\chi = \frac{1}{L^2}\int drdr' < \psi^\dagger(r)\psi(r') >$ for a system with linear size $L$ has its corresponding scaling $\chi \sim L^{2-\eta}$. In particular, at the BKT transition critical point, $\eta = 1/4$, so the rescaled susceptibility $\chi/L^{7/4}$ will have a single crossing point for the curves of different system sizes. This correlation function $g(r)$ can be calculated by the quantum Monte Carlo method. Note that there is an unfixed normalization factor for the QMC result of $g(r)$, but this does not affect the scaling behaviour, and in particular its does not affect the crossing point of the rescaled susceptibility $\chi/L^{7/4}$. The QMC result of correlations is shown in Fig. 4.3. It displays the correlation function $g(r)$ for weakly interacting bosons with $\tilde{g}_0 = 0.05$ and temperature $T = 0.1E_r$ in a homogeneous system with linear size $L = 20a$. The left column shows the data for a chemical potential $\mu = -0.005E_r$ in the normal fluid phase while the right column is for chemical potential $\mu = 0.016E_r$ in the superfluid phase. The value of the correlation function $g(r)$ is plotted in logarithm scale. The distance $r$ is plotted in linear scale for the upper row and plotted in logarithm scale in the lower row. In spite of some fluctuation of the data, the general scaling behaviour can be discerned from the data. In the normal fluid phase, it has a linear relation in semi-log scale, so the correlation has an exponential decay. In the superfluid phase, we see in Fig. 4.3 (b) that it is not linear in the semi-log scale, but the curve has a linear trend when both $g(r)$ and $r$ are plotted in logarithm scale, so it has a power law relation. These QMC calculation results all agree with the theoretical expectation.

Due to the power law behaviour of the correlation function in the superfluid phase, the BKT phase transition has a strong finite size effect. The discrimina-

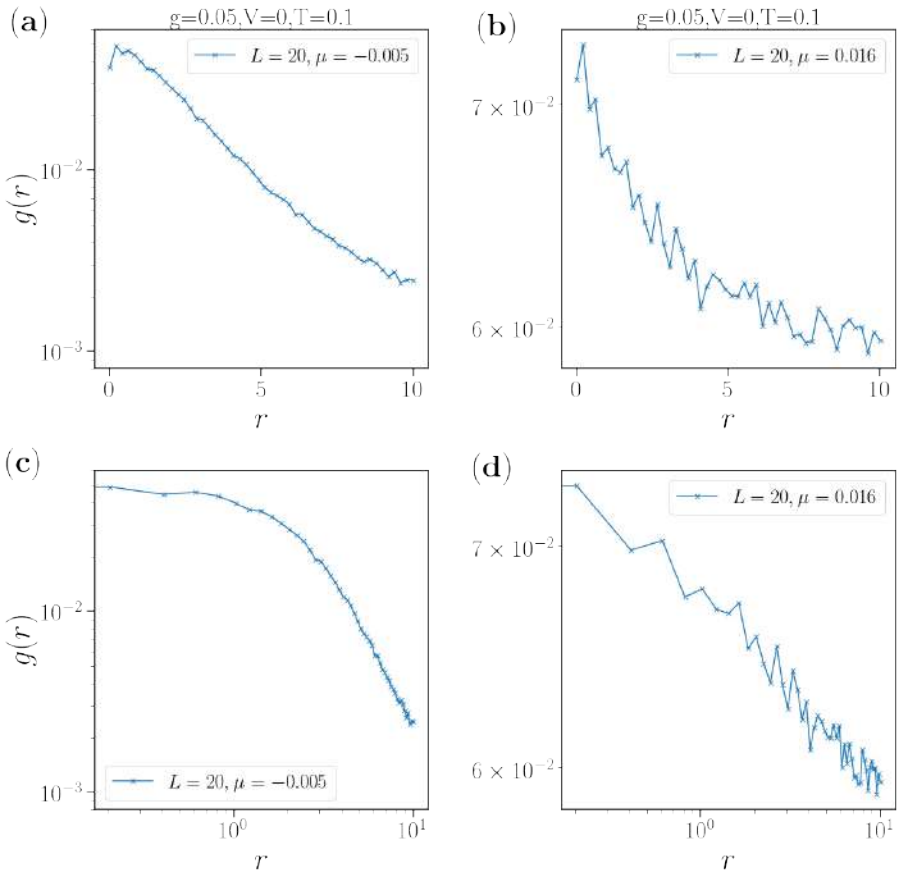


Figure 4.3: QMC results for the correlation function $g(r)$ for weakly interacting 2D bosons in homogeneous system. Interaction is $\tilde{g}_0 = 0.05$ and temperature is $T = 0.1E_r$. Left column (a) and (c) are at chemical potential $\mu = -0.005E_r$, corresponding to the normal fluid phase. Right column (b) and (d) are at chemical potential $\mu = 0.016E_r$, corresponding to the superfluid phase. The upper row (a) and (b) are plotted with the correlation function $g(r)$ in logarithm scale and the distance $r$ in linear scale. The lower row (c) and (d) are plotted with both correlation $g(r)$ and distance $r$ in logarithm scale. Linear regression on the data in (a) gives a slope $-0.015$ and a regression coefficient $r = -0.98$. Linear regression on the data in (d) gives a slope $-0.056$ and a regression coefficient $r = -0.98$.

tion between algebraic and exponential behaviour of the correlation functions is good far enough from the transition. Near the critical region, finite size analysis for the QMC numerical results is thus indispensable to locate the transition point. We calculate the equation of state and superfluid density for 2D weakly

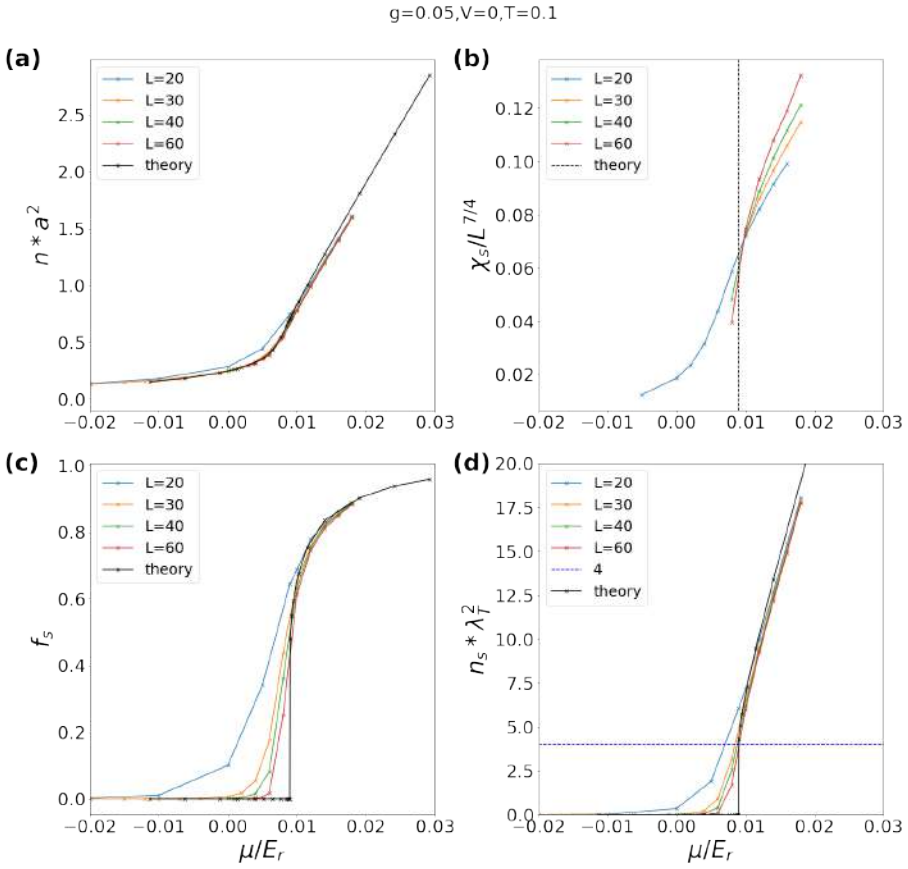


Figure 4.4: QMC results for weakly interacting 2D bosons in homogeneous system across the BKT superfluid transition point. Interaction is $\tilde{g}_0 = 0.05$ and temperature is $T = 0.1E_r$. (a) Equation of state (b) rescaled susceptibility $\chi/L^{7/4}$ (c) superfluid fraction (d) superfluid density. Calculations are performed for different system sizes $L = 20a, 30a, 40a, 60a$. The curves for the theoretical formulas are also plotted in black.

interacting Bose gas in homogeneous system with different sizes, as shown in Fig. 4.4. The interaction strength is $\tilde{g}_0 = 0.05$ and the temperature is $T = 0.1E_r$. The system sizes range from $L = 20a$ t0 $L = 60a$. As discussed in chapter 2, the critical point and the equation of state and superfluid density around the critical point was deduced by combination of analytical arguments and Monte Carlo simulation of classical $|\psi|^4$ theory [152, 153]. These theoretical results, as given in Eq. 2.36, Eq. 2.37 and Table 2.2, are plotted as black curves in Fig. 4.4.

We see in Fig. 4.4(a) that the equations of state have little finite size effects, and the results agree well with the theoretical curve. However, the superfluid fraction and superfluid density, shown in Fig. 4.4(c) and (d), converge to the

theoretical curve with a much slower pace. Theoretically, the superfluid fraction and superfluid density have a finite value jump at the critical point. On the other hand, for a finite size system, as there cannot be any non-analytic behaviour for thermodynamic variables without taking the thermodynamic limit, the superfluid fraction and superfluid density change from zero to a significant non-zero value in a continuous way. As a result, we would have a large finite size error if we simply take the point where the superfluid fraction starts to be non-zero as the critical phase transition point. We know from theory that at the transition point in the thermodynamic limit, the superfluid density $n_s$ jumps from 0 to $4/\lambda_{\mathrm{T}}^2$. This value can help us to locate the transition point as where the curve of $n_s$ cross this value $4/\lambda_{\mathrm{T}}^2$. We see in Fig. 4.4(d) that these points have a converging behaviour as system sizes increase. In addition, at critical point the correlation function jumps from power law $g(r) \sim r^{-1/4}$ to an exponential decay $g(r) \sim e^{-r/\xi}$ and the rescaled susceptibility $\chi/L^{7/4}$ for different system sizes should cross at a single point, as shown in Fig. 4.4(b). The critical point located from Fig. 4.4(b) and Fig. 4.4(d) agree with each other, giving a critical chemical potential $\mu_c \simeq 0.009E_r$.

### 4.4.2 Strong interaction

As mentioned in chapter 2, the theoretical formulas obtained by combining analytical arguments and Monte Carlo calculations over classical $|\psi|^4$ theory [152, 153] only hold in weak interaction regime. For stronger interactions, these formulas do not apply any more. However, the BKT mechanism of the superfluid phase transition still holds, as characterized by the behaviour of the correlation function $g(r)$, shown in Fig. 4.5. We see in Fig. 4.5 the QMC data of 2D Bose gas with interaction strength $\tilde{g}_0 = 0.86$ and temperature $T = 0.06E_r$, with system sizes range from $L = 20a$ to $L = 60a$. The figures are plotted with the same strategy as in Fig. 4.3, i.e. plotting the correlation functions both in semi-log scale and log-log scale. The left column, with a small chemical potential $\mu = 0.01E_r$, is for the normal fluid phase. The correlation shows linear relation only when the values of $g(r)$ are plotted in logarithm scale. So the correlation $g(r)$ itself has an exponential decay. The right column, with a large chemical potential $\mu = 0.10E_r$, is for the superfluid phase. The correlation $g(r)$ at large distance show linear relation when both $g(r)$ and $r$ are plotted in logarithm scale. It means the correlation $g(r)$ has a power law relation with the distance $r$. Thus for 2D bosons with non-weak interaction, we observe the typical behaviour of the correlation function $g(r)$ for BKT transitions, i.e. transition from power law scaling to exponential decay.

Figure 4.6 shows the QMC calculation results for equation of state, susceptibility, superfluid fraction and superfluid density for the 2D Bose gas. The interaction strength is $\tilde{g}_0 = 0.86$ and temperature is $T = 0.06E_r$. System sizes range from $L = 20a$ to $L = 60a$. Though the theoretical formulas do not apply for this case, we still plot the theoretical curves by simply inserting the value $\tilde{g}_0 = 0.86$ into the formulas. We see that for this interaction strength, the QMC results have significant difference compared to the theoretical curves which only

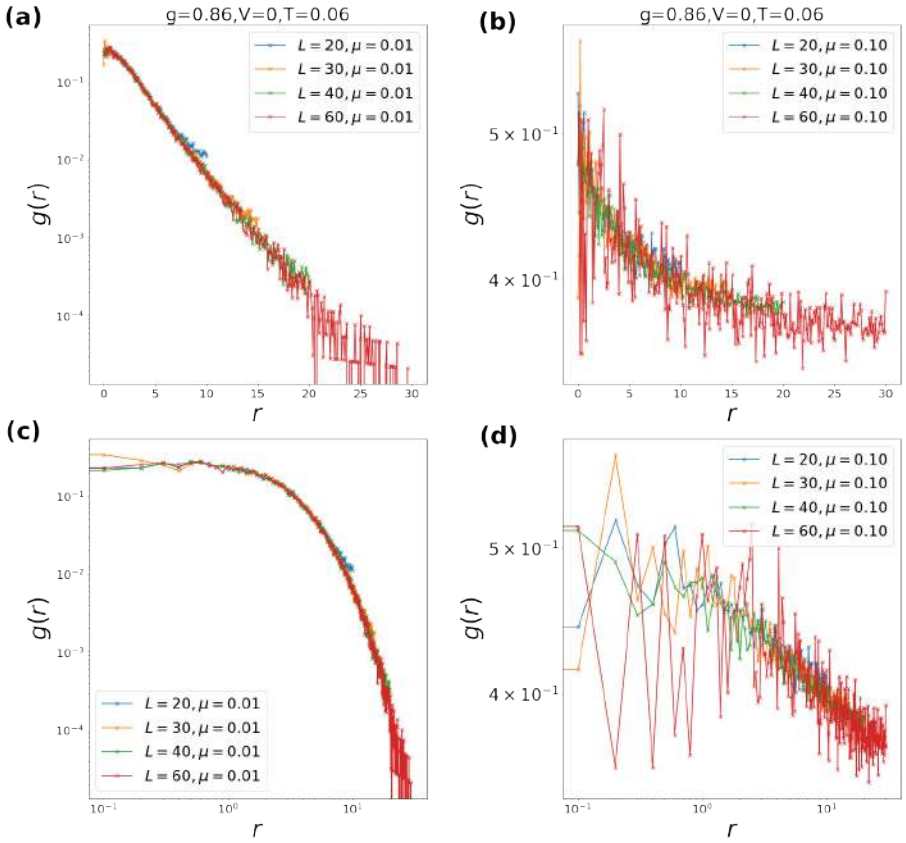


Figure 4.5: QMC results of correlation function $g(r)$ for interacting 2D bosons in an homogeneous system. Interaction is $\tilde{g}_0 = 0.86$ and temperature is $T = 0.06E_r$. Left column (a) and (c) are at chemical potential $\mu = 0.01$ in the normal fluid phase. Right column (b) and (d) are at chemical potential $\mu = 0.10E_r$ in the superfluid phase. The upper row (a) and (b) are plotted with the correlation function $g(r)$ in logarithm scale. The lower row (c) and (d) are plotted with both correlation $g(r)$ and distance $r$ in logarithm scale. Calculations are performed for different system sizes $L = 20a, 30a, 40a, 60a$. The correlation at very short distance has some strong unphysical fluctuations.

holds for weak interaction. Similar to the weak interaction case, the equations of state have little finite size effect while the superfluid fraction and superfluid density show strong finite size effects. We can locate the superfluid transition point with the same method as for weak interactions, namely the point where the superfluid density reaches value $4/\lambda_{\mathrm{T}}^2$ and the crossing point of the curves of rescaled susceptibility $\chi/L^{7/4}$ for different system sizes. We see that the critical point from Fig. 4.6(b) and Fig. 4.6(d) agree with each other, with a critical

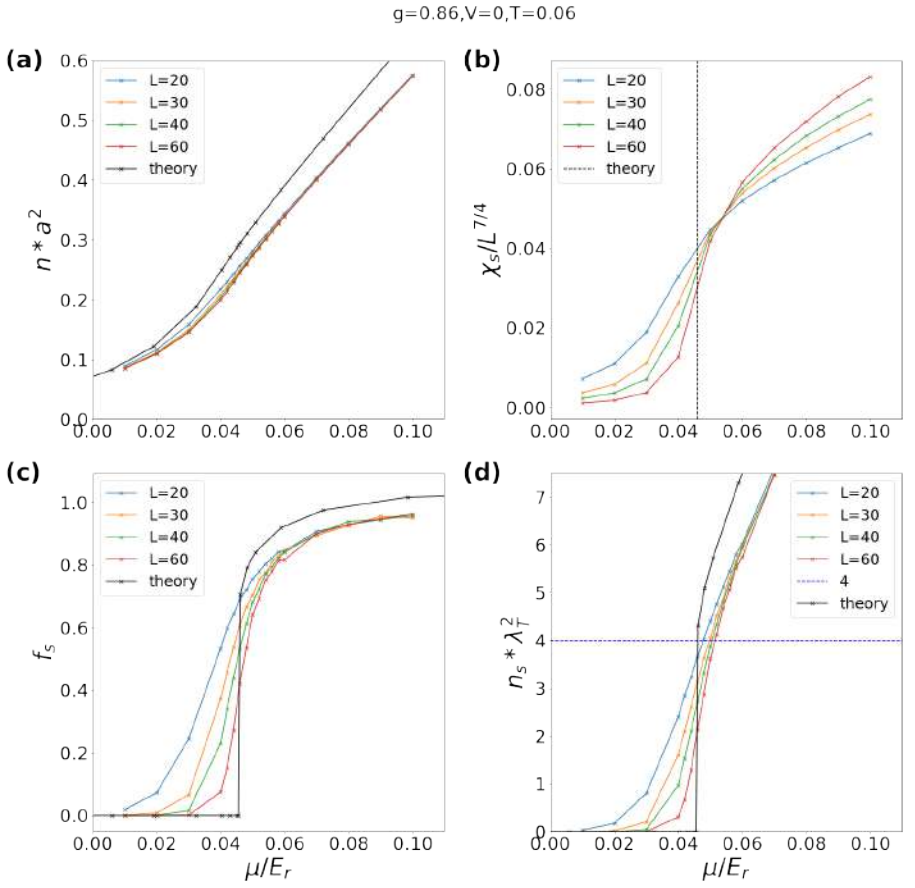


Figure 4.6: QMC results for interacting 2D bosons in homogeneous system across the BKT superfluid transition point. Interaction is $\tilde{g}_0 = 0.86$ and temperature is $T = 0.06E_r$. (a) equation of state (b) rescaled susceptibility $\chi/L^{7/4}$ (c) superfluid fraction (d) superfluid density. Calculations are performed for different system sizes $L = 20a, 30a, 40a, 60a$. The curves for the theoretical formulas by directly inserting the interaction value $\tilde{g}_0 = 0.86$ are also plotted in black.

chemical potential $\mu_c \simeq 0.052E_r$. The same set of data are also calculated and plotted for interaction strength $\tilde{g}_0 = 5$, shown in Fig. 4.7. Though the theoretical curves are even more irrelevant for this case, we still observe the familiar behaviour of the equation of state and superfluid transition, and we can get the critical point of BKT transition in the same way as before.

Equipped with the data and methods discussed above, we can perform the QMC calculations to get the equation of state and superfluid transition point of 2D interacting Bose gas in homogeneous system for any set of parameters of

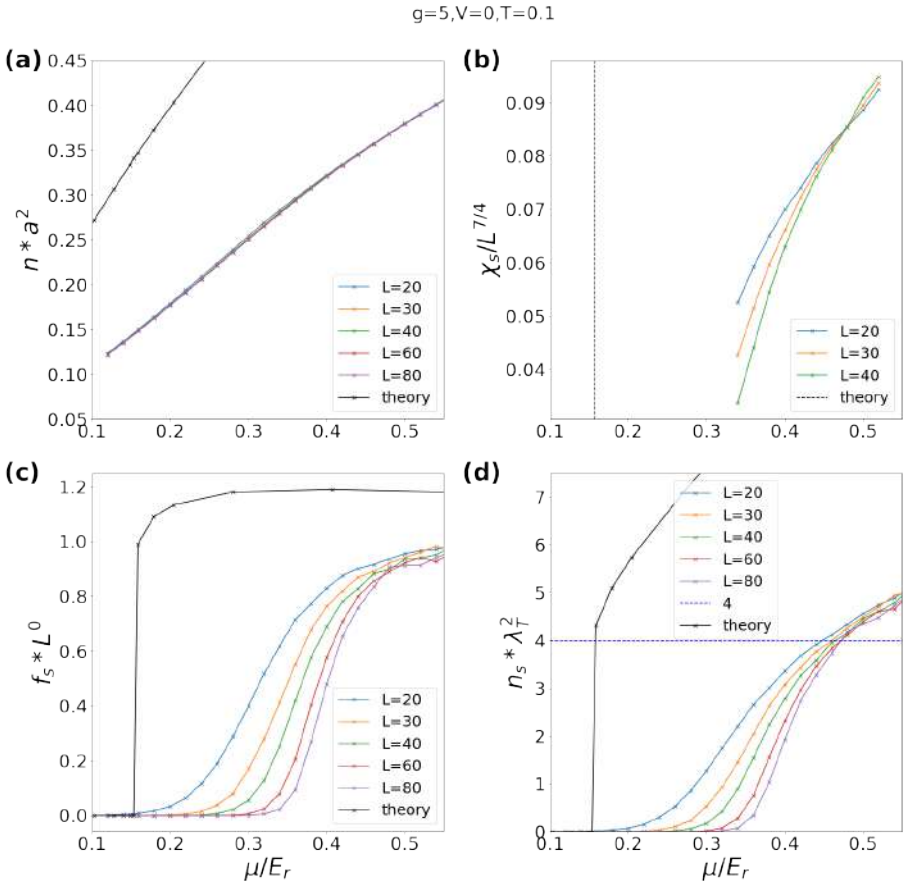


Figure 4.7: QMC results for interacting 2D bosons in homogeneous system across the BKT superfluid transition point. Interaction is $\tilde{g}_0 = 5$ and temperature is $T = 0.1E_r$. (a) equation of state (the curves for different $L$ are almost on top of each other in the middle of the figure, while the theoretical black curve is far from them in the up left corner) (b) rescaled susceptibility $\chi/L^{7/4}$ (c) superfluid fraction (d) superfluid density. Calculations are performed for different system sizes $L = 20a, 30a, 40a, 60a$. The curves for the theoretical formulas by directly inserting the interaction value $\tilde{g}_0 = 5$ are also plotted in black.

interaction $\tilde{g}_0$ and temperature $T$. This allows us to do the comparison with the Bose gas in quasicrystal potentials and identify the thermodynamic phases.

## 4.5 Bosons in quasicrystal potential

We now turn to the 2D bosons in a quasicrystal potential. The physical observables at equilibrium in grand canonical ensemble are calculated by QMC

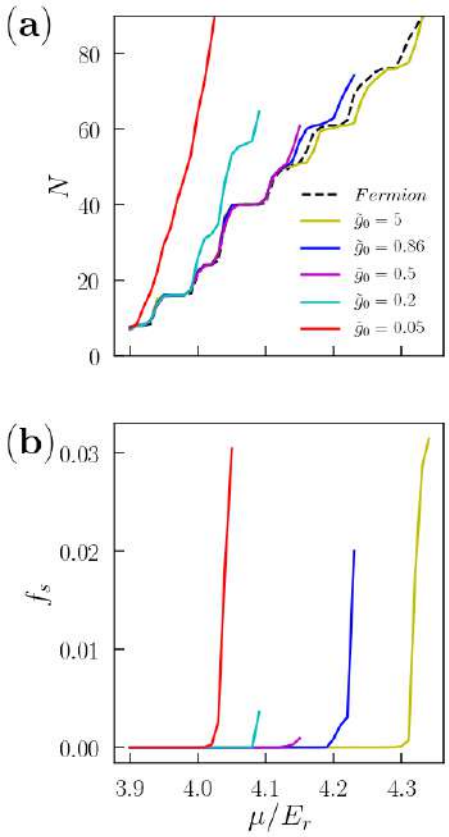


Figure 4.8: (a) Number of particles $N$ versus chemical potential $\mu$ for bosons with different interactions and free fermions, with the same temperature $T = 0.0025E_r$.(b) Same curves for superfluid fractions $f_s$ as calculated by QMC

method. As usual, we take the lattice constant $a$ as the length unit and recoil energy $E_r$ as the energy unit.

### 4.5.1 Interplay of localization, interaction and temperature

We first do the calculation in a square system with linear size $L = 20a$. Consider the zero temperature limit. The QMC results are shown in Fig. 4.8 (a) for total particle number $N$ and in Fig. 4.8 (b) for superfluid fraction $f_s$. We see that smaller interaction strength $\tilde{g}_0$ gives larger particle number. At small chemical potential $\mu$, the particle number curves for interacting bosons may coincide with the curve for free fermions, which has a bunch of plateaus of $N$, see the dash black curve in Fig. 4.8 (a). The boson curves depart from

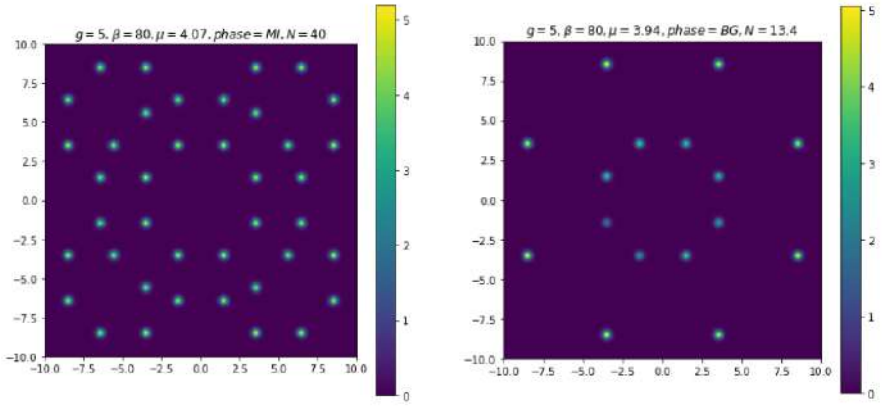


Figure 4.9: Particle number density profile $n(\mathbf{r})$ in a system with linear size $L = 20a$. Interaction strength $\tilde{g}_0 = 5$, temperature $T = 0.0025E_r$. Left: Mott rings with an integer number of bosons $N = 40$. Right: Bose glass phase with incommensurate filling $N = 13.4$.

the fermion curve at a larger chemical potential for larger interactions. The interacting bosons enter the superfluid phase for higher chemical potentials, and we find the chemical potential at superfluid transition point increase with the interaction strength, see Fig. 4.8(b).

The behaviour of the boson curves is closely related to the localization effect in the quasicrystal potential. For a weak chemical potential, the bosons populate the low-lying single-particle states which are strongly localized. With strong enough repulsive interactions, multiple occupation of the same deep potential well is suppressed, see more discussion on fermionization in the next part. In the eightfold quasicrystal potential, the single-particle states are organized in rings of 8 or 16 spots. Above the localization threshold, tunneling is suppressed between the different rings. In contrast, within each ring, the spots are strictly degenerate, and thus form a narrow energy band in the single particle spectrum. However, interactions suppress phase coherence, hence forming ring Mott insulators at commensurate fillings when the chemical potential lies in the energy gaps, see the plateaus of particle number $N$ in Fig. 4.8(a), where the compressibililty $\kappa$ is vanishing. Figure 4.9(left) shows the density $n(\mathbf{r})$ in this case. The total number of bosons is an integer $N = 40$ and these bosons are all localized in deep potential wells, while each site has just one boson. In between two gaps, the chemical potential is within a narrow band and incommensurate filling induces density fluctuations in the ring while long-range coherence is still suppressed since the different rings remain phase incoherent, see the sloping part of particle number $N$ in Fig. 4.8(a) where the compressibililty $\kappa$ is nonzero and the superfluid fraction is zero. This forms a compressible insulator, hence a BG at zero temperature. Figure 4.9(right) shows the density $n(\mathbf{r})$ in this phase.

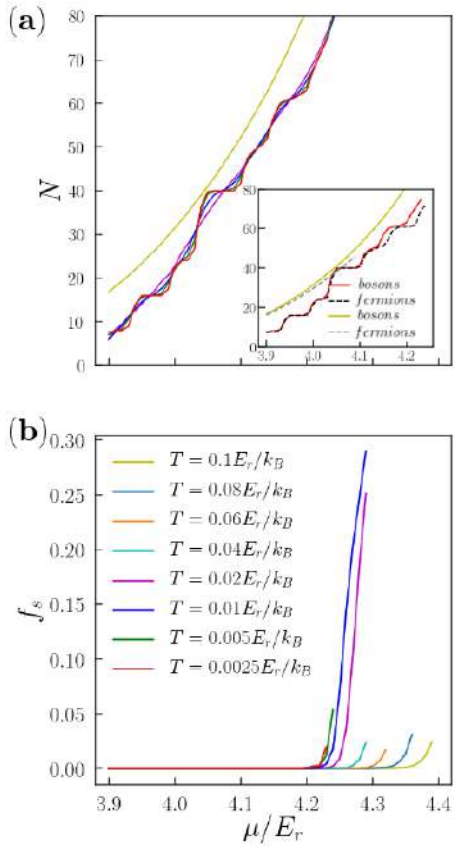


Figure 4.10: (a) Number of particles $N$ versus chemical potential $\mu$ on various temperatures for bosons with the same interaction strength $\tilde{g}_0 = 0.86$. Inset: comparision between interaction bosons and free fermions. (b) Same curves for superfluid fractions $f_s$

The total number of bosons is $N = 13.4$. While the eight spots on the outer ring are each filled by one boson, the inner ring of eight spots are incommensurately filled with density fluctuations.

We turn to finite temperatures now. The QMC results are shown in Fig. 4.10. As thermal fluctuations induce particle number fluctuation and give rise to nonzero compressibility, the Mott plateaus are smoothed out and vanish when the thermal energy $k_B T$ is comparable to the Mott gaps, see Fig. 4.10(a). On the other hand, thermal fluctuations also suppress superfluid phase coherence, thus the chemical potential of the superfluid transition point is pushed to a higher value for higher temperatures, see Fig. 4.10(b). So at finite temperatures, thermal fluctuations favor the BG phase at the expense of the MI and SF phases, in competition with the emergence of a NF phase for high enough temperatures,

where thermal fluctuations also dominate over the localization effects.

### 4.5.2 Fermionization

As we see in Fig. 4.9, the bosons in the quasicrystal potential with strong enough interaction at low chemical potential are distributed in a spatially separated way, with each local potential well accomodating at most one boson. This interaction blockade picture, is equivalent to real-space fermionization of 2D bosons. As the bosons are spatially separated, there is no interaction energy, and the strongly interacting bosons are equivalent to non-interacting free fermions. This fermionization idea can be checked by plotting the equation of state of fermions calculated from the Fermi-Dirac distribution, as shown in Fig. 4.8(a) (dashed black line). We see that indeed at low chemical potential the equation of state curves for the bosons lie on top of the free fermion curve.

This fermionization picture is expected to break down when a single site is populated by more than one boson. So in order to have the boson curve depart from the free fermion curve, the chemical potential should compensate the interaction energy of putting a second boson in an already occupied site. Consistently, the chemical potential at the departure point of the boson and fermion curve is larger for stronger interaction, see Fig. 4.8(a). The departure from the fermionization picture can also happen in the opposite direction, in the sense that the particle number of bosons may be smaller rather than larger compared to the particle number of fermions. Thus the equation of state curve of bosons would be lower than the Fermi-Dirac curve. This happens for bosons with strong interaction and will be discussed in a later section.

This fermionization picture also holds at finite temperatures. The particle number of bosons can still be evaluated by using the Fermi-Dirac distribution at finite temperature as

$$N \simeq \sum_j \frac{1}{\mathrm{e}^{(E_j-\mu)/k_{\mathrm{B}}T}+1}, \tag{4.8}$$

where $k_{\mathrm{B}}$ is the Boltzmann constant. The QMC results for interacting bosons are in excellent agreement with Eq. (4.8) in the low chemical potential and low temperature regime, see Fig. 4.11. Thermal fluctuations enhance multiple occupation of individual sites and the fermionization picture is expected to break down for a chemical potential about $\sim k_{\mathrm{B}}T$ smaller compared to the zero temperature case. We consistently find that the fermionization picture breaks down at a lower chemical potential as the temperature increases, see Fig. 4.11. In particular, we find that the QMC boson curve deviates from Eq. (4.8) about at about $0.1E_r$ smaller chemical potential for $T = 0.1E_{\mathrm{r}}/k_{\mathrm{B}}$ compared to $T = 0.0025E_{\mathrm{r}}/k_{\mathrm{B}} \simeq 0$, see inset of Fig. 4.10(a).

### 4.5.3 Necessity of finite size analysis

With the above discussed QMC results for 2D interacting bosons in a $L = 20a$ square, and similar set of data for different interactions and temperatures,

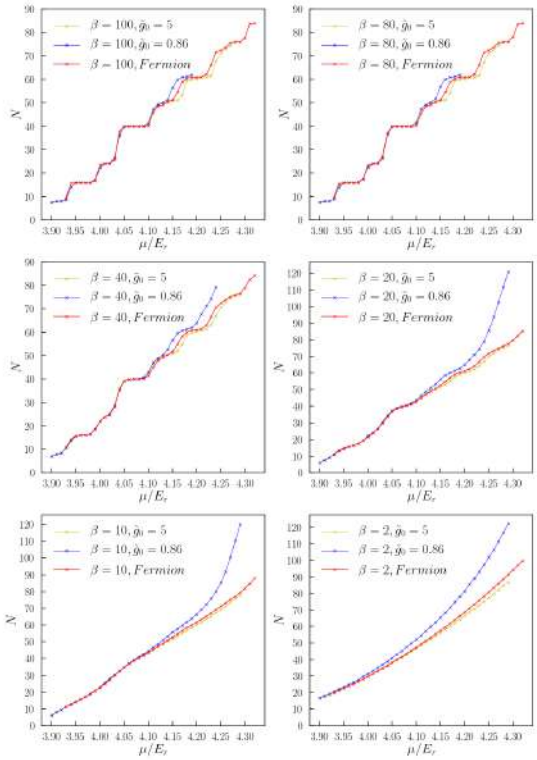


Figure 4.11: Fermionization for 2D bosons in quasicrystal potential, with interaction strength $\tilde{g}_0 = 0.86$ and $\tilde{g}_0 = 5$. Quasicrystal potential is $V_0 = 2.5$ and system size is $L = 20a$. $\beta$ is a dimensionless parameter related to the temperature as $\frac{1}{\beta} = \frac{\pi^2}{2}\frac{T}{E_r}$. Particle numbers $N$ are plotted against chemical potentials $\mu$. The fermions curves are calculated by Fermi-Dirac distribution on the single particle spectrum. The temperatures are $(1)\beta = 100, T = 0.002E_r$, $(2)\beta = 80, T = 0.0025E_r$, $(3)\beta = 40, T = 0.005E_r$, $(4)\beta = 20, T = 0.01E_r$, $(5)\beta = 10, T = 0.02E_r$, $(6)\beta = 2, T = 0.1E_r$.

we may obtain the phase diagrams according to our methods of identifying different phases. Actually, the phase diagrams thus obtained do not display the phases at the thermodynamic limit as the ones shown in Fig.4.2. As we will discuss below, the reason is that the data for $L = 20a$ systems cannot really represent the physics at the thermodynamic limit (where the concept of phase

is rigorously defined) in a faithful way.

For the identification of any phase transition, the finite size effect is always a problem to be dealt with. However, a careful finite size analysis is particularly necessary for our case. This originates from several aspects. For the superfluid transitions, as we already discussed, BKT transitions for two dimensional interacting bosons have strong finite size effects, due to the power law scaling of the correlation function. As a consequence, using the data for only $L = 20a$ to locate the BG-NF and BG-SF transition cannot give accurate result. This is even further complicated by the quasicrystal potential. In homogeneous or periodic systems, the physical quantities usually vary monotonously with the system size $L$. This is not true in quasicrystal potential as the potential does not vary in a regular way (see more detail on this in the next section 4.5.4).

The identification of MI phases also requires a careful finite size analysis. This is because the position of the Mott lobes in a $L = 20a$ system may be quite different if we pick a $L = 20a$ square area at another place in the quasicrystal. For a periodic potential, as long as the system contains a certain number of unit cells, there would be no difference if we pick the system in one place or another place. They will lead to exactly the same result just because the system is periodic, i.e. possesing some translational invariance. For a disordered system, as long as the system size is much larger than the typical disorder correlation length $\sigma$, then the fine detail of the disorder will be lost and there will again be negligible difference if we pick one area or another at a different place. In contrast, the quasicrystal potential by definition has no translational symmetry, so each finite area picked at different place will be different. On the other hand, quasicrystal is long range ordered, so there is no length scale as the correlation length $\sigma$ for disorder. As a result, a finite size system of quasicrystal potential is not guaranteed to be well representative of the physics of another finite area with the same size. The system at thermodynamic limit, viewed as combination of many finite size systems, thus may not mimic the behaviour in any single finite size system.

Take for consideration the small Mott plateaus at low chemical potential for $\tilde{g}_0 = 5$ shown in Fig. 4.8(a). According to the fermionization picture, the position of these plateaus agree with the plateaus of the Fermi-Dirac distribution for free fermions, so they correspond to the energy gaps in the single particle spectrum in the $L = 20a$ system. However, as we showed in Fig. 3.6 in chapter 3, the single particle energy gaps at $L = 20a$ are not true gaps in the thermodynamic limit. In fact, the single particle gaps for $L = 20a$ appear at different positions for systems at different locations. So the interacting bosons also become Mott insulator at different chemical potentials. At thermodynamic limit, take the full system as combination of many $L = 20a$ squares. When some squares are in the incompressible MI phase, many other squares may be in the compressible phase. As a result, all these kinds of Mott insulators for small systems will merge into the Bose glass phase, just as those single particle gaps for small systems will disappear for larger systems and the Fermi-Dirac curve will have no plateau at low chemical potential, see Fig. 3.6.

In summary, in order to get the phase diagrams at thermodynamic limit, it

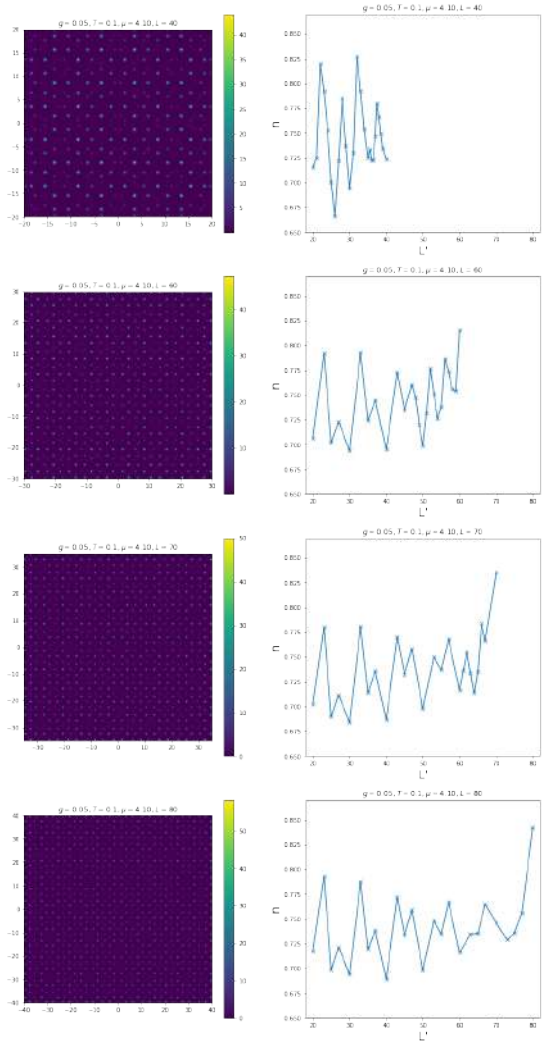

Figure 4.12: Left column: particle number density profiles for 2D bosons in quasicrystal potential. Parameters are $\tilde{g}_0 = 0.05$, $T = 0.1E_r$, $\mu = 4.10E_r$. The four rows are for four different system sizes $L = 40a, 60a, 70a, 80a$. The color scale represents the value of local particle number density $n(\mathbf{r})$, from large (yellow) to small (blue). Right column: the average particle number density $n(L')$ in the fictitious square with size $L' < L$ as a function of $L'$.

is indispensable to perform finite size analysis.

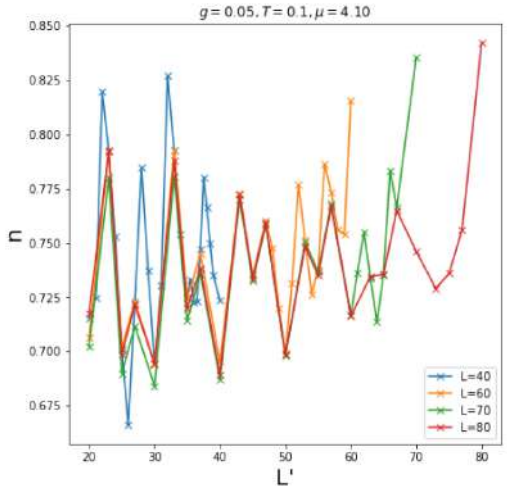


Figure 4.13: The same data of right column of Fig. 4.12 plotted on top of each other.

### 4.5.4 Fluctuation against system sizes

We do the QMC calculation for 2D interacting bosons in quasicrystal systems for different system sizes. In contrast to the case of homogeneous systems, where the equations of state have negligible finite size effect as shown in Fig. 4.4, Fig. 4.6 and Fig. 4.7, in quasicrystal potential with $V_0 = 2.5E_r$ the particle number densities have quite significant fluctuation against system size. For a better understanding of this fluctuation, we take the following approach: For a square with size $L$, draw a smaller co-centered fictitious square with size $L' < L$, then take the integral of local particle number density $n(\mathbf{r})$ inside this fictitious square to get the total particle number in the fictitious square $N(L')$. The average particle number density inside the fictitious square reads $n(L') = \frac{N(insideL'*L')}{L'^2}$, and we look at how this density $n(L')$ varies against $L'$. In this way, we can better differentiate the fluctuations in the bulk region, which are intrinsic for quasicrystal potential, and fluctuations in the edge region, which may be due to some boundary effects.

The results for $\tilde{g}_0 = 0.05, T = 0.1E_r$ and $\mu = 4.10$ are shown in Fig. 4.12. The four rows refer to different total system sizes $L = 40a, 60a, 70a, 80a$. The right column shows the density in the fictitious square $n(L')$ against $L'$. The left column shows the corresponding real space density profile in the full square. We see $n(L')$ fluctuates with $L'$. In addition, as we plot these curves of $n(L')$ for different $L$ on the same figure, as shown in Fig. 4.13, we see that if $L'$ is not close to $L$, $n(L')$ fluctuates with $L'$ in the same way for different total sizes $L$. So these fluctuations of $n(L')$ when $L'$ not close to $L$ are physical. It is due to the quasicrystal having deep potential wells, where local density $n(r)$ is large,

see the density spots in the left column of Fig. 4.12. As $L'$ increases, the area of the fictitious square may suddenly include some new potential wells, and this leads to a sudden increase of the average density $n(L')$. Furthermore, we expect this fluctuation decreases with larger $L'$. The sudden inclusion of new potential wells happens on the boundary of the fictitious square, and the length of square periphery scales as $L'$. The area of the square scales as $L'^2$. Consequently, we expect the average density in the fictitious square $n(L')$ to have a scaling as $\sim \frac{L'}{L'^2} = \frac{1}{L'}$. This is qualitatively in agreement with the numerical results, though it is difficult to check that scaling relation as the system size is limited in numerical calculations. On the other hand, we see in Fig. 4.13 that the $n(L')$ curves for different $L$ do not always have the same behaviour. As $L'$ approaches $L$, $n(L')$ curves deviate from each other for different system size $L$. So the $n(L')$ fluctuations in this region are not only due to quasicrystal potential but also due to the boundary effects.

With these understandings of the behaviours of $n(L')$, the fluctuations of the data in quasicrystal potential are not surprising nor mysterious for us. For our practical purpose, we can just get a reasonable estimation of particle number density at thermodynamic limit by calculating the $n(L)$ for various system sizes $L$ and taking their averages.

## 4.6 Superfluid-to-Bose glass transition

With all the above considerations noted, we embark on the task of identifying the phases at thermodynamic limit by the combination of the data for homogeneous and quasicrystal systems.

Typical QMC results for the total particle density $n = N/L^2$ and the SF density $n_\mathrm{s} = f_\mathrm{s} \times n$ versus chemical potential for various system sizes are shown on Fig. 4.14 for intermediate interaction strength and temperature, $\tilde{g}_0 = 0.86$ and $T = 0.06 E_\mathrm{r}/k_\mathrm{B}$. Similar results are found in all ranges of temperature, chemical potential, and interaction strength considered for the phase diagrams of Fig. 4.2, up to the MI phase relevant for strong interactions (see below). In the absence of a quasicrystal potential, $V_0 = 0$ [Fig. 4.14(a), left column], the QMC results show a clear NF-to-SF transition, characteristic of the expected Berezinskii-Kosterlitz-Thouless (BKT) behavior [149, 150, 152, 153, 178]. The density is a smooth function of the chemical potential and shows weak finite-size effects, see Fig. 4.14(a1) [179]. In constrast, the SF density shows strong size dependence, see Fig. 4.14(a2). For low chemical potential, $n_\mathrm{s}$ scales down with $L$, pointing towards a NF phase, while for high chemical potential, it converges to a finite value, as expected in the SF phase. See also Fig. 4.14(a3), which shows the variation of $n_\mathrm{s}$ with the system size for various values of the chemical potential. This behaviour is consistent with the BKT universal jump at criticality, $n_\mathrm{s}\lambda_\mathrm{T}^2 = 4$ with $\lambda_\mathrm{T} = \sqrt{2\pi\hbar^2/mk_\mathrm{B}T}$ the thermal de Broglie wavelength. It allows us to precisely locate the NF-to-SF transition point as the chemical potential $\mu_\mathrm{c}'$ such that $n_\mathrm{s}\lambda_\mathrm{T}^2 = 4$ for the largest considered sizes. We use a conservative errorbar for the critical chemical potential corresponding to

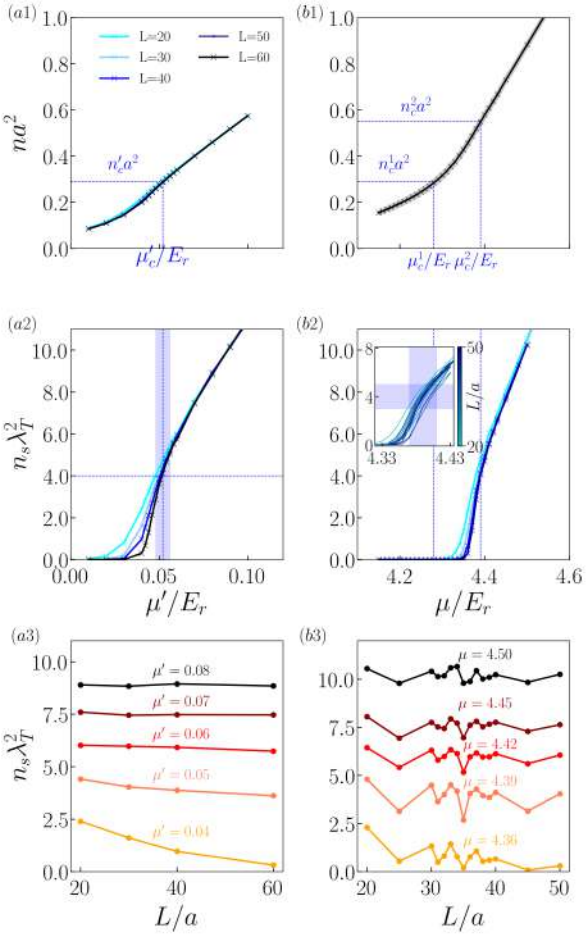


Figure 4.14: Total particle density (upper row) and SF density versus chemical potential (middle row) as well as versus system size (lower row) for a 2D Bose gas with interaction strength $\tilde{g}_0 = 0.86$ and temperature $T = 0.06E_\mathrm{r}/k_\mathrm{B}$, in the absence (left column) and in the presence (right column, $V_0 = 2.5E_\mathrm{r}$) of a quasicrystal potential. The QMC calculations are performed in square boxes for different linear sizes $L$ corresponding to the different line colors in the upper and middle rows. The QMC statistical errorbars are smaller than the markers. In panel (b1), the shaded area corresponds to the standard deviation of the density fluctuations with the system size. The inset in (b2) is a magnification of its main panel in the vicinity of the critical point for many system sizes with $L/a \in [20, 50]$ and the shaded area is the construction to locate the SF-to-BG transition point. Panels (a3) and (b3) show the SF density as a function of $L$ for various chemical potentials in the vicinity of the SF transition.

the variation of $\mu'$ with the system size in the range $L/a \in [20, 60]$, see shaded area in Fig. 4.14(a2). Although it can be refined using appropriate finite-size scaling [152], it appears to be sufficient for our purpose. The corresponding critical density, $n'_{\rm c}$, is then found using the equation of state (particle density versus temperature and chemical potential) as found from QMC calculations, see Fig. 4.14(a1). For the parameters of Fig. 4.14(a), it yields $\mu'_{\rm c} = 0.052 \pm 0.004$ and $n'_{\rm c} = 0.29 \pm 0.03$.

We now turn to the behavior of the Bose gas in the presence of the quasicrystal potential. Firstly, the NF regime is found by combining the above results with their counterparts at $V_0 \neq 0$ [Fig. 4.14(b), right column]. For a given interaction strength and temperature, we use the equation of state at $V_0 \neq 0$ to infer the chemical potential $\mu^1_{\rm c}$ corresponding to the critical density of the homogeneous gas, $n^1_{\rm c} = n'_{\rm c}$, see Fig. 4.14(b1). It yields the NF-BG threshold shown on the phase diagrams of Fig. 4.2. Note that at $\mu^1_{\rm c}$, we find a finite compressibility $\kappa = \partial n/\partial\mu$ [finite slope in Fig. 4.14(b1)] and a vanishingly small $n_{\rm s}$ [see Fig. 4.14(b2)], which allows us to discriminate the BG against the SF and the MI.

Secondly, having identified the NF regime, we can focus on the BG-to-SF transition. Compared to the homogneous case, the QMC results in the presence of the quasicrystal potential show stronger finite-size effects of both quantities $n$ and $n_{\rm s}$. The equation of state shown on Fig. 4.14(b1) is the density versus chemical potential averaged over the system size in the range $L \in [20, 50]$ with the shaded area corresponding to the standard deviation. On top of these fluctuations, the SF density nevertheless shows a clear finite-size scaling, qualitatively reminiscent of that found in the homogeneous gas at the NF-to-SF transition, see Fig. 4.14(b2). The inset of Fig. 4.14(b2) is a magnification in the vicinity of the transition with more system sizes where the fluctuations of $n_{\rm s}$ versus $L$ are more clearly seen. We find that the SF density sharply crosses over from vanishingly small values to a few units of $1/\lambda^2_{\rm T}$. We then locate the SF transition in the middle of the interval of chemical potentials such that $3 \leq n_{\rm s}\lambda^2_T \leq 5$ for all system sizes in the range $L/a \in [30, 50]$, the errorbar corresponding to the size of this interval. The BG-to-SF transition obtained here is clearly distinguished from the NF-BG threshold. For instance, for the parameters of Fig. 4.14, we find $\mu^1_{\rm c} = 4.28 \pm 0.02$ and $n^1_{\rm c} = 0.29 \pm 0.03$ at the NF-BG threshold and $\mu^2_{\rm c} = 4.39 \pm 0.02$ and $n^2_{\rm c} = 0.55 \pm 0.05$ at the BG-to-SF transition.

The values of $\mu^1_{\rm c}$ and $\mu^2_{\rm c}$ versus $T$ hence obtained are used to locate the NF-BG threshold and the BG-to-SF transition on the phase diagrams of Fig. 4.2, together with the corresponding errorbars.

## 4.7 Mott insulator phase for strong interaction

We now turn to the strongly-interacting regime ($\tilde{g}_0 \gg 1$), where MI lobes emerge, see Fig. 4.2(c). Typical QMC results for the density and superfluid fraction are shown on Fig. 4.15, for (a) vanishingly small and (b) finite temperatures. The different line colors correspond to different sizes on panel (a)

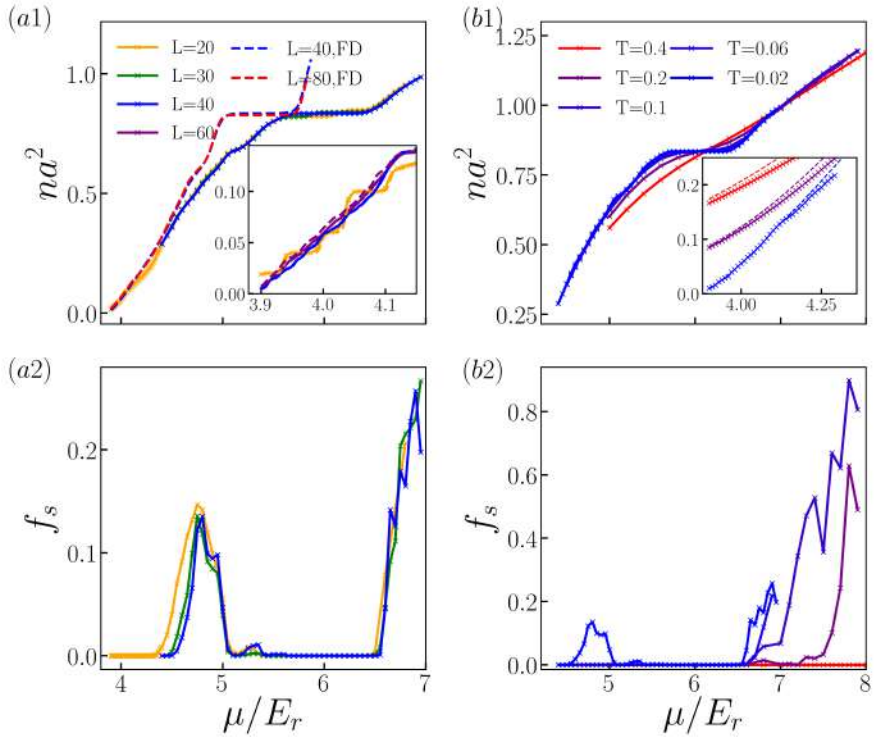


Figure 4.15: Strongly-interacting regime, $\tilde{g}_0 = 5$. The upper and lower rows show, respectively, the total particle density and the SF fraction versus the chemical potential. Left column: Low-temperature regime, $T = 0.02E_{\rm r}/k_{\rm B}$, for various system sizes. The Inset of (a1) shows the low-density regime for even lower temperature, $T = 0.0025E_{\rm r}/k_{\rm B}$. Right column: Behaviour for various temperatures and a system size $L = 40a$. QMC results for the interacting Bose gas are shown as markers and solid lines, while the Fermi-Dirac (FD) predictions, Eq. (4.9), are shown as dashed lines.

and different temperatures on panel (b). For a weak chemical potential, the bosons populate the low-lying single-particle states, where strong repulsive interactions suppress multiple occupancy. This mimics Pauli exclusion in real space and a simple fermionization picture accounts for the equation of state of the strongly-interacting Bose gas, within the Fermi-Dirac distribution,

$$n \simeq \frac{1}{L^2} \sum_j \frac{1}{\mathrm{e}^{(E_j-\mu)/k_{\rm B}T}+1}, \tag{4.9}$$

where $j$ spans the set of single particle states, with energy $E_j$. This formula (dashed lines) indeed shows good agreement with the QMC results (solid lines)

at vanishing, as well as finite temperatures and low chemical potential, see Insets of Fig. 4.15(a1) and (b1).

Consider first the low-temperature regime. The lowest states are localized and, owing to the eightfold rotational symmetry of the quasicrystal potential, they are arranged in rings of 8 or 16 trapping sites. The interacting Bose gas then organizes in MI rings, characterized by Mott plateaus at commensurability, see Inset of Fig. 4.15(a1). Out of commensurability, finite tunneling between the trapping sites of a given ring generates ring superfluidity, but energy gaps between the different rings prevent long-range superfluidity, hence creating a BG phase. We consistently find that the SF fraction vanishes for $\mu \lesssim 4.4E_{\rm r}$, see Fig. 4.15(a2). Similar phenomenology was observed in small systems in Ref. [52]. However, when the system size increases, new rings with slightly shifted energies appear. This progressively fills the smallest gaps and blurs the corresponding Mott plateaus as observed in our QMC results when the system size increases, see Inset of Fig. 4.15(a1). In the thermodynamic limit, the compressibility is thus finite and we find a BG. In contrast, the QMC results show that the largest gaps survive when the system size increases, hence creating legitimate MI phases. This occurs, for instance, for $\tilde{g}_0 = 5$ and $5.5E_{\rm r} \lesssim \mu \lesssim 6.4E_{\rm r}$, see Fig. 4.2(c) as well as Figs. 4.15(a1) and (b1). This is consistent with the survival of a single-particle gap and the existence of a plateau in the Fermi-Dirac prediction (4.9) at the same density and even larger systems, see Figs. 4.15(a1). Here, however, the chemical potential is high enough to populate many states, made of a large number of trapping sites, with nonzero spatial overlap. This generates a finite, positive interaction energy, which contributes to the chemical potential and correspondingly shifts the QMC results for interacting bosons compared to the Fermi-Dirac distribution.

We finally discuss the finite-temperature effects. When the temperature increases, the Mott plateaus shrink. The compressibility becomes finite but the SF fraction remains zero, hence progressively opening BG phases on the edges of the Mott plateaus, see Figs. 4.15(b1) and (b2). For low enough temperature, the plateaus are still marked with very small compressibility and we identify $\kappa < 0.01m/\hbar^2$ to a finite-temperature MI regime, corresponding to the MI lobes in the phase diagram of Fig. 4.2(c). As expected, finite temperatures also suppress the SF fraction in the SF phases and give space to the BG when it vanishes, see Fig. 4.15(b2). Note that, here, the Bose gas is a superfluid in the absence of the quasicrystal potential, hence the compressible insulator we obtain is a legitimate finite-temperature BG.

## 4.8 High temperature phase diagrams

We have also performed calculations up to significantly higher temperatures. The phase diagrams with larger temperature ranges are shown in Fig. 4.16. The grey areas correspond to the error bars of the BG-SF and NF-BG phase transitions. We see that as temperature increases, the error bars of the two transition lines are merging, and the Bose glass phases are narrowing and vanishing. The

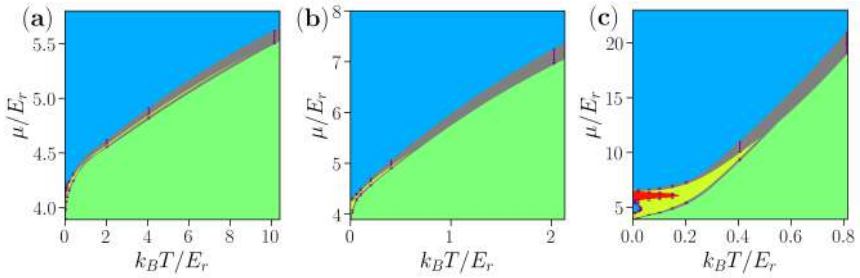


Figure 4.16: Thermodynamic phase diagrams up to high temperatures for (a) $\tilde{g}_0 = 0.05$, (b) $\tilde{g}_0 = 0.86$, and (c) $\tilde{g}_0 = 5$. Grey zones correspond to the regions defined by the errorbars around the phase transition points.

phase diagrams show that the Bose glass survives up to temperatures of about $T \simeq 8E_{\rm r}/k_{\rm B}$ for $\tilde{g}_0 = 0.05$, $T \simeq 0.7E_{\rm r}/k_{\rm B}$ for $\tilde{g}_0 = 0.86$, $T \simeq 0.5E_{\rm r}/k_{\rm B}$ for $\tilde{g}_0 = 5$. However, these temperatures are rather high for ultracold-atom experiments where the temperature is significantly sub-recoil, and compared to the phase diagrams in Fig. 4.2, these high temperature phase diagrams shrink the most interesting part of the phase diagrams where the different phases compete.

## 4.9 Experimental relevance

We now discuss the experimental relevance of the phase diagrams we obtained.

On the one hand, our work is directly relevant to experiments performed in a box, which are implementable. There has been important progress in this direction in the last years, in particular for 2D systems, see for instance Refs. [180–182]. In principle, nothing prevents the addition of a quasicrystalline potential and thus realize the model we are studying.

On the other hand, most ultracold-atom experiments are still performed in harmonic traps, which are easier to realize. Yet, the ultimate goal of quantum simulation as realized in these experiments is to extract the physics of standard condensed-matter models, which are typically homogeneous. In this sense, our work provides the "goal" of such experiments. In experiments, extraction of the bulk properties can be performed using local density approximation (LDA). More precisely, applicability of LDA in an experimental quantum simulator is arguably a necessary condition to realize this goal, so that the position in the trap can be mapped onto an effective chemical potential, using $\mu \to \mu - V_{\rm trap}(\mathbf{r})$. Here, this applies when the variation of the trapping potential $V_{\rm trap}(\mathbf{r})$ is sufficiently weak over a length scale such that the finite size effects in the 2D quasicrystal are negligible and the thermodynamic phase is nearly homogeneous on this scale. According to our calculations, a size of $L \sim 40a$ is a minimum. Our results realized in a homogeneous system hence gives particularly useful

guidance for the applicability of LDA in quasicrystal simulation experiments of ultracold atoms confined in arbitrary traps (including harmonic as well as non harmonic ones). For instance, the experimental parameters used in the quasicrystal simulation experiments at Cambridge, Refs. [47, 49], indicate a harmonic trapping potential such that $V_{\rm trap} \simeq 0.01 E_{\rm r}$ at a distance $40a$ from the center of the trap, smaller than typical energy scales in our phase diagrams, and LDA is well applicable around the center of the trap.

Vice-versa, LDA can be applied to our results for comparison to experiments (or numerical calculations) performed in any trap. To this end, we note that it is vital to work out phase diagrams in the thermodynamic sense, in particular in the grand-canonical ensemble, i.e. as a function of the chemical potential, as well as in homogeneous systems, and analyzing finite-size effects. This is what is done in our work.

## 4.10 Perspectives

### 4.10.1 Relation between the Mott insulator and small ring states

As we observed in Fig. 4.15(a), the Mott insulator phase has the same particle number density as the plateau of the Fermi-Dirac curve for free fermions which originates from a large energy gap in the single particle spectrum. This suggests that the Mott insulator is related to the single particle energy gap. As discussed in chapter 3, this large gap is bounded by the phase winding of the small ring states, and the gap is precisely confined by the two states with a ring at the symmetry center of the system $\mathbf{r} = 0$ with winding $m = 2$ and $m = 3$. To further understand the appearance of the Mott insulator phase in this quasicrystal system, we calculate the particle number density profiles for various chemical potentials for bosons with $\tilde{g}_0 = 5$ and temperature $T = 0.02 E_r$ in the quasicrystal potential. We plotted differences of particle number density distribution for different chemical potentials, see Fig. 4.17 and Fig. 4.18. The figures show the particle number density profiles of newly populated regions when the chemical potential is slightly increased. The chemical potential successively moves across the Mott insulator phase from small $\mu$ to large $\mu$ in Fig. 4.17 and Fig. 4.18. We can observe that the particles populate the centered small ring immediately before the bosons enter the Mott insulator phase, see the third row of Fig. 4.17. Then as chemical potential further increases, the bosons are in the Mott insulator phase and the plotted density profiles differences only have some background noise, see the fourth row of Fig. 4.17 and the first row of Fig. 4.18, until the bosons leave the Mott insulator phase, and note that here again the particles first populate the centered small ring immediately after the Mott insulator phase, see the second row of Fig. 4.18. Integrating the local density $n(\mathbf{r})$ in a small square with linear size $2a$ around the center ring, we get approximately the number of particles that are accomodated by the center ring, see Fig. 4.19. We see that in the range of chemical potential in the Mott insulator phase, the

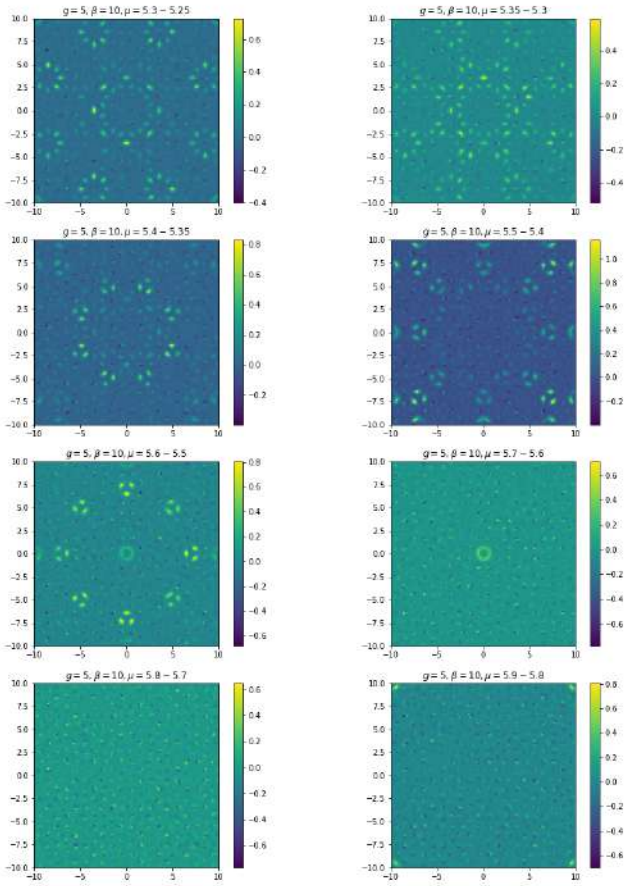


Figure 4.17: Particle number density differences for nearby chemical potentials, representing the newly populated particles as chemical potential increase. The parameters are $\tilde{g}_0 = 5, T = 0.02E_r, L = 20a$. The chemical potentials run across the Mott insulator phase. The value of $\mu$ in the subtitle means what is plotted is the particle number density difference for the two chemical potentials. For example, $\mu = 5.3 - 5.25$ means the plot shows the difference $n(\mathbf{r}, \mu = 5.3E_r) - n(\mathbf{r}, \mu = 5.25E_r)$.

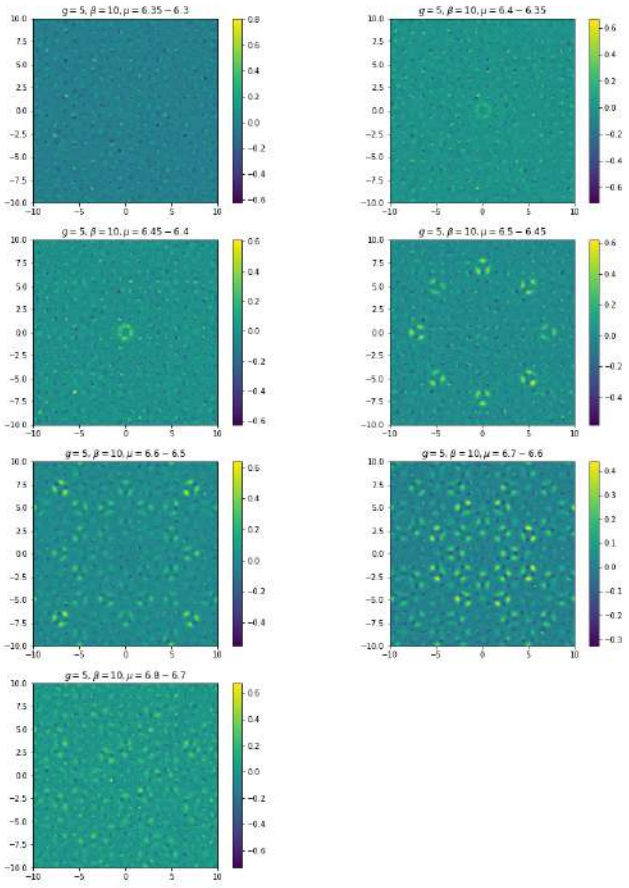


Figure 4.18: Particle number density differences for nearby chemical potentials, representing the newly populated particles as chemical potential increases. The parameters are $\tilde{g}_0 = 5, T = 0.02E_r, L = 20a$. The chemical potentials run across the Mott insulator phase. The value of $\mu$ in the subtitle means what is plotted is the particle number density difference for the two chemical potentials. For example, $\mu = 5.3 - 5.25$ means the plot shows the difference $n(\mathbf{r}, \mu = 5.3E_r) - n(\mathbf{r}, \mu = 5.25E_r)$.

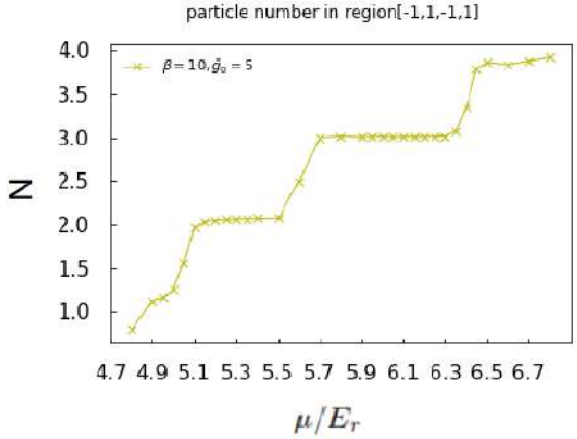


Figure 4.19: Total particle number in the square with linear size $2a$ around the system center $\mathbf{r} = 0$, obtained by taking integration of local density $n(\mathbf{r})$ in the area.

particle number in the center ring has a plateau of 3 particles.

This strongly suggests that the Mott insulator phase may be connected to the small ring states, just like the large gap in the single particle spectrum. However, the reason of this phenomenon remains to be further clarified.

### 4.10.2 Nature of BG-SF transition

The behaviour of the BG-SF transition of 2D bosons in the quasicrystal, obtained from our QMC calculations, are quite similar to the BKT superfluid transition for 2D bosons in homogeneous space. It may be interesting to study more carefully the nature of the BG-SF phase transition. Figure 4.20 shows the QMC results for the rescaled susceptibility $\chi/L^{7/4}$ for quasicrystal system with different sizes. The curves of $\chi/L^{7/4}$ with different system sizes show crossing behaviour similar to what is observed for homogeneous systems as in Fig. 4.4, Fig. 4.6 and Fig. 4.7, but the crossing point is not that sharp for quasicrystal system. This may be due to fluctuations against system sizes which we observed for quasicrystal potential, and these fluctuations complicate a systematic study over the nature of BG-SF transitions.

## 4.11 Conclusions

In conclusion, we have established the thermodynamic phase diagrams of weakly to strongly interacting 2D bosons in a quasicrystalline potential. The quantum phases have been obtained analyzing finite-size effects and systematically distinguished from the NF regime. Our results show the emergence of a

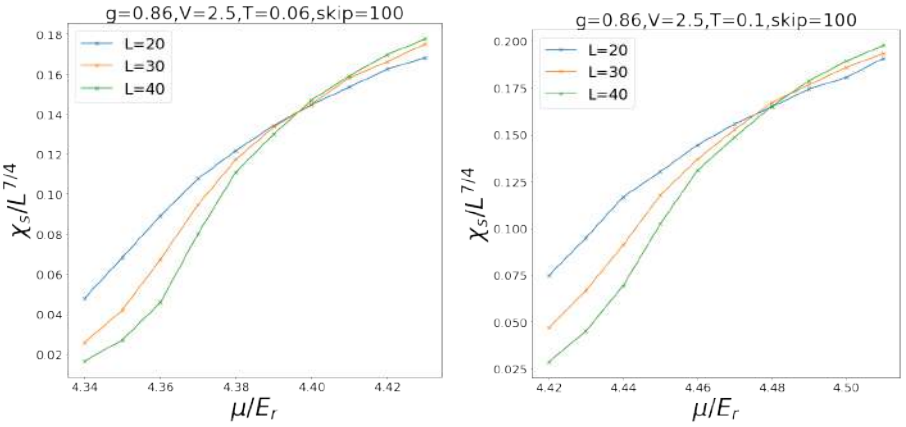


Figure 4.20: Rescaled susceptibility $\chi/L^{7/4}$ for 2D bosons in the quasicrystal system with $V_0 = 2.5E_r$. Interaction strength is $\tilde{g}_0 = 0.86$ and system sizes are $L = 20a, 30a, 40a$. The temperature is $T = 0.06E_r$ (left) and $T = 0.1E_r$ (right).

sizable BG phase induced by the quasicrystalline potential. For the parameters used here, the BG extends over a range where the density typically varies by a factor from 2 to 4 in all phase diagrams of Fig. 4.2, where the considered temperatures are relevant for ultracold-atom experiments. This paves the way to the direct observation of the BG in ultracold-atom quantum simulators. For example, for $^{39}K$ potassium atoms in an optical lattice with laser wavelength $\lambda_{lat} = 725nm$, a temperature $T = 0.1E_r$ corresponds to $47nK$, relevant for typical cold atoms experiments. Moreover, further calculations for higher temperatures show that the BG phase survives up to $T \simeq 8E_{\rm r}/k_{\rm B}$ for $\tilde{g}_0 = 0.05$, $T \simeq 0.7E_{\rm r}/k_{\rm B}$ for $\tilde{g}_0 = 0.86$, and $T \simeq 0.5E_{\rm r}/k_{\rm B}$ for $\tilde{g}_0 = 5$.

Our results would directly apply to experiments performed in optical boxes [180–182]. For experiments performed in confining traps, our diagrams, found versus chemical potential, are amenable to local density approximation (LDA). It applies provided the variation of the trap potential is negligible over a large enough distance such that the finite size effects become insignificant. Our results show that a size $L \sim 40a$ is a minimum. For the parameters of Refs. [47, 49] for instance, it corresponds to a variation of $\simeq 0.01E_r$ from the trap center, smaller than the typical energy scales in our phase diagrams, and LDA is well applicable.

Moreover, our work raises new questions, notably about the detailed mechanism of the formation of MI phase and the nature of the SF-to-BG transition. Our results for SF-to-BG transition are phenomenologically similar to a BKT transition, but the exact mechanism at the origin of the transition, as well as the effect of the quasicrystal potential on vortex pairing remain to be elucidated, via quantum simulation experiments and theoretical work.

# Chapter 5

# Conclusions and perspectives

In this thesis, we study the quantum simulation of quasicrystals with cold atoms. The single particle properties are discussed with energies and wavefunctions of single particle eigenstates obtained by exact diagonalization numerical calculations. Based on these data, we have analysed the localization and spectral properties of quasicrystal potentials. We have identified different kinds of states by looking at how their IPR scales with system size $L$. For scaling IPR $\sim L^0$, we get localized states; for scaling IPR $\sim L^{-2}$, we get extended states. In addition, we have observed states with IPR scaling that is neither IPR $\sim L^0$ or IPR $\sim L^{-2}$. These are the critical states. Localized states have low energies, and are localized in one or a finite number of potential wells. The extended states have high energies and typically cover the full system. Critical states appear in the intermediate energy ranges, with wavefunctions showing interesting geometrical structures. On the spectral properties, we put special focus on the largest gap, which is related to the Mott insulator phase for strongly interacting bosons in the quasicrystal potential. We have shown that the gaps are bounded by two states that are very special: they are located at the symmetry center of the whole potential. They have ring structures and are localized in a nearly isotropic annular potential well. We have developed a theoretical model for these ring states, agreeing well with the numerical data. The states with energies near the largest gap also display ring structures, which are just off-centered ring states. The ring states can be classified according to the phase winding number $m$. We have analysed the energies of these off-centered ring states with perturbation theory. In particular, we have shown that for ring states with a phase winding number difference $\pm 3$, the perturbation coupling due to the potential deformation has a resonance effect. This results in the level repelling and explains why the gap exists. We have also shown the general spectrum pattern for quasicrystal potentials with other rotational symmetries. For some cases, the ring states also play some special roles. However, as the number of laser beams to create the potential increases, the gaps, at least the large ones, tend to disappear.

For interacting two dimensional bosons in the quasicrystal potential, we have

used quantum Monte Carlo methods to calculate various physical observables. We use the superfluid fraction $f_s$ and compressibility $\kappa$ as order parameters to identify the superfluid and Mott insulator phases. For the Bose glass and normal fluids, which are both compressible insulators, we give a method to differentiate them by comparing the Bose gas with and without the quasicrystal potential. For bosons in homogeneous systems, we have shown that our QMC data agree well with the theoretical expectation. We get the BKT transition points for 2D bosons in homogeneous systems from weak to strong interactions. We then discuss the bosons in the quasicrystal potential, in particular the fermionization phenomenon. We argued that to get a reliable thermodynamic phase diagram, a careful finite size analysis is indispensable, which was complicated by the quasicrystal potential. With all these precautions, we study and locate the transition from Bose glass to superfluid, as well as the boundary between Bose glass and normal fluid. For strong interaction, the Mott insulator phase appears. The large Mott insulator plateau shows a particle number density at the same value as the plateau of the Fermi-Dirac distribution, obtained from the single particle spectrum of the quasicrystal potential. This indicates that the Mott phase may be related to the single particle gap.

Our works raise some new questions, which may be interesting for future research. On the single particle side, we may wonder whether it is possible to build a model to explain why and when the critical states appear. Can we predict the energies of the critical states? For the gap structure, we realized the special roles played by the ring states. Again, how general is this picture? Do we have similar ring states, or some equivalents of ring states, in other kinds of quasicrystal potentials? Our resolution of the gaps is limited by the system sizes that are reachable in our exact diagonalization calculations. Mathematically, if the energy resolution is infinitely high, will we get a spectrum with some kind of fractal structure or not? In a Penrose lattice, some works [183–187] have shown that the single particle spectrum have some similar tastes as the one I obtained for the shallow optical quasicrystal potential. For example, for a single particle tight-binding model on a Penrose lattice with constant on-site energy and constant hopping term between all the nearest neighbours [183], it has been shown that the density of states has a peak at zero energy while these zero energy states are all localized, and all the other states are separated from these zero energy states by a finite gap. Then for a tight-binding model on a Penrose lattice with a particular on-site potential landscape, it has been shown that the ground state wavefunction is self-similar. It would be interesting to see whether the results I obtained, like the gap bounded by the ring states, are in some sense related to the results in the Penrose latiice.

For the thermodynamic phase diagrams of interacting bosons, a first question is the nature of the Mott insulator phase. We may try to explain the value of its chemical potential width. In particular, is this width governed by the single particle gap or the interactions? It would be interesting to do calculations with different potential amplitude $V_0$ and interaction strength $\tilde{g}_0$, and see how the Mott phase varies with these parameters. We see that there is no Mott phase for $\tilde{g}_0 = 0.86$ but there is the Mott phase for $\tilde{g}_0 = 5$. We may ask at

which interaction strength the Mott phase starts to appear, and how does its width vary with interaction. Does the width always increase with increasing $\tilde{g}_0$? For different $V_0$, does the Mott width saturate at a large $V_0$ or not? In practice, can we always reproduce this Mott insulator by doing a calculation in a smaller system containing the center ring? If that's the case, we may be able to study this Mott phase with much cheaper calculations. The transition between Bose glass and superfluid also leaves certain questions. We may study whether the transtion we observed is still the standard BKT transition for 2D bosons. If the chemical potential is very high, much larger than the average quasicrystal potential, then intuitively we may expect a BKT behaviour persists as the quasicrystal potential is strongly dominated by the kinetic and interaction energies and may only perturb the bosons. However, in our case, the transition chemical potential is by no means higher than the quasicrystal potential, so we may need to have a careful study of whether the transition is of the BKT type. For this, we may look at the one-body correlation function $g(r)$. A characteristic of BKT transition is that at the critical point $g(r)$ has an algebraic decay as $g(r) \sim r^{-1/4}$, and once the bosons enter the normal fluid phase, $g(r)$ has an exponential decay. So a scaling of $g(r) \sim r^{\eta}$ with $\eta$ between $-1/4$ and 0 cannot be observed. This may be used to check whether the transition is BKT or not. However, as quasicrystal systems has no translational symmetry, certain kinds of averages is needed to have a correlation function $g(r)$ that only depends on one variable. This may introduce some fluctuation of the results and we may need to have some smart ways to interpret the data. In addition, we can further try to study how the localization interplays with the vortex/anti-vortex pairing mechanism.

# Acknowledgements

> "All theory, dear friend, is grey, but the golden tree of actual life springs ever green."
>
> Johann Wolfgang von Goethe, Faust

A PhD study has two sides. One side of it is impersonalized, being a little wave in the long river of scientific advancements in the history of human civilization. All scientists, or more generally, all human beings exploring the nature of the world, give their contributions to this long river of science. Sooner or later, these human beings will perish, the personal traces of their work will be washed out by the history, and what will remain are the impersonalized advancements on the truth of nature. The river is ever-flowing, and compared to it, the little wave of a PhD work may be really negligible. On the other side, a PhD work is done by someone in real life, which takes a few years time. Lift is short and these years are by no means negligible in the personal life history. It is filled with happiness, pains, excitements, frustrations,..., with all the personalized feelings and experiences. While the main body of the thesis is devoted to the first side of my PhD work, it is a convention to embark on the second side in the acknowledgement part of the thesis.

My PhD research is supervised by Laurent Sanchez-Palencia, and I would express my great thanks to him. I have really learned a lot during all the discussions and works with him. He always sees through all the superficial aspects and directly targets the underlying physics right at the point. Facing a physics problem, he just sees it as how it is. This may sound a bit trivial at a first glance, but in my opinion, this is really not trivial at all (in some sense, this is the highest goal of science). On the other hand, modern scientific research is not just 'eureka' times of individuals, but also systematic projects, done in a research group. Laurent always has a very organized picture over the proceeds of the project. Each time after I discuss with him, I have a much clearer mind on what I should do next. I have been often amazed by how well he can organize the results we have obtained and point out the next step direction accordingly. And the next steps he suggested are always concrete doable tasks rather than just big directions, such that I can readily get on the rail and progress, without wandering about how to proceed. Needless to say, he has so clear arrangements of the research project just because of his deep understanding of the physics.

Laurent is not just the project's supervisor for me, but also helps me and guides me on many things in my life, which I am unable to give a complete list.

I would also like to thank all my colleagues during my PhD. I am grateful to Hepeng Yao, who guided me on the quantum Monte Carlo codes, Jan Schneider, who is an encyclopedia type of person and has a lot of knowledge over all sorts of things (including physics of course), Dean Johnstone, who is always earnest and committed towards research work, Erik Linner, a very talkative Swedish guy who is also a good organizer of seminars. I am grateful to Jie Xiong, Shengjie Yu, Xiaoxu Zhou, Yilin Ye, Tingwen Guo, with whom I have many delightful and enlightening talks, on physics and also on various topics, not only in the office, but also during the dinners in Magnan or Crous, and during the Ping Pong exercises in the CPHT courtyard. I am a person who likes to raise random questions appearing in my mind, and though these questions may not be always solved, the discussions and talks are always inspiring. And I want to say thanks to all my colleagues at CPHT, making CPHT a very convivial place to work. I have done my research happily in this friendly and lively environment.

I am very grateful to the administrative department and IT supports at CPHT. I want to say thanks to the secretaries, Florence Auger, Malika Lang, Fadila Debbou. In particular, for the invaluable help, together with Laurent, over my issue of the resident card, which had been a long-term energy-consuming nightmare and a great crisis during my PhD. I could not imagine how the situation would be without these helps.

I want to thank Marcel Filoche and Patrik Öhberg for being the referees of my thesis, and Anuradha Jagannathan, Patrizia Vignolo, Nicolas Dupuis for being the examinators.

I am deeply grateful for all the people who accompany me, help me, guide me on my journey of science, which could be long but also enjoyable.

> "Man should honor himself and consider himself worthy of the highest. He cannot overestimate the greatness and power of the spirit; the closed essence of the universe contains no force which could withstand the courage of cognition; it must open up before it, and afford it the spectacle and enjoyment of its riches and its depths."
>
> Hegel, Inaugural address delivered at the University of Berlin

# Bibliography


[1] D. Shechtman, I. Blech, D. Gratias, and J. W. Cahn, *Metallic phase with long-range orientational order and no translational symmetry*, Phys. Rev. Lett. **53**, 1951 (1984).

[2] M. Senechal, *Quasicrystals and geometry* (Cambridge University press, UK, 1995).

[3] W. Steurer, *Quasicrystals: What do we know? What do we want to know? What can we know?*, Acta Cryst. Sec. A: Found. Adv. **74**, 1 (2018).

[4] K. Edagawa, K. Suzuki, and S. Takeuchi, *High resolution transmission electron microscopy observation of thermally fluctuating phasons in decagonal Al–Cu–Co*, Phys. Rev. Lett. **85**, 1674 (2000).

[5] J. E. S. Socolar, T. C. Lubensky, and P. J. Steinhardt, *Phonons, phasons, and dislocations in quasicrystals*, Phys. Rev. B **34**, 3345 (1986).

[6] P. A. Bancel, *Dynamical phasons in a perfect quasicrystal*, Phys. Rev. Lett. **63**, 2741 (1989).

[7] K. Kamiya, T. Takeuchi, N. Kabeya, N. Wada, T. Ishimasa, A. Ochiai, K. Deguchi, K. Imura, and N. Sato, *Discovery of superconductivity in quasicrystal*, Nat. Comm. **9**, 1 (2018).

[8] D. Mayou, C. Berger, F. Cyrot-Lackmann, T. Klein, and P. Lanco, *Evidence for unconventional electronic transport in quasicrystals*, Phys. Rev. Lett. **70**, 3915 (1993).

[9] S. J. Ahn, P. Moon, T.-H. Kim, H.-W. Kim, H.-C. Shin, E. H. Kim, H. W. Cha, S.-J. Kahng, P. Kim, M. Koshino, *et al.*, *Dirac electrons in a dodecagonal graphene quasicrystal*, Science **361**, 782 (2018).

[10] W. Yao, E. Wang, C. Bao, Y. Zhang, K. Zhang, K. Bao, C. K. Chan, C. Chen, J. Avila, M. C. Asensio, *et al.*, *Quasicrystalline 30° twisted bilayer graphene as an incommensurate superlattice with strong interlayer coupling*, Proc. Nat. Acad. Sci. **115**, 6928 (2018).

[11] T. S. Cubitt, D. Perez-Garcia, and M. M. Wolf, *Undecidability of the spectral gap*, Nature (London) **528**, 207 (2015).

[12] T. Fujiwara, S. Yamamoto, and G. Trambly de Laissardière, *Band structure effects of transport properties in icosahedral quasicrystals*, Phys. Rev. Lett. **71**, 4166 (1993).

[13] T. Odagaki and D. Nguyen, *Electronic and vibrational spectra of two-dimensional quasicrystals*, Phys. Rev. B **33**, 2184 (1986).

[14] L.-J. Lang, X. Cai, and S. Chen, *Edge states and topological phases in one-dimensional optical superlattices*, Phys. Rev. Lett. **108**, 220401 (2012).

[15] Y. E. Kraus and O. Zilberberg, *Topological equivalence between the Fibonacci quasicrystal and the Harper model*, Phys. Rev. Lett. **109**, 116404 (2012).

[16] Y. E. Kraus, Z. Ringel, and O. Zilberberg, *Four-dimensional quantum Hall effect in a two-dimensional quasicrystal*, Phys. Rev. Lett. **111**, 226401 (2013).

[17] A. Dareau, E. Levy, M. B. Aguilera, R. Bouganne, E. Akkermans, F. Gerbier, and J. Beugnon, *Revealing the topology of quasicrystals with a diffraction experiment*, Phys. Rev. Lett. **119**, 215304 (2017).

[18] H. Huang and F. Liu, *Quantum spin Hall effect and spin Bott index in a quasicrystal lattice*, Phys. Rev. Lett. **121**, 126401 (2018).

[19] S. Aubry and G. André, *Analyticity breaking and Anderson localization in incommensurate lattices*, Ann. Israel Phys. Soc. **3**, 133 (1980).

[20] G. Roati, C. D'Errico, L. Fallani, M. Fattori, C. Fort, M. Zaccanti, G. Modugno, M. Modugno, and M. Inguscio, *Anderson localization of a non-interacting Bose-Einstein condensate*, Nature (London) **453**, 895 (2008).

[21] R. P. Feynman, *Simulating physics with computers*, Int. J. Theor. Phys. **21**(6-7), 467 (1982).

[22] I. Buluta and F. Nori, *Quantum simulators*, Science **326**(5949), 108 (2009).

[23] I. M. Georgescu, S. Ashhab, and F. Nori, *Quantum simulation*, Rev. Mod. Phys. **86**, 153 (2014).

[24] M. H. Anderson, J. R. Ensher, M. R. Matthews, C. E. Wieman, and E. A. Cornell, *Observation of Bose-Einstein condensation in a dilute atomic vapor*, Science **269**(5221), 198 (1995).

[25] K. B. Davis, M. O. Mewes, M. R. Andrews, N. J. Van Druten, D. S. Durfee, D. M. Kurn, and W. Ketterle, *Bose-Einstein condensation in a gas of sodium atoms*, Phys. Rev. Lett. **75**(22), 3969 (1995).

[26] I. Bloch, J. Dalibard, and W. Zwerger, *Many-body physics with ultracold gases*, Rev. Mod. Phys. **80**, 885 (2008).

[27] I. Bloch, J. Dalibard, and S. Nascimbène, *Quantum simulations with ultracold quantum gases*, Nat. Phys. **8**(2), 267 (2012).

[28] R. Roth and K. Burnett, *Phase diagram of bosonic atoms in two-color superlattices*, Phys. Rev. A **68**, 023604 (2003).

[29] B. Damski, J. Zakrzewski, L. Santos, P. Zoller, and M. Lewenstein, *Atomic Bose and Anderson glasses in optical lattices*, Phys. Rev. Lett. **91**, 080403 (2003).

[30] L. Fallani, J. E. Lye, V. Guarrera, C. Fort, and M. Inguscio, *Ultracold atoms in a disordered crystal of light: Towards a Bose glass*, Phys. Rev. Lett. **98**, 130404 (2007).

[31] T. Roscilde, *Bosons in one-dimensional incommensurate superlattices*, Phys. Rev. A **77**, 063605 (2008).

[32] G. Roux, T. Barthel, I. P. McCulloch, C. Kollath, U. Schollwöck, and T. Giamarchi, *Quasiperiodic Bose-Hubbard model and localization in one-dimensional cold atomic gases*, Phys. Rev. A **78**, 023628 (2008).

[33] B. Gadway, D. Pertot, J. Reeves, M. Vogt, and D. Schneble, *Glassy behavior in a binary atomic mixture*, Phys. Rev. Lett. **107**, 145306 (2011).

[34] C. D'Errico, E. Lucioni, L. Tanzi, L. Gori, G. Roux, I. P. McCulloch, T. Giamarchi, M. Inguscio, and G. Modugno, *Observation of a disordered bosonic insulator from weak to strong interactions*, Phys. Rev. Lett. **113**, 095301 (2014).

[35] L. Gori, T. Barthel, A. Kumar, E. Lucioni, L. Tanzi, M. Inguscio, G. Modugno, T. Giamarchi, C. D'Errico, and G. Roux, *Finite-temperature effects on interacting bosonic one-dimensional systems in disordered lattices*, Phys. Rev. A **93**, 033650 (2016).

[36] F. A. An, E. J. Meier, and B. Gadway, *Engineering a flux-dependent mobility edge in disordered zigzag chains*, Phys. Rev. X **8**, 031045 (2018).

[37] F. A. An, K. Padavić, E. J. Meier, S. Hegde, S. Ganeshan, J. H. Pixley, S. Vishveshwara, and B. Gadway, *Interactions and mobility edges: Observing the generalized Aubry-André model*, Phys. Rev. Lett. **126**, 040603 (2021).

[38] H. Yao, H. Khoudli, L. Bresque, and L. Sanchez-Palencia, *Critical behavior and fractality in shallow one-dimensional quasiperiodic potentials*, Phys. Rev. Lett. **123**, 070405 (2019).

[39] H. Yao, T. Giamarchi, and L. Sanchez-Palencia, *Lieb-Liniger bosons in a shallow quasiperiodic potential: Bose glass phase and fractal Mott lobes*, Phys. Rev. Lett. **125**, 060401 (2020).

[40] S. Lellouch and L. Sanchez-Palencia, *Localization transition in weakly-interacting Bose superfluids in one-dimensional quasiperdiodic lattices*, Phys. Rev. A **90**, 061602(R) (2014).

[41] S. Iyer, V. Oganesyan, G. Refael, and D. A. Huse, *Many-body localization in a quasiperiodic system*, Phys. Rev. B **87**, 134202 (2013).

[42] M. Schreiber, S. S. Hodgman, P. Bordia, H. P. Lüschen, M. H. Fischer, R. Vosk, E. Altman, U. Schneider, and I. Bloch, *Observation of many-body localization of interacting fermions in a quasi-random optical lattice*, Science **349**, 842 (2015).

[43] V. Khemani, D. N. Sheng, and D. A. Huse, *Two universality classes for the many-body localization transition*, Phys. Rev. Lett. **119**, 075702 (2017).

[44] T. Kohlert, S. Scherg, X. Li, H. P. Lüschen, S. Das Sarma, I. Bloch, and M. Aidelsburger, *Observation of many-body localization in a one-dimensional system with a single-particle mobility edge*, Phys. Rev. Lett. **122**, 170403 (2019).

[45] T. Liu, X. Xia, S. Longhi, and L. Sanchez-Palencia, *Anomalous mobility edges in one-dimensional quasiperiodic models*, SciPost Phys. **12**, 27 (2022).

[46] L. Sanchez-Palencia and L. Santos, *Bose-Einstein condensates in optical quasicrystal lattices*, Phys. Rev. A **72**, 053607 (2005).

[47] K. Viebahn, M. Sbroscia, E. Carter, J.-C. Yu, and U. Schneider, *Matter-wave diffraction from a quasicrystalline optical lattice*, Phys. Rev. Lett. **122**, 110404 (2019).

[48] A. Jagannathan and M. Duneau, *An eightfold optical quasicrystal with cold atoms*, Europhys. Lett. **104**, 66003 (2013).

[49] M. Sbroscia, K. Viebahn, E. Carter, J.-C. Yu, A. Gaunt, and U. Schneider, *Observing localization in a 2D quasicrystalline optical lattice*, Phys. Rev. Lett. **125**, 200604 (2020).

[50] D. Johnstone, P. Öhberg, and C. W. Duncan, *Mean-field phases of an ultracold gas in a quasicrystalline potential*, Phys. Rev. A **100**, 053609 (2019).

[51] D. Johnstone, P. Öhberg, and C. W. Duncan, *The mean-field Bose glass in quasicrystalline systems*, J. Phys. A: Math. Theor. **54**, 395001 (2021).

[52] R. Gautier, H. Yao, and L. Sanchez-Palencia, *Strongly interacting bosons in a two-dimensional quasicrystal lattice*, Phys. Rev. Lett. **126**, 110401 (2021).

[53] T. Giamarchi and H. J. Schulz, *Localization and interactions in one-dimensional quantum fluids*, Europhys. Lett. **3**, 1287 (1987).

[54] M. P. A. Fisher, P. B. Weichman, G. Grinstein, and D. S. Fisher, *Boson localization and the superfluid-insulator transition*, Phys. Rev. B **40**(1), 546 (1989).

[55] D. Pines and P. Nozieres, *Quantum liquids* (Benjamin, New York, 1966).

[56] L. D. Landau and E. M. Lifshitz, *Statistical Physics, parts 1 and 2* (Elsevier, Oxford, UK, 1980).

[57] A. A. Abrikosov, L. P. Gor'kov, and I. Y. Dzyaloshinskii, *Methods of Quantum Field Theory in Statistical Physics* (Dover publications, 1975).

[58] P. W. Anderson, *Concepts in solids: lectures on the theory of solids*, vol. 58 (World Scientific, 1997).

[59] L. P. Pitaevskii and S. Stringari, *Bose-Einstein Condensation* (Clarendon press, Oxford, 2004).

[60] J. Bardeen, L. Cooper, and J. Schrieffer, *Theory of superconductivity*, Phys. Rev. **108**, 1175 (1957).

[61] B. DeMarco and D. S. Jin, *Onset of Fermi degeneracy in a trapped atomic gas*, Science **285**(5434), 1703 (1999).

[62] G. Modugno, G. Roati, F. Riboli, F. Ferlaino, R. J. Brecha, and M. Inguscio, *Collapse of a degenerate Fermi gas.*, Science **297**(5590), 2240 (2002).

[63] A. G. Truscott, K. E. Strecker, W. I. McAlexander, G. B. Partridge, and R. G. Hulet, *Observation of Fermi pressure in a gas of trapped atoms*, Science **291**(5513), 2570 (2001).

[64] F. Schreck, L. Khaykovich, K. L. Corwin, G. Ferrari, T. Bourdel, J. Cubizolles, and C. Salomon, *Quasipure Bose-Einstein condensate immersed in a Fermi sea*, Phys. Rev. Lett. **87**(8), 4 (2001).

[65] P. S. Jessen and I. H. Deutsch, *Optical lattices*, Adv. At. Mol. Opt. Phys. **37**, 95 (1996).

[66] G. Grynberg and C. Robilliard, *Cold atoms in dissipative optical lattices*, Phys. Rep. **355**(5-6), 335 (2001).

[67] L. Guidoni, C. Triché, P. Verkerk, and G. Grynberg, *Quasiperiodic optical lattices*, Phys. Rev. Lett. **79**, 3363 (1997).

[68] L. Guidoni, B. Dépret, A. di Stefano, and P. Verkerk, *Atomic diffusion in an optical quasicrystal with five-fold symmetry*, Phys. Rev. A **60**(6), R4233 (1999).

[69] S. Inouye, M. R. Andrews, J. Stenger, H. J. Miesner, D. M. Stamper-Kurn, and W. Ketterle, *Observation of Feshbach resonances in a Bose-Einstein condensate*, Nature (London) **392**(6672), 151 (1998).

[70] S. L. Cornish, N. R. Claussen, J. L. Roberts, E. A. Cornell, and C. E. Wieman, *Stable $^{85}$Rb Bose-Einstein condensates with widely tunable interactions*, Phys. Rev. Lett. **85**(9), 1795 (2000).

[71] M. Greiner, O. Mandel, T. Esslinger, T. W. Hänsch, and I. Bloch, *Quantum phase transition from a superfluid to a Mott insulator in a gas of ultracold atoms*, Nature (London) **415**(6867), 39 (2002).

[72] T.-L. Ho, *Universal thermodynamics of degenerate quantum gases in the unitarity limit*, Phys. Rev. Lett. **92**, 090402 (Mar 2004).

[73] H. Hu, P. D. Drummond, and X.-J. Liu, *Universal thermodynamics of strongly interacting fermi gases*, Nature Physics **3**(7), 469 (2007).

[74] M. J. Ku, A. T. Sommer, L. W. Cheuk, and M. W. Zwierlein, *Revealing the superfluid lambda transition in the universal thermodynamics of a unitary Fermi gas*, Science **335**, 563 (2012).

[75] S. Nascimbène, N. Navon, K. Jiang, F. Chevy, and C. Salomon, *Exploring the thermodynamics of a universal Fermi gas*, Nature (London) **463**(7284), 1057 (2010).

[76] M. Greiner, C. A. Regal, and D. S. Jin, *Emergence of a molecular Bose-Einstein condensate from a fermi gas*, Nature (London) **426**(6966), 537 (2003).

[77] S. Jochim, M. Bartenstein, A. Altmeyer, G. Hendl, S. Riedl, C. Chin, J. Hecker Denschlag, and R. Grimm, *Bose-Einstein condensation of molecules*, Science **302**(5653), 2101 (2003).

[78] M. W. Zwierlein, C. A. Stan, C. H. Schunck, S. M. F. Raupach, S. Gupta, Z. Hadzibabic, and W. Ketterle, *Observation of Bose-Einstein condensation of molecules*, Phys. Rev. Lett. **91**(25), 4 (2003).

[79] T. Bourdel, L. Khaykovich, J. Cubizolles, J. Zhang, F. Chevy, M. Teichmann, L. Tarruell, S. J. J. M. F. Kokkelmans, and C. Salomon, *Experimental study of the BEC-BCS crossover region in Lithium 6*, Phys. Rev. Lett. **93**(5), 050401 (2004).

[80] A. Einstein, *Über die von der molekularkinetischen Theorie der Wärme geforderte Bewegung von in ruhenden Flüssigkeiten suspendierten Teilchen*, Annalen der Physik **322**(8), 549 (1905).

[81] P. W. Anderson, *Absence of diffusion in certain random lattices*, Phys. Rev. **109**, 1492 (1958).

[82] C. Cohen-Tannoudji and D. Guéry-Odelin, *Advances in atomic physics: an overview* (World Scientific, 2011).

[83] S. Chu, L. Hollberg, J. E. Bjorkholm, A. Cable, and A. Ashkin, *Three-dimensional viscous confinement and cooling of atoms by resonance radiation pressure*, Phys. Rev. Lett. **55**, 48 (1985).

[84] W. D. Phillips, *Nobel lecture: Laser cooling and trapping of neutral atoms*, Rev. Mod. Phys. **70**(3), 721 (1998).

[85] J. Dalibard and C. Cohen-Tannoudji, *Laser cooling below the Doppler limit by polarization gradients: Simple theoretical models*, J. Opt. Soc. Am. B **6**(11), 2023 (1989).

[86] P. J. Ungar, D. S. Weiss, E. Riis, and S. Chu, *Optical molasses and multilevel atoms: Theory*, J. Opt. Soc. Am. B **6**(11), 2058 (1989).

[87] J. Dalibard (1987), helsinki workshop on laser manipulation of atoms.

[88] E. Raab, M. Prentiss, A. Cable, S. Chu, and D. Pritchard, *Trapping of neutral sodium atoms with radiation pressure*, Phys. Rev. Lett. **59**, 2631 (1987).

[89] D. Sesko, T. Walker, C. Monroe, A. Gallagher, and C. Wieman, *Collisional losses from a light-force atom trap*, Phys. Rev. Lett. **63**, 961 (1989).

[90] H. J. Metcalf and P. van der Straten, *Laser Cooling and Trapping* (Spinger, Berlin, 2001).

[91] S. Chu, *Nobel lecture: The manipulation of neutral particles*, Rev. Mod. Phys. **70**(3), 685 (1998).

[92] C. N. Cohen-Tannoudji, *Nobel lecture: Manipulating atoms with photons*, Rev. Mod. Phys. **70**(3), 707 (1998).

[93] E. A. Cornell and C. E. Wieman, *Nobel lecture: Bose-Einstein condensation in a dilute gas, the first 70 years and some recent experiments*, Rev. Mod. Phys. **74**(3), 875 (2002).

[94] W. Ketterle, *Nobel lecture: When atoms behave as waves: Bose-Einstein condensation and the atom laser*, Rev. Mod. Phys. **74**(4), 1131 (2002).

[95] C. Chin, R. Grimm, P. Julienne, and E. Tiesinga, *Feshbach resonances in ultracold gases*, Rev. Mod. Phys. **82**, 1225 (2010).

[96] M. Ben Dahan, E. Peik, J. Reichel, Y. Castin, and C. Salomon, *Bloch oscillations of atoms in an optical potential*, Phys. Rev. Lett. **76**(24), 4508 (1996).

[97] E. Peik, M. Ben Dahan, I. Bouchoule, Y. Castin, and C. Salomon, *Bloch oscillations of atoms, adiabatic rapid passage, and monokinetic atomic beams*, Phys. Rev. A **55**(4), 2989 (1997).

[98] D. Jaksch, C. Bruder, J. I. Cirac, C. W. Gardiner, and P. Zoller, *Cold bosonic atoms in optical lattices*, Phys. Rev. Lett. **81**(15), 3108 (1998).

[99] A. J. Leggett, *Quantum Liquids* (Oxford University Press, Oxford, UK, 2006).

[100] `http://web.archive.org/web/20080207010024/http://www.808multimedia.com/winnt/kernel.htm`, accessed: 2023-11-05.

[101] `https://medium.com/@adubey40/classical-bit-vs-qubit-fa6c6c06e8f`, accessed: 2023-11-05.

[102] M. Lewenstein, A. Sanpera, V. Ahufinger, B. Damski, A. Sen, and U. Sen, *Ultracold atomic gases in optical lattices: Mimicking condensed matter physics and beyond*, Adv. Phys. **56**, 243 (2007).

[103] C. A. Regal, M. Greiner, and D. S. Jin, *Observation of resonance condensation of fermionic atom pairs*, Phys. Rev. Lett. **92**(4), 040403 (2004).

[104] J. Dalibard, F. Gerbier, G. Juzeliūnas, and P. Öhberg, *Colloquium: Artificial gauge potentials for neutral atoms*, Rev. Mod. Phys. **83**, 1523 (2011).

[105] J. Simon, W. S. Bakr, R. Ma, M. E. Tai, P. M. Preiss, and M. Greiner, *Quantum simulation of antiferromagnetic spin chains in an optical lattice*, Nature **472**(7343), 307 (2011).

[106] J. E. Lye, L. Fallani, M. Modugno, D. S. Wiersma, C. Fort, and M. Inguscio, *Bose-Einstein condensate in a random potential*, Phys. Rev. Lett. **95**(7), 070401 (2005).

[107] C. Fort, L. Fallani, V. Guarrera, J. E. Lye, M. Modugno, D. S. Wiersma, and M. Inguscio, *Effect of optical disorder and single defects on the expansion of a Bose-Einstein condensate in a one-dimensional waveguide*, Phys. Rev. Lett. **95**(17), 170410 (2005).

[108] T. Schulte, S. Drenkelforth, J. Kruse, W. Ertmer, J. Arlt, K. Sacha, J. Zakrzewski, and M. Lewenstein, *Routes towards Anderson-like localization of Bose-Einstein condensates in disordered optical lattices*, Phys. Rev. Lett. **95**(17), 170411 (2005).

[109] D. Clément, A. F. Varón, M. Hugbart, J. A. Retter, P. Bouyer, L. Sanchez-Palencia, D. M. Gangardt, G. V. Shlyapnikov, and A. Aspect, *Suppression of transport of an interacting elongated Bose-Einstein condensate in a random potential*, Phys. Rev. Lett. **95**(17), 170409 (2005).

[110] L. Sanchez-Palencia and M. Lewenstein, *Disordered quantum gases under control*, Nat. Phys. **6**, 87 (2010).

[111] `https://physics.stackexchange.com/questions/653883/what-is-the-meaning-or-definition-of-correlation-length-in-the-context-of-ande`, accessed: 2023-11-06.

[112] N. W. Ashcroft and D. N. Mermin, *Solid State Physics* (Thomson Learning, Toronto, 1976).

[113] E. Abrahams, P. W. Anderson, D. C. Licciardello, and T. V. Ramakrishnan, *Scaling theory of localization: Absence of quantum diffusion in two dimensions*, Phys. Rev. Lett. **42**, 673 (1979).

[114] D. J. Thouless, *Electron in disordered systems and the theory of localization*, Phys. Rep. **13**, 93 (1974).

[115] J. T. Edwards and D. J. Thouless, J. Phys. C: Solid State Phys. **5**, 807 (1972).

[116] A. Lagendijk, B. A. van Tiggelen, and D. Wiersma, *Fifty years of Anderson localization*, Phys. Today **62**, 24 (2009).

[117] S. John, *Electromagnetic absorption in a disordered medium near a photon mobility edge*, Phys. Rev. Lett. **53**(22), 2169 (1984).

[118] J. Billy, V. Josse, Z. Zuo, A. Bernard, B. Hambrecht, P. Lugan, D. Clément, L. Sanchez-Palencia, P. Bouyer, and A. Aspect, *Direct observation of Anderson localization of matter waves in a controlled disorder*, Nature (London) **453**, 891 (2008).

[119] L. Sanchez-Palencia, D. Clément, P. Lugan, P. Bouyer, G. V. Shlyapnikov, and A. Aspect, *Anderson localization of expanding Bose-Einstein condensates in random potentials*, Phys. Rev. Lett. **98**, 210401 (2007).

[120] D. A. Abanin, E. Altman, I. Bloch, and M. Serbyn, *Colloquium: Many-body localization, thermalization, and entanglement*, Rev. Mod. Phys. **91**, 021001 (2019).

[121] J. D. Reppy, *$^4$He as a dilute Bose gas*, Physica B+C **126**, 335 (1984).

[122] T. Giamarchi and H. J. Schulz, *Anderson localization and interactions in one-dimensional metals*, Phys. Rev. B **37**(1), 325 (1988).

[123] S. Poon, *Electronic properties of quasicrystals an experimental review*, Adv. Phys. **41**, 303 (1992).

[124] J. Biddle, B. Wang, D. J. Priour Jr, and S. Das Sarma, *Localization in one-dimensional incommensurate lattices beyond the Aubry-André model*, Phys. Rev. A **80**, 021603 (2009).

[125] J. Biddle, D. J. Priour Jr, B. Wang, and S. D. Sarma, *Localization in one-dimensional lattices with non-nearest-neighbor hopping : Generalized Anderson and Aubry-André models*, Phys. Rev. B **83**, 075105 (2011).

[126] A. Taoufyq, H. Ait Ahsaine, M. Arab, B. Abdeljalil, M. Ezahri, F. Guinneton, A. Lyoussi, G. Nolibe, and J.-R. Gavarri, *Electron microscopy analyses and electrical properties of the layered bi2wo6 phase*, Journal of Solid State Chemistry **203**, 8–18 (07 2013).

[127] L. Pauling, *Apparent icosahedral symmetry is due to directed multiple twinning of cubic crystals*, Nature **317**(6037), 512 (1985).

[128] L. Pauling, *Evidence from x-ray and neutron powder diffraction patterns that the so-called icosahedral and decagonal quasicrystals of mnal6 and other alloys are twinned cubic crystals*, Proceedings of the National Academy of Sciences **84**(12), 3951 (1987).

[129] L. Pauling, *So-called icosahedral and decagonal quasicrystals are twins of an 820-atom cubic crystal*, Physical review letters **58**(4), 365 (1987).

[130] L. Pauling, *Icosahedral quasicrystals as twins of cubic crystals containing large icosahedral clusters of atoms: The 1012-atom primitive cubic structure of al6culi3, the c-phase al37cu3li21mg3, and gamg2zn3*, Proceedings of the National Academy of Sciences **85**(11), 3666 (1988).

[131] L. Pauling, *Unified structure theory of icosahedral quasicrystals: Evidence from neutron powder diffraction patterns that alcrfemnsi, alculimg, and tinifesi icosahedral quasicrystals are twins of cubic crystals containing about 820 or 1012 atoms in a primitive unit cube*, Proceedings of the National Academy of Sciences **85**(22), 8376 (1988).

[132] L. Pauling, *Icosahedral quasicrystals of intermetallic compounds are icosahedral twins of cubic crystals of three kinds, consisting of large (about 5000 atoms) icosahedral complexes in either a cubic body-centered or a cubic face-centered arrangement or smaller (about 1350 atoms) icosahedral complexes in the $\beta$-tungsten arrangement*, Proceedings of the National Academy of Sciences **86**(22), 8595 (1989).

[133] L. Pauling, *Analysis of pulsed-neutron powder diffraction patterns of the icosahedral quasicrystals pd3siu and alculimg (three alloys) as twinned cubic crystals with large units.*, Proceedings of the National Academy of Sciences **88**(15), 6600 (1991).

[134] W. Steurer and S. Deloudi, *Fascinating quasicrystals*, Acta Crystallographica Section A: Foundations of Crystallography **64**(1), 1 (2008).

[135] D. Gratias and M. Quiquandon, *Discovery of quasicrystals: The early days*, Comptes Rendus Physique **20**(7-8), 803 (2019).

[136] A. Jagannathan, *The fibonacci quasicrystal: Case study of hidden dimensions and multifractality*, Reviews of Modern Physics **93**(4), 045001 (2021).

[137] Wikipedia contributors, *Penrose tiling — Wikipedia, the free encyclopedia* (2023), [Online; accessed 10-November-2023], `https://en.wikipedia.org/w/index.php?title=Penrose_tiling&oldid=1184260757`.

[138] Wikipedia contributors, *Aperiodic tiling — Wikipedia, the free encyclopedia* (2023), [Online; accessed 10-November-2023], `https://en.wikipedia.org/w/index.php?title=Aperiodic_tiling&oldid=1180331435`.

[139] A. L. Mackay, *Crystallography and the penrose pattern*, Physica A: Statistical Mechanics and its Applications **114**(1), 609 (1982).

[140] D. J. Boers, B. Goedeke, D. Hinrichs, and M. Holthaus, *Mobility edges in bichromatic optical lattices*, Phys. Rev. A **75**, 063404 (2007).

[141] X. Li, X. Li, and S. Das Sarma, *Mobility edges in one-dimensional bichromatic incommensurate potentials*, Phys. Rev. B **96**, 085119 (2017).

[142] H. P. Lüschen, S. Scherg, T. Kohlert, M. Schreiber, P. Bordia, X. Li, S. Das Sarma, and I. Bloch, *Single-particle mobility edge in a one-dimensional quasiperiodic optical lattice*, Phys. Rev. Lett. **120**, 160404 (2018).

[143] D. M. Ceperley, *Path integrals in the theory of condensed helium*, Rev. Mod. Phys. **67**, 279 (1995).

[144] M. Boninsegni, N. Prokof'ev, and B. Svistunov, *Worm algorithm for continuous-space path integral Monte Carlo simulations*, Phys. Rev. Lett. **96**, 070601 (2006).

[145] M. Boninsegni, N. V. Prokof'ev, and B. V. Svistunov, *Worm algorithm and diagrammatic Monte Carlo: A new approach to continuous-space path integral Monte Carlo simulations*, Phys. Rev. E **74**, 036701 (2006).

[146] R. Peierls, in *Annales de l'institut Henri Poincaré* (1935), vol. 5, pp. 177–222.

[147] N. D. Mermin and H. Wagner, *Absence of ferromagnetism or antiferromagnetism in one-or two-dimensional isotropic heisenberg models*, Physical Review Letters **17**(22), 1133 (1966).

[148] P. C. Hohenberg, *Existence of long-range order in one and two dimensions*, Physical Review **158**(2), 383 (1967).

[149] V. L. Berezinskii, *Destruction of long range order in one-dimensional and two-dimensional systems having a continuous symmetry group. 1. classical systems*, Sov. Phys. JETP **32**, 493 (1971).

[150] J. M. Kosterlitz and D. J. Thouless, *Ordering, metastability and phase transitions in two-dimensional systems*, J. Phys. C: Solid State Phys. **6**, 1181 (1973).

[151] J. M. Kosterlitz, *The critical properties of the two-dimensional XY model*, J. Phys. C: Solid State Phys. **7**(6), 1046 (1974).

[152] N. Prokof'ev, O. Ruebenacker, and B. Svistunov, *Critical point of a weakly interacting two-dimensional Bose gas*, Phys. Rev. Lett. **87**, 270402 (2001).

[153] N. Prokof'ev and B. Svistunov, *Two-dimensional weakly interacting Bose gas in the fluctuation region*, Phys. Rev. A **66**, 043608 (2002).

[154] G. Carleo, G. Boéris, M. Holzmann, and L. Sanchez-Palencia, *Universal superfluid transition and transport properties of two-dimensional dirty bosons*, Phys. Rev. Lett. **111**, 050406 (2013).

[155] H. Yao, *Strongly-correlated one-dimensional bosons in continuous and quasiperiodic potentials*, Theses, Institut Polytechnique de Paris (Oct. 2020), `https://theses.hal.science/tel-03065015`.

[156] R. P. Feynman, A. R. Hibbs, and D. F. Styer, *Quantum mechanics and path integrals* (Courier Corporation, 2010).

[157] Z. Zhu, H. Yao, and L. Sanchez-Palencia, *Thermodynamic phase diagram of two-dimensional bosons in a quasicrystal potential*, Phys. Rev. Lett. **130**, 220402 (2023).

[158] J.-C. Yu, S. Bhave, L. Reeve, B. Song, and U. Schneider, *Observing the two-dimensional Bose glass in an optical quasicrystal*, arXiv:2303.00737.

[159] E. Gottlob and U. Schneider, *Hubbard models for quasicrystalline potentials*, Phys. Rev. B **107**, 144202 (2023).

[160] A. Saul, A. M. Llois, and M. Weissmann, *Wavefunctions of one-dimensional incommensurate hamiltonians: The fractal dimension and its relationship with localisation*, J. Phys. C: Solid State Phys. **21**, 2137 (1988).

[161] H. Hiramoto and M. Kohmoto, *Scaling analysis of quasiperiodic systems: Generalized Harper model*, Phys. Rev. B **40**, 8225 (1989).

[162] A. Szabó and U. Schneider, *Mixed spectra and partially extended states in a two-dimensional quasiperiodic model*, Phys. Rev. B **101**, 014205 (2020).

[163] M. N. Kosch, L. Asteria, H. P. Zahn, K. Sengstock, and C. Weitenberg, *Multifrequency optical lattice for dynamic lattice-geometry control*, Phys. Rev. Research **4**, 043083 (2022).

[164] S. E. Pollack, D. Dries, M. Junker, Y. P. Chen, T. A. Corcovilos, and R. G. Hulet, *Extreme tunability of interactions in a $^7$Li Bose-Einstein condensate*, Phys. Rev. Lett. **102**, 090402 (2009).

[165] S. S. Kondov, W. R. McGehee, J. J. Zirbel, and B. DeMarco, *Three-dimensional Anderson localization of ultracold fermionic matter*, Science **334**, 66 (2011).

[166] F. Jendrzejewski, A. Bernard, K. Müller, P. Cheinet, V. Josse, M. Piraud, L. Pezzé, L. Sanchez-Palencia, A. Aspect, and P. Bouyer, *Three-dimensional localization of ultracold atoms in an optical disordered potential*, Nat. Phys. **8**, 398 (2012).

[167] R. C. Kuhn, O. Sigwarth, C. Miniatura, D. Delande, and C. A. Müller, *Coherent matter wave transport in speckle potentials*, New J. Phys. **9**(6), 161 (2007).

[168] S. E. Skipetrov, A. Minguzzi, B. A. van Tiggelen, and B. Shapiro, *Anderson localization of a Bose-Einstein condensate in a 3D random potential*, Phys. Rev. Lett. **100**, 165301 (2008).

[169] M. Piraud, P. Lugan, P. Bouyer, A. Aspect, and L. Sanchez-Palencia, *Localization of a matter wave packet in a disordered potential*, Phys. Rev. A **83**, 031603(R) (2011).

[170] M. Piraud, L. Pezzé, and L. Sanchez-Palencia, *Matter wave transport and Anderson localization in anisotropic three-dimensional disorder*, Europhys. Lett. **99**, 50003 (2012).

[171] M. Piraud, L. Pezzé, and L. Sanchez-Palencia, *Quantum transport of atomic matter waves in anisotropic two-dimensional and three-dimensional disorder*, New J. Phys. **15**, 075007 (2013).

[172] L. Pezzé and L. Sanchez-Palencia, *Localized and extended states in a disordered trap*, Phys. Rev. Lett. **106**, 040601 (2011).

[173] M. Ciardi, T. Macrì, and F. Cinti, *Finite-temperature phases of trapped bosons in a two-dimensional quasiperiodic potential*, Phys. Rev. A **105**, L011301 (2022).

[174] D. S. Petrov, M. Holzmann, and G. V. Shlyapnikov, *Bose-Einstein condensation in quasi-2D trapped gases*, Phys. Rev. Lett. **84**, 2551 (2000).

[175] D. Petrov and G. Shlyapnikov, *Interatomic collisions in a tightly confined Bose gas*, Phys. Rev. A **64**, 012706 (2001).

[176] L. Pricoupenko and M. Olshanii, *Stability of two-dimensional Bose gases in the resonant regime*, J. Phys. B: At. Mol. Opt. Phys. **40**, 2065 (2007).

[177] L.-C. Ha, C.-L. Hung, X. Zhang, U. Eismann, S.-K. Tung, and C. Chin, *Strongly interacting two-dimensional Bose gases*, Phys. Rev. Lett. **110**, 145302 (2013).

[178] D. R. Nelson and J. M. Kosterlitz, *Universal jump in the superfluid density of two-dimensional superfluids*, Phys. Rev. Lett. **39**, 1201 (1977).

[179] To ease comparison to the quasicrystal case, the chemical potential is noted with a prime for the homogeneous case.

[180] A. L. Gaunt, T. F. Schmidutz, I. Gotlibovych, R. P. Smith, and Z. Hadzibabic, *Bose-Einstein condensation of atoms in a uniform potential*, Phys. Rev. Lett. **110**, 200406 (2013).

[181] L. Chomaz, L. Corman, T. Bienaimé, R. Desbuquois, C. Weitenberg, S. Nascimbène, J. Beugnon, and J. Dalibard, *Emergence of coherence via transverse condensation in a uniform quasi-two-dimensional Bose gas*, Nat. Comm. **6**, 6162 (2015).

[182] N. Navon, R. P. Smith, and Z. Hadzibabic, *Quantum gases in optical boxes*, Nat. Phys. **17**, 1334 (2021).

[183] M. Kohmoto and B. Sutherland, *Electronic states on a penrose lattice*, Physical review letters **56**(25), 2740 (1986).

[184] B. Sutherland, *Self-similar ground-state wave function for electrons on a two-dimensional penrose lattice*, Physical Review B **34**(6), 3904 (1986).

[185] Z. Akdeniz and P. Vignolo, *Condensate oscillations in a penrose tiling lattice*, Physica E: Low-dimensional Systems and Nanostructures **91**, 136 (2017).

[186] J.-M. Gambaudo and P. Vignolo, *Brillouin zone labelling for quasicrystals*, New Journal of Physics **16**(4), 043013 (2014).

[187] P. Vignolo, M. Bellec, J. Böhm, A. Camara, J.-M. Gambaudo, U. Kuhl, and F. Mortessagne, *Energy landscape in a penrose tiling*, Physical Review B **93**(7), 075141 (2016).

ECOLE DOCTORALE

**Titre :** Atomes froids dans des quasi-cristaux bidimensionnels

**Mots clés :** Quasi-cristaux, Bosons fortement corrélés, Monte Carlo quantique

**Résumé :** Les quasi-cristaux sont des solides ordonnés à longue distance sans symétrie de translation, présentant des symétries rotationnelles qui sont interdites pour les cristaux normaux, par exemple d'ordre 5, 7, 8, ... Leur découverte en laboratoire dans les années 1980 a entraîné un changement de paradigme en cristallographie, révolutionnant notre compréhension de la structure possible des solides. Depuis lors, les quasi-cristaux ont attiré beaucoup d'attention en raison de leurs propriétés intrigantes, notamment les quasi-particules phasoniques, les propriétés de transport, le spectre d'énergie complexe, l'ordre topologique non trivial et la localisation de type Anderson. Un outil puissant pour étudier les propriétés physiques des quasi-cristaux est la simulation quantique. Avec la réalisation de systèmes atomiques ultrafroids dans les années 1990 et les développements rapides qui ont suivi, un nouveau terrain de jeu pour la physique quantique à plusieurs corps s'est ouvert. En particulier, le contrôle précis des paramètres physiques et les différents outils de mesure dans un système atomique froid en font une plateforme prometteuse pour la simulation quantique. Un potentiel quasipériodique unidimensionnel dans les expériences sur les atomes froids peut être créé en superposant plusieurs faisceaux laser avec des périodes incommensurables. Au cours des dernières années, les atomes froids dans des potentiels quasipériodiques unidimensionnels ont été largement étudiés. Un réseau optique bidimensionnel formant un potentiel quasi-cristallin peut également être créé par certaines configurations géométriques de faisceaux laser. Cela a été proposé pour la première fois théoriquement en 2005 et réalisé dans des expériences sur les atomes froids en 2019, suivant une configuration proposée en 2013. La localisation de bosons faiblement interactifs dans ce système a été rapportée. Avec ces avancées dans les expériences, les études théoriques sur les atomes froids bidimensionnels dans des potentiels quasicristaux commencent également à gagner du terrain. Dans cette thèse, nous présentons une étude théorique de la simulation quantique de quasicristaux bidimensionnels avec des atomes froids. Nous discutons des propriétés des particules individuelles et des diagrammes de phase thermodynamiques pour des bosons bidimensionnels dans un potentiel quasicristallin peu profond.

**Title :** Cold atoms in two dimensional quasicrystals

**Keywords :** Quasicrystals, Strongly correlated bosons, Quantum Monte Carlo

**Abstract :** Quasicrystals are long-range-ordered solids without translational symmetry, showing rotational symmetries that are forbidden for normal crystals, for example 5 fold, 7 fold, 8 fold etc. Their discovery in the laboratory during the 1980s lead to a paradigm shift in crystallography, revolutionizing the basic idea on possible structure of solids. Since then on, quasicrystals have attracted much attentions, owing to their intriguing properties, including for examples phasonic quasiparticles, transport properties, intricate energy spectrum, nontrivial topological order and Anderson-like localization. A powerful tool to study the physical properties of quasicrystals is quantum simulation. With the realization of ultracold atomic systems in the 1990s and the rapid developments thereon, a new playground of quantum many body physics has opened. In particular, the strong control over the physical parameters and the various measurement tools in a cold atomic system make it a promising platform for quantum simulation. A one-dimensional quasiperiodic potential in cold atoms experiments can be created by superimposing several laser beams with incommensurable periods. In the past years, cold atoms in one-dimensional quasiperiodic potentials have been studied extensively. A two-dimensional optical lattice giving a quasicrystal potential can also be created by certain geometrical arrangements of laser beams. This was first proposed theoretically in 2005, and realized in cold atoms experiments in 2019 following a configuration proposed in 2013. Localization of weakly interacting bosons in that system has been reported. With these advancements in experiments, the theoretical studies of two dimensional cold atoms in quasicrystal potentials also start to gain momentum. In this thesis, we give a theoretical study of quantum simulation of two-dimensional quasicrystals with cold atoms. We discuss the single particle properties and the thermodynamic phase diagrams for two dimensional bosons in a shallow quasicrystal potential.

**Institut Polytechnique de Paris**
91120 Palaiseau, France